

FRACTURE TOUGHNESS ENHANCEMENT AND  
SYNTHESIS OF  $ZrO_2$  BEARING CERAMIC ALLOYS

by

THOMAS DALE KETCHAM

B.S., University of Utah  
(1975)

SUBMITTED IN PARTIAL FULFILLMENT  
OF THE REQUIREMENTS FOR THE  
DEGREE OF

DOCTOR OF SCIENCE

at the

MASSACHUSETTS INSTITUTE OF TECHNOLOGY

February 1982

© Massachusetts Institute of Technology 1982

Signature of Author **Signature redacted**  
Department of Materials Science and Engineering  
January 8, 1982

Certified by **Signature redacted**  
Rowland M. Cannon, Jr.  
Thesis Supervisor

Accepted by **Signature redacted**  
Regis M. Pelloux  
Chairman, Department Committee

Archives  
MASSACHUSETTS INSTITUTE  
OF TECHNOLOGY

MAY 3 1982

LIBRARIES

## ABSTRACT

### FRACTURE TOUGHNESS ENHANCEMENT AND SYNTHESIS OF $ZrO_2$ BEARING CERAMIC ALLOYS

BY

THOMAS DALE KETCHAM

Submitted to the Department of Materials Science and Engineering on January 8, 1982 in partial fulfillment of the requirements for the degree of Doctor of Science

An exploratory experimental study of the synthesis and fracture toughness of  $ThO_2$ - $ZrO_2$  ceramic alloys and a theoretical three-dimensional analysis of the variation of stress intensity along a crack front near a misfitting inclusion are presented.

The synthesis of 100% dense, polycrystalline two phase  $ThO_2$ - $ZrO_2$  alloys with grain sizes between 0.1-2 microns is described. Oxide powders were obtained primarily from hydroxides and densified by hot pressing and sintering at 1400°C to 1600°C. Dense materials with grain sizes <0.5 micron were obtained after hot pressing and coarser grain sizes were obtained by heat treating. Porous (92-97% dense) specimens of  $ThO_2$ - $ZrO_2$  with larger  $ZrO_2$  grain sizes (1-10 microns) were produced by sintering oxide powders derived from thorium oxalate and  $ZrO_2$ . With 0.1-0.3 micron  $ZrO_2$  grains in dense material,  $ZrO_2$  can be maintained in the high temperature (> 1070°C) tetragonal crystal structure to room temperature. At larger  $ZrO_2$  grain sizes and higher porosities transformation to the lower density monoclinic phase occurs. Toughened alloys of  $AlCrO_3$  - 40 v/o  $ZrO_2$  ( $K_{IC}=6.6 \text{ MPa m}^{1/2}$ ),  $3Al_2O_3 \cdot 2SiO_2$ -20 v/o  $ZrO_2$  ( $K_{IC}=4.5 \text{ MPa m}^{1/2}$ ) and  $ThO_2$ -20 m/o ( $Zr_{.6}Hf_{.4}$ ) $O_2$  were also produced. Fracture toughness enhancement from  $\sim 1.6 \text{ MPa m}^{1/2}$  for  $ThO_2$  to  $>3 \text{ MPa m}^{1/2}$  can occur in  $ThO_2$ - $ZrO_2$  alloys with  $ZrO_2$  contents from 15 to 46 m/o  $ZrO_2$  as measured by the microhardness indentation technique. For  $ThO_2$ -15 m/o  $ZrO_2$  alloys a high fracture toughness of  $>3 \text{ MPa m}^{1/2}$  and good transmission of infrared light at 5-6 micron wavelengths can be obtained simultaneously.



For the dense, submicron grain sized material the toughness enhancement is attributed to the retention of the tetragonal  $ZrO_2$  phase and the martensitic nature of the tetragonal to monoclinic phase transformation which can be stress induced near propagating cracks. For the porous, coarser grained materials, microcracking near the main crack probably contributes to the toughness. At high density and large  $ZrO_2$  grain sizes (from 0.3 to 1 micron depending on  $ZrO_2$  content), low toughness and spontaneous fracture occur. The detailed microstructure of the alloy, the  $ZrO_2$  content, the  $ZrO_2$  grain size, the  $ZrO_2$  grain size distribution and porosity all effect the tetragonal to monoclinic ratio, the fracture toughness and spontaneous fracture behavior of  $ThO_2-ZrO_2$ . Surface compressive stresses caused by grinding induced transformation can occur in these alloys and increase the measured toughness. The tetragonal to monoclinic transformation and the resulting toughening appear to be nucleation controlled in  $ThO_2-ZrO_2$  alloys.

The interaction of a misfitting inclusion and a straight front crack is treated using three-dimensional elasticity and modelling the inclusion as a point source of expansion. The basic formulation results in an expression for the local stress intensity,  $\Delta K$ , involving a double integral. This was solved using three methods. A rigorous method using Legendre polynomials was developed. Two non-rigorous methods, one using Fourier series and a second using an approximate solution for a contour integral were obtained. Numerical solutions by the latter two methods were obtained for several inclusion positions near a crack tip. The numerical solutions predict an inclusion with a volume expansion that is within a region  $\pm 45^\circ$  ahead of the crack tip will promote local crack extension, while an expanding inclusion which is further out of plane or behind the crack tip will impede local crack extension. The accuracies and limitations of the methods and applications of this calculation to modelling microcrack or transformation toughening are discussed. The double integral describing

the interaction of the crack and inclusion is very similar to integrals describing the interaction of a straight crack front with general point forces in three dimensions, thus the methods of solution might be useful for a range of fracture mechanics problems.

Thesis Supervisor: Rowland M. Cannon, Jr.  
Title: Associate Professor of Ceramics

## Table of Contents

	<u>page</u>
Title Page	1
Abstract	2
Table of Contents	5
List of Figures	7
List of Tables	11
Acknowledgements	12
I. Introduction	14
II.A. General Literature Review	16
II.B. Intended Research	37
III. Sample Production	39
III.A. Processing Literature Review	39
III.B. Experimental Method	44
III.C. Results - Processing	57
III.D. Discussion	92
III.E. Conclusions	95
IV. Fracture Toughness and Phase Transformation	97
IV.A. Introduction	97
IV.B. Experimental Method	101
IV.C. Results	102
IV.D. Discussion	136
IV.E. Speculation Regarding Nucleation	142
IV.F. Conclusions	146
V. Stress Intensity Variation Calculation	148



	<u>page</u>
V.A. Motivation for Model Development	148
V.B. Formulation of $\Delta K_I$ Problem	150
V.C. Calculation of $\Delta K_I$	157
V.D. Discussion	175
V.E. Conclusions	181
VI. Summary	184
VI.A. Total Conclusions	184
VI.B. Discussion	185
VI.C. Suggestions For Further Research	186
Appendix A. I.R. Transmission of $ZrO_2$ Bearing Alloys	188
Appendix B. Other $ZrO_2$ Toughened Alloys	195
Appendix C. Mathematical Details for Section V	197
Bibliography	204
Biographical Note	212

## List of Figures

	<u>page</u>
II 1	The $ZrO_2$ -MgO system 19
II 2	$\Delta G$ vs. Temperature and $K_{IC}$ vs. Temperature Schematic 27
II 3	$K_{IC}$ and $\sigma$ vs. Annealing Time for PSZ 35
III 1	The $ZrO_2$ - $ThO_2$ system 40
III 2	Flow chart for sample preparation 46
III 3	As hot pressed grain size of $ThO_2$ -15 m/o $ZrO_2$ , H-85-II 60
III 4	As hot pressed grain size and grain size distribution of $ThO_2$ -15 m/o $ZrO_2$ , H-85-Th1 61
III 5	Particle size of powder from hydroxides 67
III 6	Agglomerate size of powder from hydroxides 67
III 7	Example of a large $ZrO_2$ grain size and wide grain size distribution, H-85-G 69
III 8	Example of non-uniform $ZrO_2$ distribution, H-85-F 69
III 9	Non-uniform $ZrO_2$ grain size distribution, H-85-Th 40 71
III 10	Surface of slip cast, translucent green body 73
III 11	$ZrO_2$ grain size and grain size distribution in annealed $ThO_2$ -15 m/o $ZrO_2$ , H-85-H9 76
III 12	As hot pressed grain size of $ThO_2$ -15 m/o $ZrO_2$ , H-85-H1 78
III 13	Porosity in sintered $ThO_2$ -15 m/o $ZrO_2$ , 1/2 hr. 1600°C 82
III 14	Porosity in sintered $ThO_2$ -15 m/o $ZrO_2$ , 2.5 hr. 1600°C 83
III 15	$ZrO_2$ grain size in pseudoisostatically hot pressed $ThO_2$ -15 m/o $ZrO_2$ , HSF-85-A9 84
III 16	Fracture surface of bloated $ThO_2$ -20 m/o $ZrO_2$ , H-80-B10 84

	<u>page</u>	
III 17	Fine pores ( $\sim 500 \text{ \AA}$ ) caused by oxidation, H-85-D2	88
IV 1	Empirical curve of Evans and Charles used for $K_{IC}$ measurement	103
IV 2	Dislocations, microcracks and twinned $ZrO_2$ in $ThO_2$ -15 m/o $ZrO_2$ , H-85-D2	106
IV 3	Microcracks in $ThO_2$ -15 m/o $ZrO_2$ sintered from oxalate precursors	108
IV 4	Schematic of crack sizes for various $K_{IC}$ 's	111
IV 5	$K_{IC}$ vs. $ZrO_2$ content, hot pressed samples with $ZrO_2$ grain size of 0.1-0.3 micron	113
IV 6	$K_{IC}$ vs. $ZrO_2$ content hot pressed and annealed samples	116
IV 7	$K_{IC}$ vs. $ZrO_2$ content, sintered samples, powder from oxalate precursors	119
IV 8	Indent impression in $ThO_2$ -20 m/o $ZrO_2$ , sintered sample, powder from oxalate precursors	120
IV 9	$K_{IC}$ vs. annealing time for hot pressed $ThO_2$ -15 m/o $ZrO_2$ samples	121
IV 10	$ZrO_2$ grain size and medium to narrow grain size distribution in an annealed $ThO_2$ -15 m/o $ZrO_2$ , H-85-Th 6	127
IV 11	Indent impression in $ThO_2$ -15 m/o $ZrO_2$ , narrow grain size distribution	130
IV 12	Indent impression in $ThO_2$ -15 m/o $ZrO_2$ , medium grain size distribution	130
IV 13	Indent impression in $ThO_2$ -15 m/o $ZrO_2$ , wide grain size distribution	131



	<u>page</u>
IV 14	$K_{IC}$ vs. $ZrO_2$ grain size, $ThO_2$ -15 m/o $ZrO_2$ 132
IV 15	Indent impression in annealed $ThO_2$ -15 m/o $ZrO_2$ , $K_{IC} = 3.3 \text{ MPam}^{1/2}$ , H-85-B9 134
IV 16	Large M- $ZrO_2$ grain without microcracking 137
V 1a	Coordinate orientation and sphere position for stress intensity calculation 151
b	Stress superposition schematic
V 2	Normalized stress intensity vs. normalized distance 161 for $x_{o/a} = -2$ , $y_{o/a} = 2$ , Fourier series method
V 3	Normalized stress intensity vs. normalized distance 162 for $x_{o/a} = 0$ , $y_{o/a} = 2$ , Fourier series method
V 4	Normalized stress intensity vs. normalized distance 163 for $x_{o/a} = 2$ , $y_{o/a} = 2$ , Fourier series method
V 5	Normalized stress intensity vs. normalized distance 164 for $x_{o/a} = 2$ , $y_{o/a} = 0$ , Fourier series method
V 6	Comparison of normalized stress intensity vs. 170 normalized distance for $x_{o/a} = 2$ , $y_{o/a} = 2$ calculated by Fourier series and rapid non-rigorous (RNR) methods
V 7	Comparison of normalized stress intensity vs. 171 normalized distance for $x_{o/a} = 0$ , $y_{o/a} = 2$ calculated by Fourier series and RNR methods
V 8	Comparison of normalized stress intensity vs. normalized 172 distance for $x_{o/a} = 2$ , $y_{o/a} = 2$ calculated by Fourier series and RNR methods
V 9	Comparison of normalized stress intensity vs. normalized 173

page

distance for  $x_{o/a}=2, y_{o/a}=0$  calculated by Fourier series, RNR and limited rapid non-rigorous (LRNR) methods

A.A.1	Index mismatch vs. particle size for I.R. windows	190
A.A.2	IR transmission of hot pressed $\text{ThO}_2\text{-ZrO}_2$ alloys	192
A.C.1	Contour for complex residue integral A.C. 10	199
A.C.2	Vector representation for equations A.C. 12a & b	199

## List of Tables

	<u>page</u>
I Sample Nomenclature, $\text{ThO}_2\text{-ZrO}_2$ Produced from Hydroxide Precipitation	62
II $\text{ThO}_2\text{-ZrO}_2$ Samples from Hydroxides Standard Processing	65
III $\text{ThO}_2\text{-ZrO}_2$ Samples, Sintered	80
IV Effect of Air Annealing Hot Pressed $\text{ThO}_2\text{-ZrO}_2$	87
V $\text{ThO}_2\text{-ZrO}_2$ Samples Produced from Oxalate Precipitation	91
VI Crack Sizes for $H = 9.5$ GPa	110
VII Effects of Surface Condition	114
VIII Toughness of Annealed $\text{ThO}_2\text{-46 m/o ZrO}_2$	117
IX Toughness of Miscellaneous Samples	123
X Toughness of Heat Treated Samples of H-85-Th	125
XI Semiquantitative Impurity Analysis	128
XII Fourier Series Method	160
Al Optical and Mechanical Properties of Toughened I.R. Windows	193



## Acknowledgements

The author wishes to express his appreciation to many people without whom this thesis would not exist. First and foremost among them is Professor Rowland Cannon. He provided much wisdom, inspiration and the framework on which this thesis rests. His patience and forbearance during my occasional outbursts of irrationality was commendable. His critical reading of the first draft has made this thesis an improved document. Professor Robert Coble provided guidance and help at crucial junctures. Professor H. Kent Bowen provided funds during the author's first two and one half years at M.I.T. and helpful advice. Tom Coyle injected fresh ideas and energy into the I.R. window project. He is thanked for allowing me access to his reference files. The excellent TEM micrographs produced by Joachim Schneibel grace the forthcoming pages. Some conclusions are based on these micrographs and would only be speculations without them.

Pat Kearney deserves special mention for providing me with several furnaces, many alumina tubes and crucibles and much technical assistance. Al Freker was helpful on technical matters. John Centorino, Pat Kearney and I spent an interesting, high pressure week hot pressing hercynite-magnetite spinels. Linda Sayegh performed miracles in typing my thesis, Joe's thesis and Anna's thesis all at the same time under great pressure. Linda is thanked especially for the expert typing of the difficult equations. Patricia Risley at Corning Glass Works is thanked for typing many pages of corrections and additions. My wife Jane Ketcham and son Edwin (age 9-13 months) typed the first draft magnificently.

Joe Dynys contributed several evenings of SEM time and drew figure A.A.1.. Tom Coyle did several BET measurements and draw figure A.A.2.. Dave Cranmer provided an evening of SEM time. Harry Fujimoto first suggested a version of water and organic fluid washing of hydroxides. Bill Coblenz provided several useful suggestions (wheat<<chaff).

As the author spent a considerable amount of time as a graduate student at MIT a great number of people associated with MIT contributed to his emotional well being. They cannot all be listed individually, if you are not listed it is due to the author's poor memory. John Blendell and Carol Handwerker are exceptional people and I was privileged to be their friend. Jim Hodge was a good apartment mate, friend and wedding attendant. Joe Dynys was a constant inspiration and Dave Cranmer cleared the air on many issues. Tom Coyle and Bill Hong made lunchtime more interesting. Pairs of people who provided amusement (in different ways) were Paul Lemaire and Tom Yager, Bill Tasker and Mike Barsoum, John Hart, Nancy Dudley and Isabel Lloyd, L. Schioler and F. VanGieson, Keith and Mary, and A. N. Onymous and A. F. ReLaplacemont. Thank God for the Muddy, the Wellesley Madrigal and softball. Ace Blum (residence doggy heaven) provided several exciting moments.

My family, and later Jane's family, provided financial assistance and crucial emotional support. Their help and advice was vital to this endeavor.

Financial support for graduate research not covered in this thesis was provided by the U.S. Department of Energy, contract # DE-AC01-79ET 15518. Financial support for research covered in the thesis from; (1) the U.S. Department of Defense through D.A.P.R.A. and the General Electric Company, monitored by O.N.R., contract # N00014-78-C0466, and through O.N.R. contract # N00014-81-K-0450; (2) Detroit Diesel Allison, and (3) MIT (half semester T.A.) is gratefully acknowledged. I would like to personally thank the American taxpayers for the funds they provided, directly from the U.S. Dept. of Defense and U.S. Dept. of Energy, and indirectly and partially funds from MIT, that supported my work. My wife Jane, and later my son Edwin, were the only reason(s) that I was able to finish this work. Without Jane's love, patience and listening ability my graduation would not have occurred. Because of her sacrifices, particularly over the last year during which I developed the model in section V, I can only say that this thesis is as much hers as mine.

Yes Mom and Dad, I've finished.



## I. INTRODUCTION

A revolution has been occurring in the structural ceramics field during the latter half of the decade of the 1970's. Prior to this time improvements in the mechanical properties of ceramics occurred due to the reduction in flaw sizes obtained by improved processing methods. The intrinsic properties of structural ceramics (fracture toughness) were not successfully altered to any great degree. Improvements in  $K_{IC}$  (or work of fracture) of 25% were deemed successes. Several methods now exist that can improve  $K_{IC}$  by 100% to 1000%. One method is the addition of a minor amount of  $ZrO_2$  to an oxide to produce a  $ZrO_2$  bearing ceramic alloy;  $K_{IC}$  can be improved 100% to 200% and with the addition of compressively stressed surface layers, the 4-point bend strength of these ceramic alloys can be extremely high, about 1,200 MPa (175 Kpsi) (Claussen and Rühle 1981). The  $ZrO_2$  must be included as grains less than one micron, which demands fairly sophisticated powder processing and densification techniques.

This work covers the use of this  $ZrO_2$  alloying technique for  $ThO_2$ - $ZrO_2$  alloys. A review (Evans and Heuer 1980) of this toughening technique has been published and a recent book (Heuer and Hobbs, ed. 1981) contains the current published state of the art. Fairly involved powder processing and densification schemes are described; introductions to the engineering (Wang ed.) and scientific aspects (Kingery et al.) are recommended to those unfamiliar with nuances of ceramic fabrication. The mechanical results of the sample fabrication are analyzed via fracture mechanics theory; Lawn and Wilshaw is an introductory text and Evans and Langdon is more advanced though neither is recent enough to contain  $ZrO_2$  bearing alloys.



The importance of this toughening field to the use of structural ceramics has been only slightly exaggerated by calling these alloys ceramic steels. This toughening method may actually become more important to ceramics than steels are to metallurgy because the important properties of these ceramic alloys are derived from a minor (5-20 v/o) phase of  $ZrO_2$ . Under some circumstances  $ZrO_2$  may improve the mechanical properties enough to allow a slight degradation of other properties of the matrix ceramic. Lastly, the minor transforming phase may not need to be  $ZrO_2$ , any material with phase transformations with significant volume expansion or shear strain, or large numbers of microcracking events that occur in the stress field of a propagating crack may exhibit toughening behavior.

## II.A. GENERAL LITERATURE REVIEW

### II.A.1. Introduction

Improvement of the mechanical properties of zirconia alloys and other ceramics by the retention of a minor phase of tetragonal zirconia is a new field for ceramic science. Garvie et al. (1975) first clearly suggested the martensitic nature of the tetragonal to monoclinic phase transformation of zirconia occurring near a propagating crack, as one mechanism by which significant strength and fracture toughness enhancement of zirconia bearing ceramic alloys is possible. Many different microstructures and alloy compositions can now be produced to utilize this T→M transformation and the common denominator linking these microstructures is the presence of fine, 0.1-1 micron, grains or precipitates of tetragonal zirconia. These T-zirconia transform to monoclinic symmetry either in the high stress field of a propagating crack (transformation toughening, Garvie et al. 1975, Porter and Heuer 1977, Claussen 1978), or during cooling from the high temperature used for fabrication of the microstructure. If the T→M transformation occurs before crack propagation, microcracks need to form to significantly enhance the mechanical properties (microcrack toughening, Green et al. 1973, Claussen 1976, Claussen et al. 1977). Two interesting scientific questions that need to be addressed are: (1) the exact thermodynamic and kinetic conditions, including stress, that allow the retention of the tetragonal phase at low temperatures; (2) the coupling of this transformation to enhanced mechanical properties via transformational toughening or microcrack production.

## II.A.2. $ZrO_2$ Pre-1975

Pure  $ZrO_2$  has three polymorphs: the monoclinic form is stable during heating to about  $1170^\circ C$ , the tetragonal form is stable from  $1170^\circ C$  to about  $2370^\circ C$ , and the cubic form is stable to the melting point ( $2700^\circ C$ ). The high temperature cubic crystal structure is a fluorite type (Smith and Cline); the tetragonal and monoclinic forms/polymorphs can be regarded as distortions from the fluorite structure (Fig. 1 in Kriven et al. 1981). Wolten (1963) was the first to suggest that the tetragonal to monoclinic transformation was martensitic. The transformation is athermal, the monoclinic and tetragonal polymorphs coexist in pure bulk  $ZrO_2$  over extensive temperature ranges and the amount of a phase varies with temperature but not time. The transformation exhibits considerable hysteresis, with the M $\rightarrow$ T transformation occurring at about  $1000^\circ C$  to  $1200^\circ C$  upon heating and the T $\rightarrow$ M occurring at about  $900^\circ C$  to  $700^\circ C$  during cooling. The transformation within a grain proceeds at speeds approaching the sonic velocity (Fehrenbacher and Jacobson). Experimental and theoretical crystallographic information on the transformation is available (Bansal and Heuer, 1972, 1974, Kriven et al. 1981).

The volume change for the T $\rightarrow$ M transformation is about + 3 v/o at about  $950^\circ C$  (Kriven et al., 1981) with extensive shear strains in the unit cell, some of which can be accommodated by twinning on various planes and various structure scales (Kriven 1981). The large dilatational and shear strains are usually not accommodated plastically due to the high yield stress in the T- $ZrO_2$  surrounding the M- $ZrO_2$  plate. The transformation upon cooling usually leads to cracking and disruption of the



macroscopic integrity of a dense pure  $ZrO_2$  body of the T phase. It is this macroscopic failure of pure zirconia bodies that prevents the successful use of pure zirconia in anything other than powder form.

A cubic solid solution of the fluorite type with zirconia as the major chemical constituent can be formed with a number of oxides: MgO, CaO,  $Y_2O_3$ , and many rare earth oxides. There is considerable controversy about the accuracy of most published binary phase diagrams (Stubican and Hellmann). This is understandable because of the slow diffusion controlled solid state transformations at low temperatures, the martensitic nature of the T→M transformation and the chemical inhomogeneity of the starting materials (milled, large particle size oxides) used for some studies; however Figure II.1 of the  $ZrO_2$ -MgO system (Grain) can serve as a basis for discussion.

When about 12 m/o MgO is combined with  $ZrO_2$  at temperatures above  $1400^\circ C$  a face centered cubic solid solution ( $C_{ss}$ ) is formed. If the material is now cooled to room temperature, the material remains face-centered (cubic solid solution) because the decomposition reaction is slow. In the ceramics literature this is called fully stabilized zirconia. This alloy has no martensitic phase change, and the thermal expansion coefficient is isotropic. The cubic solid solution is of limited use as an engineering ceramic due to failure by thermal shock. The  $C_{ss}$  has a high thermal expansion coefficient  $9.7 \times 10^{-6}/^\circ C$  ( $0-1200^\circ C$  Neilsen and Leipold) and low thermal conductivity.

Manufacturers of commercial, binary alloys of zirconia solved this problem by producing a material of about 8.0 m/o MgO (or appropriate m/o of another oxide) in the two phase tetragonal solid solution ( $T_{ss}$ ) +



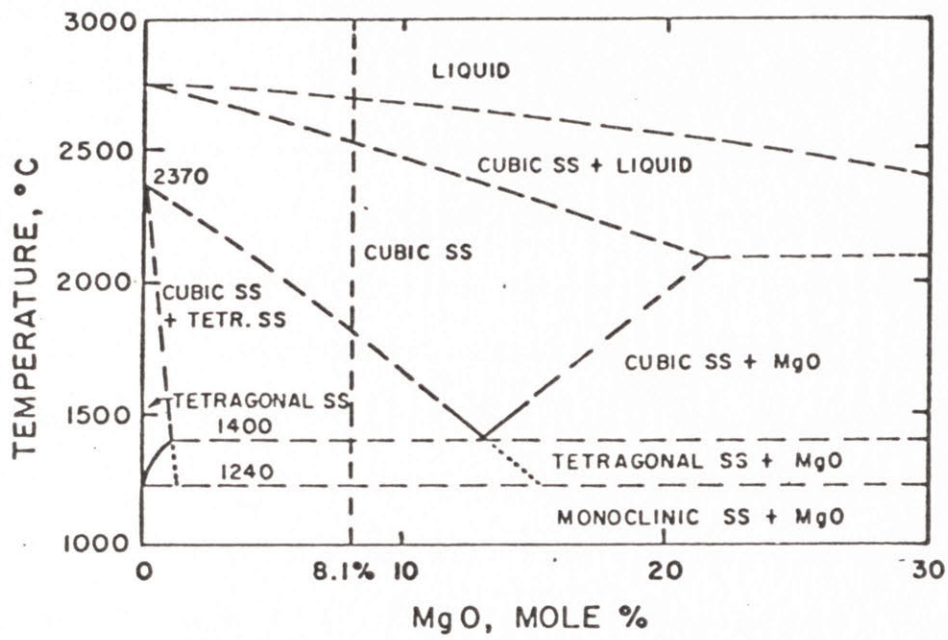


Figure II 1 The  $ZrO_2$ - $MgO$  system, after Grain.

fluorite cubic solid solution ( $C_{ss}$ ) region ( $\sim 1400^\circ\text{C}$ ). This is called partially stabilized zirconia. During cooling to room temperature the T $\rightarrow$ M transformation occurs and the volume expansion associated with the transformation partially compensates the thermal contraction of the  $C_{ss}$  during cooling. Adequate thermal shock resistance and improved strength resulted from this 2-phase alloy. Porter and Heuer (1979a) studied this composition and characterized the microstructure. At room temperature, two types of monoclinic particles are present, large intergranular grains ( $G.S. \gg 1$  micron) and small (about 0.4 micron) intragranular precipitates. In addition, even smaller tetragonal precipitates are found between intragranular monoclinic precipitates. The probable sintering and cooling steps necessary to produce this microstructure are discussed fully by Porter and Heuer. The important point is that in commercial binary  $\text{ZrO}_2$  alloys (partially stabilized zirconia) prior to 1975, tetragonal zirconia could exist and probably contributed to mechanical property improvement.

### II.A.3. Microstructures Containing T- $\text{ZrO}_2$

After the suggestion by Garvie et al. (1975) of the nature of the mechanical property improvement using T- $\text{ZrO}_2$  many groups began to intentionally produce microstructures that could retain T- $\text{ZrO}_2$  to room temperature. Five main microstructure types can be identified that do, or can, retain T- $\text{ZrO}_2$  to room temperature:

1. Single crystal ( $\text{Y}_2\text{O}_3$ ) and large grained (20-100 micron) polycrystalline binary ( $\text{Y}_2\text{O}_3$ , CaO, MgO) ceramic alloys with small (0.1-0.4 micron) intragranular T- $\text{ZrO}_2$  precipitates have been produced.

2. Fine grained 0.1-0.5 micron polycrystalline binary  $\text{ZrO}_2$  alloys can be fabricated in the T or T +  $C_{ss}$  region; the temperature, composition

and cooling rate can be adjusted to produce 90% T-ZrO<sub>2</sub> (by X-ray diffraction).

3. Fine grained 0.1-5 micron ceramic alloys with T-ZrO<sub>2</sub> contained as a minor phase in separate grains, the major phase being thermodynamically or kinetically stable with respect to incorporation of ZrO<sub>2</sub> have been produced, using major phases of Al<sub>2</sub>O<sub>3</sub>, spinel or mullite.

4. Directional solidification of near-eutectic binary or ternary compositions containing ZrO<sub>2</sub> or HfO<sub>2</sub> might produce alloys containing T-ZrO<sub>2</sub> (Kennard, et al.) or T-HfO<sub>2</sub> (Hulse). These microstructures can be similar in some respects to both type 1 or type 3 microstructures. Toughening has not been unambiguously linked to T-ZrO<sub>2</sub> or T-HfO<sub>2</sub> in this type of microstructure.

5. Plasma sprayed coatings based on ZrO<sub>2</sub> are gaining wide acceptance. This type can be similar to types 1, 3 and 4 microstructures. Plasma sprayed coatings may exhibit non-equilibrium microstructures due to the large change in P<sub>O<sub>2</sub></sub> from plasma gun to surface, and high cooling rates from the melt (Miller, et al.). Plasma sprayed coatings typically have some porosity (Bratton and Lau).

Type 1 microstructures can be produced by skull-melting<sup>\*</sup> in a high temperature C<sub>SS</sub> region to produce a single crystal, sintering or solution annealing a previously sintered polycrystalline sample in the C<sub>SS</sub> region; rapid quenching of the C<sub>SS</sub> to a lower temperature within the C<sub>SS</sub>-T region suppresses intergranular nucleation and growth of T and thereby enhances the nucleation rate of intragranular T precipitates. Single crystals are

---

\* Ceres Corp., Waltham, Mass.



available with  $Y_2O_3$  (Bender and Ingel) and the large grained material has been made and examined by Hannink 1978, Porter and Heuer 1977, and Garvie et al., 1978. Nearly fully tetragonal fine grained, 0.1 to 0.5 micron, tetragonal solid solution  $ZrO_2$  (microstructure type 2) have been produced by sintering or hot-pressing in the T or T +  $C_{ss}$  region with  $Y_2O_3$  (Gupta et al., 1977, Reith et al., Scott and Reed, 1979).

Other ceramic matrix materials can be used to maintain the T- $ZrO_2$  phase to room temperature. They include  $Al_2O_3$  (Claussen 1978, Lange and Green, 1981) mullite; spinel and ZnO (Claussen and Rühle, 1981). Most of these materials are two phase systems with a small volume fraction of  $ZrO_2$ . These alloys sometimes contain a small amount of a third "stabilizing" oxide. This can reduce the  $-\Delta G_0$  available for the T→M transformation when the sample is cooled. The zirconia grain size distribution and the spatial distribution of zirconia (i.e., is the  $ZrO_2$  grain isolated in the matrix material or is it adjacent to other  $ZrO_2$  grains?) seem to be important aspects of this type 3 microstructure to avoid macroscopic fracture. Most authors attempt to obtain the narrowest grain size distribution and most uniform spacial distribution (i.e., isolated  $ZrO_2$  grains) possible. P. Becker has intentionally made a bimodal  $ZrO_2$  grain size  $Al_2O_3$ - $ZrO_2$  alloy with the fine  $ZrO_2$  grains <1 micron and the large  $ZrO_2$  grains (3-10 microns) in an effort to produce microcrack toughening and crack branching (Rothman 1981). A second unusual microstructure has been reported by Claussen and Rühle (1981). This  $Al_2O_3$ -8 v/o  $ZrO_2$  alloy has large  $Al_2O_3$  grains >10 microns, which when growing entrap  $ZrO_2$  grains of size 0.1 to 0.8 micron within them. In addition, there are the more usual  $ZrO_2$



grains along the  $\text{Al}_2\text{O}_3$  grain boundaries. The exaggerated  $\text{Al}_2\text{O}_3$  grain growth in the presence of this volume fraction of zirconia might be attributable to sulfur impurities remaining from fabrication as sulfur seems to be associated with exaggerated grain growth in  $\text{Al}_2\text{O}_3$  (Cutler 1976).

#### II.A.4. Grain Size for T- $\text{ZrO}_2$ Retention Observations and Theories.

In most microstructures it is generally observed that fine  $\text{ZrO}_2$  particles tend to remain T and only coarser ones transform to M on cooling. Methods used to observe the phase distribution directly are TEM, X-ray diffraction and Raman scattering. Indirect methods include thermal expansion measurement and elastic modulus measurements, especially when microcracking might be present. Although observations of the "critical sizes" for room temperature transformation seem to be consistent for a given microstructure and author, they do not seem to be consistent between different matrix materials given the matrix elastic moduli and thermal expansion coefficients for type 3 microstructures even within the same research group (Claussen and Rühle 1981, Table 1). The elastic strain energy originating from thermal expansion mismatch modified by the T→M phase transformation can significantly influence the energetics for the phase transformation. In particular, the large volume increase (about 3% at 950°C) for the T→M transformation and associated distortion- al strains provide enough strain energy that the transformation cannot occur at the stress free equilibrium temperature,  $T_e$  (1150°C to about 700°C depending on chemical composition of the T phase). If the distortional strains were fully relaxed, but the dilatational strains

were accommodated elastically for typical particle shapes, the strain energy would be too high to allow transformation except at significant undercooling below  $T_e$ . The undercooling must be sufficient to make the chemical-free energy change,  $-\Delta G$ , which drives the transformation, greater than the strain energy change  $\Delta U$ . If both the dilatational and distortional strains were completely unrelaxed and accommodated elastically, then  $\Delta U$  may be larger than  $-\Delta G$  at any undercooling for typical dispersed  $ZrO_2$  particles. The conditions for transformation then depend on either deformation by slip or twinning within the transforming  $ZrO_2$ , plastic deformation in the matrix or matrix cracking to relax the misfit strains. Even in a very weak or compliant matrix some internal stress relief from slip or twinning may occur within the transforming  $ZrO_2$  particles to maintain coherency across the habit plane during transformation.

Both thermodynamic and kinetic (nucleation) hypotheses for the size dependence of transformation of T- $ZrO_2$  in ceramic matrices have been proposed. As M- $ZrO_2$  plates have been observed to grow extremely rapidly within individual grains, there are no kinetic growth hypotheses for the T→M size dependence. Thermodynamic hypotheses include:

1. The interfacial energies of the transformed particles, including twin boundary or fault energies, are higher for M than for the T  $ZrO_2$  (Garvie, et al., 1981, Lange and Green, 1981).

2. Slip or twinning within the transforming  $ZrO_2$  particles cause partial relief of the shear strains within the  $ZrO_2$  particles for larger particles but not at the particle/matrix interface and so there is a critical particle or grain size,  $d_t$ , above which transformation is



favorable (Evans, et al. 1981b).

3. Matrix or interfacial microcracking partially relieves the stresses for particles larger than a critical size,  $d_m$ , and this microcracking allows transformation (Lange and Green, 1981).

Kinetic (nucleation) hypotheses include:

4. Nucleation is heterogeneous and the population of nuclei depends on the particle volume. For fine particles/grains the transformation is nucleation limited by the absence of embryos and does not occur in some particles (Anderson and Gupta, 1981).

5. For T particles which are coherent precipitates in a cubic  $ZrO_2$  matrix, transformation only occurs at sizes large enough that coherency is lost; this could be related to the interfacial efficiency in nucleating the transformation or to surface energy differences (Hannink, 1978).

6. Nucleation is heterogeneous, rate controlling and occurs at dislocations (Olson and Cohen, 1976, Cohen and Wayman, 1981), the growth which is not rate controlling might be described by dislocation reactions (Olson and Cohen, 1976).

For fine powders (particles unconstrained by a matrix) the "critical size" for retention of T- $ZrO_2$  can be  $100 \text{ \AA}$  (Garvie 1965) whereas in dense materials it is more typically 0.1-1 micron. Approximate calculations, suggest that surface energy considerations (# 1) are not the dominant factor controlling the critical size for constrained particles. Significant amounts of hydroxyl ion impurities also occur in some T- $ZrO_2$  powders (Mitubashi, et al., 1974). Although initial considerations focused on microcracking in dense materials, attention has already switched to deformation mechanisms within the transforming  $ZrO_2$  particles (# 2) which can relax strain energy and allow transformation. This may be reasonable

since the distortional strains are large and slip and twinning more effectively relieve them whereas several radial microcracks in the matrix can relieve dilatational strains more effectively than distortional strains.

However, the arguments presented to date for strain energy relief based on either deformation or cracking are incomplete as they neglect the effect of particle size or nucleation and assume complete transformation of particles. The nucleation condition must depend on stress relief by deformation and appropriate nucleus shape; however it is difficult to understand a direct coupling between nucleation of the martensite and microcracks. In type 1 microstructures (partially stabilized  $ZrO_2$ ) in which there are coherent T particles in a cubic matrix, there appears to be a correlation between the particle size for loss of coherency and for transformation. However, the particle sizes at which transformation occurs for incoherent particles in fine grained T- $ZrO_2$  (type 2 microstructures) or other matrices (type 3 microstructures) are similar, so coherency is apparently not the dominant issue in preventing transformation.

For any of the proposed mechanisms the critical size for transformation would depend on undercooling, as the chemical driving force approximately depends on undercooling as  $-\Delta G \propto -\Delta S \Delta T$  (Figure II.2) In the simplest cases dependent on creating higher energy surfaces (including cracks), the critical size would depend on undercooling as  $d_c \propto \Gamma / \Delta S \Delta T - \Delta U$  where  $\Gamma$  includes surface energies, surface energy differences, or differences in strain energy terms which are proportional to particle area;  $\Delta U$  includes the difference in strain energy terms which are proportional to  $d^3$ . However, for many cases the dependence on undercooling



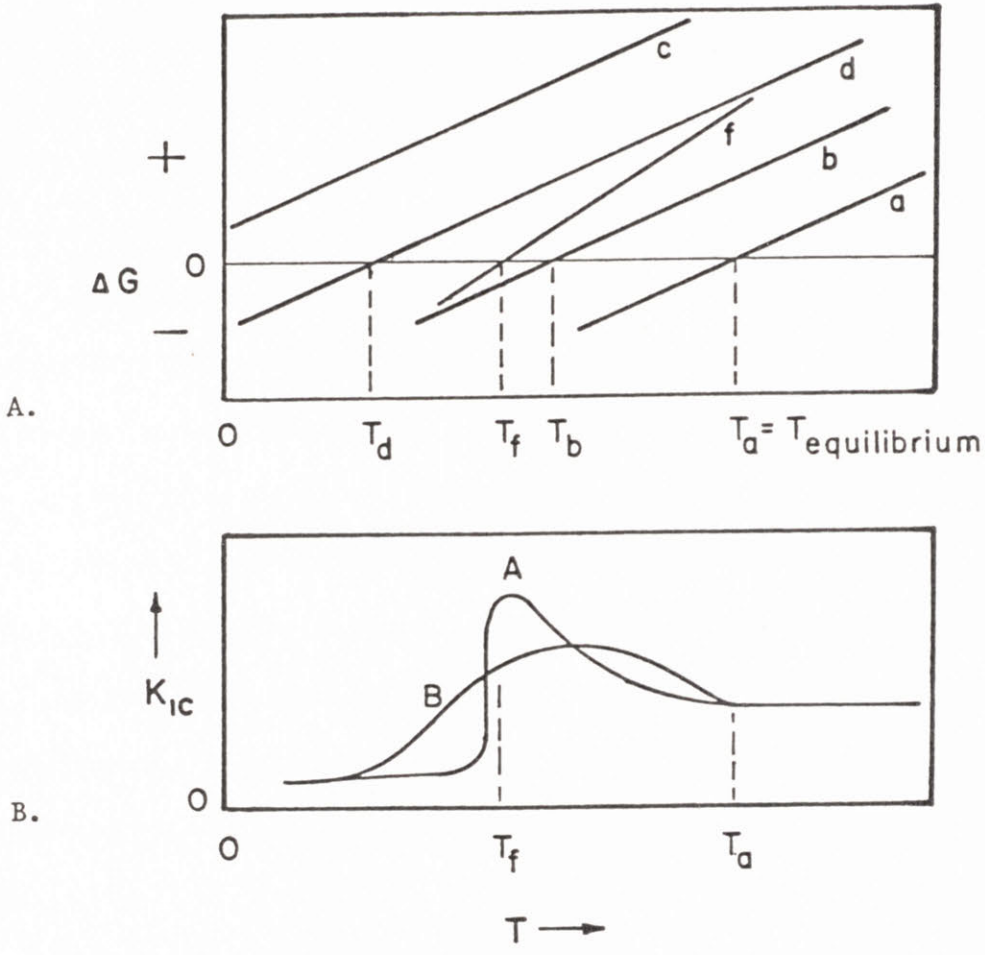


Figure II 2 A.  $\Delta G$  vs. temperature schematic  $T\text{-ZrO}_2 \rightarrow M\text{-ZrO}_2$ : free particle, a; dilational constraint on  $T\text{-ZrO}_2$ , b; dilational and shear strains unrelaxed, c; as for c but with shear strains partially relaxed by internal twinning, d; as for d but with  $\alpha_{\text{matrix}} < \alpha_{T\text{-ZrO}_2}$ , f.

B. Transformational toughening with conditions as for f above. Narrow  $\text{ZrO}_2$  grain size distribution, A; wide  $\text{ZrO}_2$  grain size distribution, B.

could be more complex and could depend sensitively on the chemical composition, both intentionally added oxides and impurities, and the microstructural details, such as the dislocation density or the density of microcrack initiation sites such as pores. The energetic considerations for both slip/twinning and for microcracking depend on volume fraction of T-ZrO<sub>2</sub> because the transformation of a nearby T-ZrO<sub>2</sub> affects the local stress state. In all cases applied stresses can alter the transformation energies and so the critical size for transformation. This means that appropriate applied stresses can facilitate the transformation and that cooperative effects are expected as well as simpler dependences on particle concentration.

Observations indicate that transformed ZrO<sub>2</sub> particles generally have stacking faults such as twins (Porter and Heuer, 1977, 1979). TEM examination indicates that not all transformed particles are associated with microcracks (Porter and Heuer 1977, Claussen and Rühle 1981). The second observation suggests that, at least in some cases the critical size for transformation,  $d_t$ , can be less than a critical size for microcracking,  $d_m$ .

There are no unambiguous experimental results that support thermodynamic hypotheses for the T-ZrO<sub>2</sub> grain size dependence. One experiment other than coherency observations seems to support the arguments for nucleation control. Heuer et al. (1982) have examined Al<sub>2</sub>O<sub>3</sub>-ZrO<sub>2</sub> alloys with both intergranular ZrO<sub>2</sub> grains and intragranular ZrO<sub>2</sub> particles and determined fraction M vs T for a given ZrO<sub>2</sub> grain/particle diameter as a function of temperature by TEM. For intergranular ZrO<sub>2</sub> grains, there seems to be a critical grain size,  $d_t$ , for transformation. This critical grain

size decreases with temperature. For intragranular particles, there is not a critical particle diameter for transformation. All particle diameter classes contain a mixture of T and M at both 273°K and 20°K. Annealing this microstructure at 1500°C for 30 hrs. increased the % tetragonal in all particle diameter classes of intragranular particles while the size distribution of the intragranular particles remained constant. Although a chemical explanation can be offered, Heuer et al. conclude that these observations indicate a nucleation phenomenon.

#### II.A.5. Mechanical Property Enhancement--Observations and Theories

Significant toughening has been obtained for several oxides with dispersions of T or M  $ZrO_2$ , including C- $ZrO_2$ ,  $Al_2O_3$  and mullite. The toughness depends sensitively on the  $ZrO_2$  size and can be a maximum at some (peak) particle size,  $d_p$  (Evans et al., 1981b). When the  $ZrO_2$  is very fine it remains T, the toughness is not particularly high, and there is little evidence for microcracking. At much larger sizes than  $d_p$  all the  $ZrO_2$  is essentially M, usually there is extensive microcracking, and often, but not always, samples spontaneously fracture. With finer  $ZrO_2$  particles the toughening is accompanied by significant strength increases.

Four reasons have been postulated for the toughening and strength effects:

1.  $K_{IC}$  increases because of the stress induced transformation of T- $ZrO_2$  in a local zone around the crack tip (Evans, et al., 1981b, Garvie et al., 1975, Porter et al., 1979b).

2.  $K_{IC}$  increases because of the stress induced microcracking and crack branching in a local zone near the crack (Green et al., 1973,



Claussen et al., 1977).

3. Fracture strength is increased by the high compressive stresses in a near surface zone which result from transformation induced by grinding or polishing (Garvie et al., 1978, Gupta, 1980).

4.  $K_{IC}$  can increase because of crack bowing and branching due to the elastic moduli and thermal expansion mismatch of the matrix and the  $ZrO_2$  (Evans and Laugdon, 1976).

Increases in strength and the measured fracture toughness due to the third effect have been demonstrated. The extent to which local stress induced transformation and microcracking contribute to toughening and high strength is unresolved and a matter of considerable controversy.

The greatest toughening is expected to occur for particle sizes just smaller than those which would spontaneously transform (or crack). This situation should give the largest transformation (or microcrack) zone around the crack tip. If only stress induced transformation were important, it would be expected that  $d_p \sim d_t$ . If both stress induced transformation and microcracking are important, then it may be that  $d_t < d_p < d_m$ , if  $d_t$  and  $d_m$  are different.

The toughness obtained will be strongly temperature dependent since the driving force for transformation depends on undercooling, Figure II.2. There may be little toughening near or above  $T_e$ , and the toughening will increase with undercooling. It may reach a peak and dramatically decrease below a temperature at which significant transformation and/or microcracking spontaneously occur, Figure II.2. The anticipated temperature dependence of  $K_{IC}$  would be quite different among the various mechanisms proposed to explain the toughening mechanism and size dependences and may

show a temperature hysteresis.

Different models for microcracking give different guidelines for developing microstructures. Evans and Farber (1981b) produced a microcrack model based on the energy absorption of circumferential microcracking occurring in the stress field of a macrocrack around spherical inclusions that are in tension from thermal expansion coefficient mismatch stresses. No radial microcracking is allowed, no compliance effect due to the microcrack is included and macrocrack-microcrack linking is ignored. From this specialized microstructure and these particular microfailure events the model predicts a high  $K_{IC}$  from a narrow distribution of inclusion sizes just under the size needed for spontaneous microcracking. If macrocrack-microcrack linking is allowed and if the inclusions have sharp corners the distribution of inclusion sizes may need to be wide to obtain high  $K_{IC}$ .

Hoagland and Embury (1980) have produced a model in which microcracks have a given fracture strength and when they crack they have a predetermined length that is constant for all microcracks. The microcracks are loaded by the stress field of a macrocrack and compliance changes due to the microcracking are included. The direction of propagation for individual microcracks was determined before loading and was random or preferentially textured parallel and perpendicular to the macrocrack. With random microcrack directions the stress at which microcracking occurs was given three distributions. Macrocrack-microcrack linking was not allowed. Macrocrack extension was defined somewhat arbitrarily by the length of contiguous microcracks resolved on the crack plane. Hoagland and Embury suggest the microcrack strength distribution ( $ZrO_2$  grain size distribution



or pore distribution) has little effect on toughening. Orienting the microcracks perpendicular to the macrocrack increased the toughening; this result is not surprising given the definition of macrocrack extension.

McClintock and Zaverl (1979) developed a model for brittle failure in polycrystalline bodies by microcrack linking based on a distribution of grain boundary strengths. No macrocrack was used other than that produced by the microcracks themselves. For uniaxial tension they found that improved failure strengths for the entire body resulted from a moderately narrow distribution of grain boundary strengths. If a similar model is used for a constant intensity stress field decaying as  $r^{-1/2}$ , a wider distribution of strengths is needed to produce considerable microcracking near the stress singularity (Evans et al., 1977). Implications for microcrack toughening via  $ZrO_2$  are not extremely clear but a wide distribution of microcrack strengths ( $ZrO_2$  grain sizes?) is probably preferred.

Most toughening models use the strain energy absorption of a single transforming/microcracking particle in a two-dimensional stress field near a propagating crack to find a strain energy release rate. By summation of all transformation/microcrack events and not allowing either the transformation or microcrack events to alter the crack tip stress field (compliance) for the next event, a simple computational scheme is achieved. An energy needed for crack propagation is derived based on the energy absorption of transformation/microcrack events occurring during a maincrack extension increment. Some models directly calculate the stresses near transformation/microcrack events to obtain  $K_{IC}$ 's, but are limited to two-dimensions. No single model includes both transform-



ation and microcrack toughening occurring simultaneously and none treat the essentially discrete three dimensional aspects of the problem appropriate for dispersed particles.

The two dimensional models developed for transformational toughening are the most satisfactory from a fracture mechanics viewpoint. Both  $G_C$  and  $K_{IC}$  calculations have been applied to T-ZrO<sub>2</sub> bearing alloys. The models assume the T→M transformation occurs in a zone around the crack tip; the zone size is the region where the applied stress is sufficient to make the free energy of transformation of T-ZrO<sub>2</sub> inclusions to M-ZrO<sub>2</sub> while constrained in an elastic matrix zero or negative. These calculations give the same result significant toughening can occur with T-ZrO<sub>2</sub> with only a small transformation zone (Evans et al. 1981a, Evans et al. 1981b). These calculations suggest the hypothesis that the maximum toughening occurs when the size of the T-ZrO<sub>2</sub> inclusions is at or slightly smaller than the inclusion size for the spontaneous T→M transformation with no applied stress,  $d_p \lesssim d_t$ . These calculations are unsatisfactory because they do not treat the T→M transformation kinetics and neglect the possibility of the reverse, M→T, transformation.

More recently improved calculations have been done in which the stress to stimulate the transformation is taken as a variable which is bounded by the thermodynamic limit, but depends on the transformation kinetics. The results preserve the feature that  $K_{IC}$  increases with transformation strain and zone size and that the zone size and  $K_{IC}$  increases as the stress necessary to stimulate transformation decreases (Evans and McMeeking, 1982). The increase in  $K_{IC}$  can also depend on the form of stress necessary for nucleation and growth of the T→M

transformation (Hutchinson, 1982). These models treat the transformation zone as homogeneous in two dimensions in order to calculate a  $\Delta K_I$  and thus neglect the effects of local stresses. For the more recent models the conditions required to initiate transformation are left as parameters. These parameters can be approximated using simple T-ZrO<sub>2</sub> inclusion size arguments but are not fully understood.

Experimentally obtained evidence regarding the contributions of transformation and/or microcracking to toughening is limited. Transformation around crack tips has been observed in TEM foils in partially stabilized ZrO<sub>2</sub> (type 1 microstructures) by Porter and Heuer (1977) and in situ with TEM by Rühle and Kraog (1981) in Al<sub>2</sub>O<sub>3</sub>-ZrO<sub>2</sub> (type 3 microstructures). The transformation zones are small <5 microns. Deconvolution of x-ray diffraction measurements of fracture surfaces of Al<sub>2</sub>O<sub>3</sub>-ZrO<sub>2</sub> also suggest a transformation zone size of <5 microns for toughened Al<sub>2</sub>O<sub>3</sub>-ZrO<sub>2</sub> (Claussen and Rühle, 1981). A dependence of toughness on T-ZrO<sub>2</sub>/M-ZrO<sub>2</sub> precipitate size has been assumed because aging studies at high temperature on type 1 microstructures (PSZ) show that toughness increases then decreases with increasing annealing (aging) time at temperature, Figure II-3. The low toughness at short annealing times may be a combination of fine precipitates and a low volume fraction of T-ZrO<sub>2</sub> phase. The higher toughness at longer annealing times may be a combination of larger T-ZrO<sub>2</sub> precipitates and a higher volume fraction of T-ZrO<sub>2</sub> phase, as this microstructure is being produced by a non-equilibrium, sub-eutectoid decomposition reaction. For type 2 or 3 microstructures high strength and toughness with fine T-ZrO<sub>2</sub> grains and lower strength with larger ZrO<sub>2</sub> (T or M?)

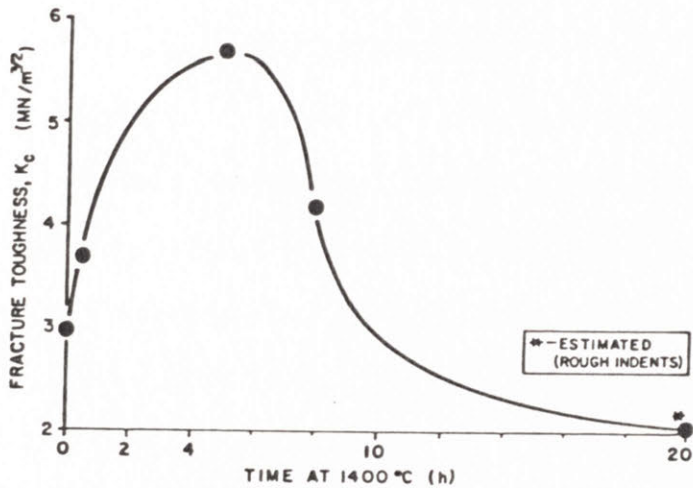
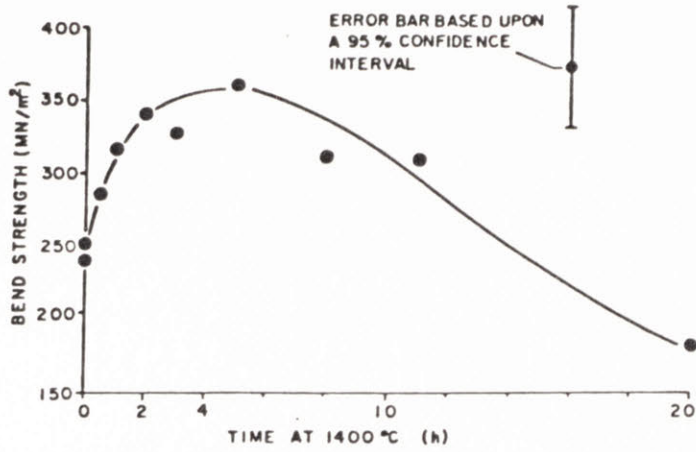


Figure II 3 Bend strength and critical stress intensity of Mg-PSZ (type 1 microstructure) as a function of annealing (aging) time at 1400°C, after Porter and Heuer (1979). The curves would imply a peak in bend strength and fracture toughness as a function of T-ZrO<sub>2</sub> precipitate (grain) size if the volume % of T-ZrO<sub>2</sub> was constant, the volume % of T-ZrO<sub>2</sub> is probably increasing with annealing time.



grains has been interpreted as a  $K_{IC}$  vs.  $ZrO_2$  grain size relation such as could be assumed from figure II-3. Measurements of high  $K_{IC}$  or work of fracture on PSZ (Green and Nicholson) and  $Al_2O_3-ZrO_2$  (Claussen et al. 1977) have been attributed to microcrack toughening as these materials had larger T- $ZrO_2$ /M- $ZrO_2$  inclusion/grain sizes and had lower fracture strengths than materials in which transformation toughening has been shown to occur.

#### II.A.6. LITERATURE SUMMARY

Tetragonal zirconia can exist in ceramic alloys to temperatures as low as 20°K.  $ZrO_2$  precipitate, grain or particle sizes of less than 1 micron are necessary to maintain the T phase to room temperature. There is no adequate theory to account for the T- $ZrO_2$  size for transformation to M- $ZrO_2$ . The martensitic transformation of T- $ZrO_2 \rightarrow$  M- $ZrO_2$  can enhance the mechanical properties of ceramic alloys containing  $ZrO_2$ . T- $ZrO_2 \rightarrow$  M- $ZrO_2$  particle transformation near crack tips has been demonstrated. Microcrack toughening is also probably occurring in some microstructures. The modelling of transformation and/or microcrack toughening is incomplete; different models predict different  $ZrO_2$  grain size distribution effects.

## II.B. INTENDED RESEARCH

Most microstructure types presented in the literature review were developed to improve the mechanical properties. The research presented in the following sections had several goals:

1. to improve the mechanical properties of an optical quality ceramic for IR wavelengths between 3-5 microns,
2. to provide experimental information on fracture toughness when the volume fraction and/or the grain size distribution of  $ZrO_2$  was varied in a single well-characterized matrix material, and
3. to develop a single three-dimensional model for fracture toughness including both transformation and microcrack toughening.

The use of a material for optical purposes places constraints on the porosity and purity levels for any ceramic. When using a two phase material, the index of refraction mismatch must be minimized, the volume of second phase minimized, the size of the minor second phase minimized, the grain size distribution should be narrow and the shape of the second phase should be nearly spherical if the two phases indices of refraction are isotropic and no preferential grain/precipitate texturing occurs (see Appendix A).

Several systems appeared to have potential for toughening at the start of the program (Musikant, 1978). Some potential systems were binary zirconia alloys of microstructure types 1 or 2, or a  $ThO_2-ZrO_2$  binary alloy of microstructure type 3. The  $ThO_2-ZrO_2$  binary had the advantage of allowing the  $ZrO_2$  v/o to be varied independent of composition, and hence  $\Delta G_o$ , unlike microstructure types 1 and 2. Pure  $ThO_2$  is cubic, and transparent to a wider range of IR wavelengths and the IR cutoff decreases in wavelength more slowly with increasing temperature than does  $C_{SS}-ZrO_2$ . In

addition,  $\text{ThO}_2$  was matrix material unexplored for  $\text{ZrO}_2$  toughening.

$\text{ThO}_2$  is not a good matrix material for optical quality  $\text{ZrO}_2$  bearing ceramics for two reasons: the index of refraction mismatch between the two oxides is large (about 4%), and  $\text{ThO}_2$  is radioactive. Because of the index mismatch, as well as for mechanical property considerations, it was initially thought necessary to obtain  $\text{ZrO}_2$  grain/particle sizes significantly below 1 micron. This put a premium on powder processing. If the thermodynamic theories for the size effect for the retention of T- $\text{ZrO}_2$  and its coupling to toughening theories were true, then pure  $\text{ZrO}_2$  would give a higher  $K_{\text{IC}}$  than any T- $\text{ZrO}_2$  solid solution using  $\text{CaO}$ ,  $\text{Y}_2\text{O}_3$ , etc. as the  $\text{ZrO}_2$  grain size decreased. The smallest grain size possible was needed for optical scattering considerations. The effect of alloying with other oxides on the index of refraction of T- $\text{ZrO}_2$  or  $\text{C}_{\text{SS}}\text{-ThO}_2$  was not clearly apparent, thus only the  $\text{ThO}_2\text{-ZrO}_2$  binary was studied in detail.

Because of the high atomic number of thorium (90), thorium oxide has a large absorption coefficient for X-rays (Cullity) and electrons. The difference in absorption coefficients for  $\text{ZrO}_2$  and  $\text{ThO}_2$  prevents the use of X-ray diffraction for  $\text{ZrO}_2$  phase identification in the bulk. Thin TEM foils (200 Å - 800 Å) must be used in Transmission Electron Microscopes of limited power (100 Kev).



### III. SAMPLE PRODUCTION

#### III.A. PROCESSING LITERATURE REVIEW

##### III.A.1. $\text{ThO}_2\text{-ZrO}_2$ Binary Phase Diagram

A suggested  $\text{ThO}_2\text{-ZrO}_2$  phase diagram is presented in Figure III.1 (Duwez and Loh, Mumpton and Roy). There are two options open for producing a toughened  $\text{ThO}_2\text{-ZrO}_2$  alloy with fine, 1 micron,  $\text{ZrO}_2$  grain sizes.

1. Produce a microstructure similar to type 1 by skull melting or by annealing previously sintered  $\text{ThO}_2\text{-ZrO}_2$  in the single phase  $\text{C}_{\text{SS}}$  or two phase  $\text{C}_{\text{SS}}\text{-ZrO}_2 + \text{C}_{\text{SS}}\text{-ThO}_2$  region, at temperatures greater than  $2200^\circ\text{C}$  with the  $\text{ZrO}_2$  content at about 50 mole % or less. Rapid quenching into the two phase  $\text{T-ZrO}_2 + \text{C}_{\text{SS}}\text{-ThO}_2$  region between  $1500^\circ\text{C}$  to  $1200^\circ\text{C}$  might produce a high nucleation rate and small coherent or semi-coherent  $\text{T-ZrO}_2$  precipitates.

2. Use advanced powder processing techniques to make a type 3 microstructure. If the powders have a small particle size, then sintering or hot-pressing in the  $\text{T-ZrO}_2 + \text{C}_{\text{SS}}\text{-ThO}_2$  region might produce the necessary grain size and lack of porosity.

Option 1 was not pursued as the high temperature ( $>2200^\circ\text{C}$ ) oxidizing furnaces were not immediately available, the size and coherency of the postulated  $\text{T-ZrO}_2$  precipitates was open to question and radioactive contamination via vapor phase transport due to the high temperatures needed seemed possible.

Option 2 was pursued as oxidizing furnaces for lower temperatures ( $\sim 1700^\circ\text{C}$ ) were available, as was an induction heated hot-press. The author was familiar with traditional ceramic powder processing and densification techniques, hence success seemed more likely with option 2. Airborne radioactive contamination due to the fine particle size needed in the

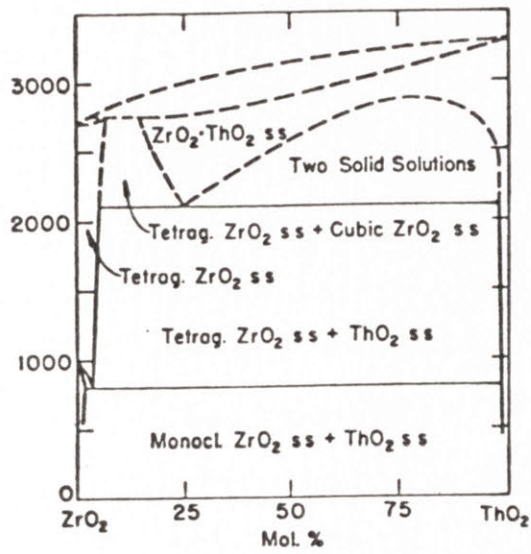


Figure III 1 The ThO<sub>2</sub>-ZrO<sub>2</sub> system, suggested. After Duwez and Loh.

powder was still a problem.

### III.A.2. Sintering and Hot Pressing - General

Sintering and hot pressing are methods that use ceramic powder (particle sizes can range from 50 Å to about 10 microns) to form solid bodies. Sintering utilizes the slight surface energy difference between a powder and a solid body to produce a body with less surface area via solid state, liquid phase or vapor phase diffusion. In some systems (glasses) viscous flow or plasticity can also be important. Hot pressing at least adds pressure transmitted through the solid to the driving force for densification (Coble 1970). In addition, the applied pressure may aid in particle/agglomerate rearrangement for better packing at high temperatures during initial stage sintering.

Engineering criteria for successful sintering or hot pressing to full density for oxide materials are: fine particle size, small agglomerate size (several to thousands of particles that, by physical, electrical or chemical bonding, act as a single physical and mechanical unit), regular packing of agglomerates, few density gradients in the unsintered but compacted powder mass, and a high density for the unsintered body. During final stage sintering, the pores should contain no gas or a gas that is soluble in the body and/or diffuses rapidly. If grain growth occurs too rapidly during the final stage, pores are often trapped within grains. After this entrapment densification is usually much slower as diffusion rates for the gas or vacancies through the lattice are usually much slower than along the grain boundaries.

Hot pressing is useful in avoiding pore entrapment. The applied pressure increases the densification rate for any temperature and thus



lower temperatures can be used to densify bodies in reasonable time periods. Grain growth rates are not usually affected by pressure, but commonly drop as temperature is lowered. By adding pressure and reducing temperature hot pressing retains reasonable densification rates while reducing pore entrapment by grain growth. Hot pressing is thus very useful in producing dense ceramics with small grain sizes. For two phase materials with the minor phase greater than about 10%, pore entrapment is less likely because the second phase inhibits grain boundary motion.

There are three general types of hot pressing (Leipold): (1) uniaxial, using graphite, metal or ceramic dies, (2) isostatic, using a fluid, usually a gas, to transmit pressure, and (3) pseudo-isostatic (Lange and Terwillinger, 1973), where a uniaxial die contains a pressure transmitting powder (graphite or boron nitride) or fluid (glass). When open porosity is present, iso- and pseudo-isostatic hot pressing need a pressure transmitting seal around the powder body being densified. Evacuation of the gas in the porous body is also recommended.

### III.A.3. Densification of $ZrO_2$ and $ThO_2$

To obtain the high density and the fine grain sizes necessary for optical properties and the retention of the T- $ZrO_2$  phase, normal powder production and processing are ineffective. Brook (1981) reviewed  $ZrO_2$  preparation and Claussen and Rühle (1981) briefly noted some processing methods used for ceramics containing T- $ZrO_2$ .

Both  $ThO_2$  and  $ZrO_2$  are good oxygen ion conductors, so under no conditions do we expect that oxygen diffusion would be the rate controlling step for sintering. At the fine grain sizes needed, we might anticipate that cation transfer via grain boundary diffusion would be faster than

cation transfer by lattice diffusion. Under some conditions of temperature and  $P_{O_2}$ ,  $ZrO_2$  and  $ThO_2$  can become electronic conductors, and can become slightly oxygen deficient. We do not anticipate much change in stoichiometry from grain boundary midpoint to neck surface. The free energy change needed to produce extensive non-stoichiometry in this system is probably much larger than the free energy driving forces from sintering.

Mazdiyazni et al. (1967) have been able to produce fine  $ZrO_2-Y_2O_3$  powders from alkoxides. After preparation of the organo-metallic complexes, exposure to water produces an oxide. The oxide at this stage has a particle size of about 50 Å. After calcination at 350°C for 30 minutes, the particle size is 100 to 400 Å. This material has a registered trademark, Zyttrite<sup>®</sup> and has been used in subsequent studies. Haberko (1979) recently coprecipitated Zr + Y hydroxides from chloride salts. Washing with alcohol proved critical in avoiding hard agglomerates. Dole et al. (1978a) also recommend washing hydroxide precursors prior to calcining with organic fluids.

Rhodes and Haag (1970) produced a massive study on sintering and hot pressing Zyttrite<sup>®</sup>. The main observation was that to obtain the full benefits of the small particle size, powder agglomerates must be eliminated. When agglomerates are avoided, a 0.2 micron grain size 99.5% dense  $ZrO_2$  solid solutions can be obtained by sintering at 1100°C (Rhodes 1981). This is hundreds of degrees less than usual  $ZrO_2$  sintering temperatures, and a higher density than is usually obtained. Both Scott and Reed (1979) and Haberko have also shown the importance of eliminating agglomerates to obtain dense  $ZrO_2$  at low sintering temperatures. These authors also stress the importance of eliminating chlorine ion impurities from

their chloride derived powders, evidently because chlorine may promote gas phase transfer during calcination and initial stage sintering.

Fine grain sized dense  $\text{ThO}_2$  can be obtained by the sol-gel method (Furgeson et al., 1964). Bannister (1968) has measured particle sizes in  $\text{ThO}_2$  gel (150 Å) and reviewed the sintering mechanisms (1975) in  $\text{ThO}_2$  gel, concluding grain boundary diffusion of Th was rate controlling. Currently,  $\text{ThO}_2$  microspheres are made at Oak Ridge by a form of hydroxide precipitation via urea decomposition.

### Summary

Fine grain size dense ceramic bodies of  $\text{ZrO}_2$  or  $\text{ThO}_2$  can probably be obtained from alkoxide or hydroxide precursors. Elimination of agglomerates is crucial to both methods. Washing hydroxide gel with organics seems to be important in eliminating agglomerates. Hot pressing can achieve higher densities and finer grain sizes than sintering.

## III.B. EXPERIMENTAL METHOD - PROCESSING

### III.B.1a. Powders Derived from Hydroxides

Pyrex<sup>\*</sup> glassware and teflon coated magnetic stirring bars were used for the aqueous chemistry steps. The Millipore glass filter<sup>\*\*</sup> apparatus was used during the nitrate solution filtration. A porcelain buchner funnel or a Pyrex glass fritted filter were used in the hydroxide filtration step. Fused silica crucibles were often used during calcining and glass stirring rods were often used to manipulate the nitrate powders or hydroxide gels. This labware was cleaned with concentrated hydrochloric acid

---

\* Corning Glass Works, Corning, N.G.

\*\* Millipore, Bedford, MA.



or concentrated chromic-sulfuric acid, washed with distilled water and dried with acetone. Polypropelene jars used were washed with distilled water and acetone.

Since thorium is radioactive, standard precautions were taken. Whenever loose powder was not in a container, it was in a fume/dust hood. Two layers of gloves, a lab coat and a dust mask were worn when loose powder was being handled, and often a face mask or goggles were worn when acid was present. To the greatest extent possible, powder which could become airborne was kept moistened by liquid to prevent airborne contamination problems.

Figure III.2 is a flow chart of the "best" sample production method. Known masses of reagent grade thorium nitrate and zirconyl nitrate were heated to greater than 1000°C in air for one hour to convert the hydrous nitrates to oxides. The water of hydration was determined by weighing the remaining oxide. Appropriate amounts of thorium nitrate and zirconyl nitrate for a given mole %  $ZrO_2$  in the end product oxide ( $O^m/o$  to  $46^m/o$ ) were dissolved into distilled water. Concentrations of salt solutions varied by a factor of 3; from 0.24 molal to 0.73 molar for  $O^m/o$  Zr and 0.3 molal to 0.9 molal for  $46^m/o$  Zr with intermediate  $^m/o$  Zr concentrations at molal values between these two limits.

The thorium nitrate dissolved easily but the zirconyl nitrate often would not dissolve completely under a moderate stirring action provided by a teflon coated magnetic stirring bar. Lumps of zirconyl nitrate were usually broken by hand using either a glass stirring rod, a glass stirring rod covered by a rubber "policeman" or a wooden tongue depressor. Early

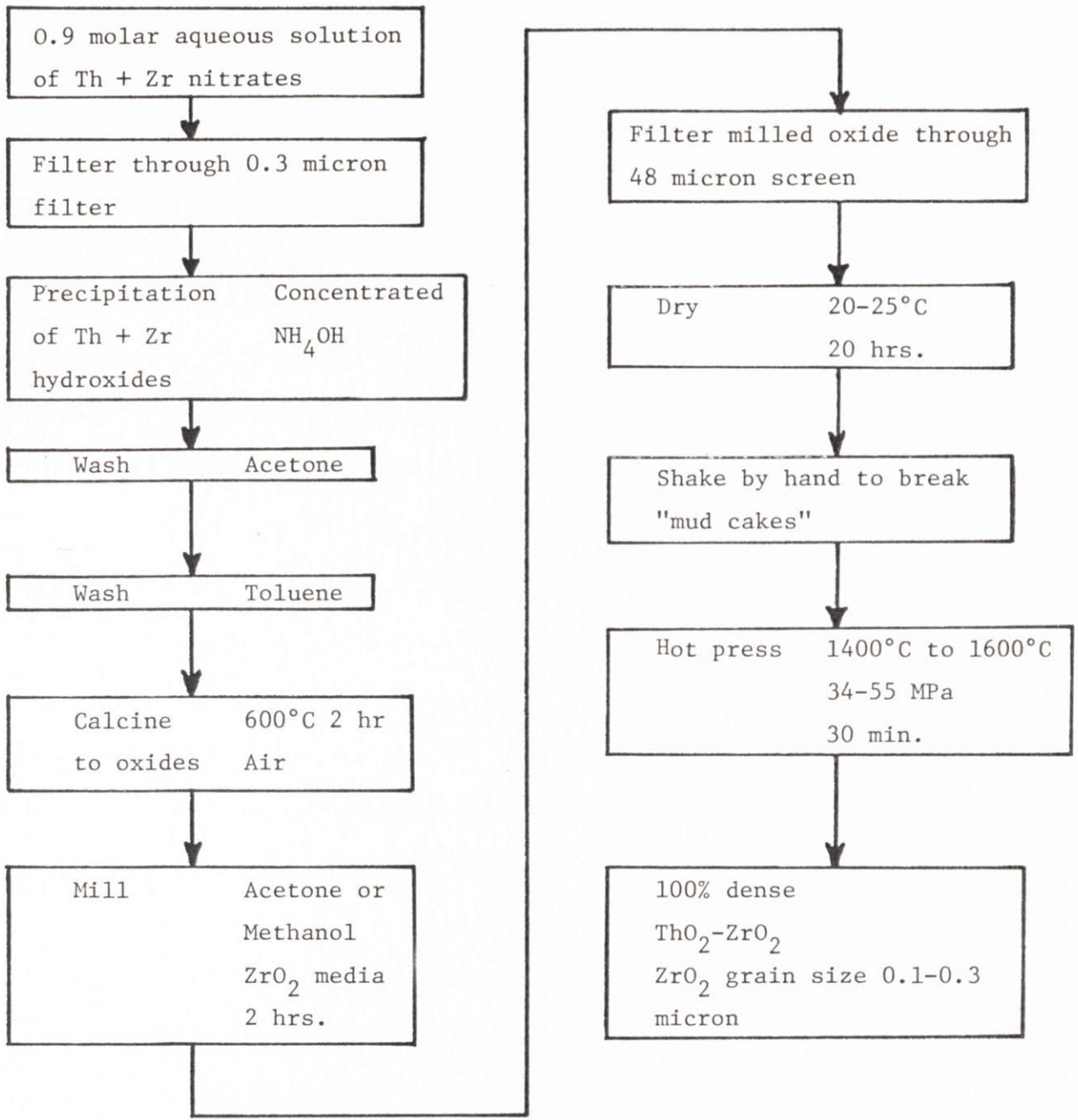


Figure III 2 - Flow chart for powder and sample preparation from hydroxide precursors

samples were produced directly from nitrate solutions. In later samples either the zirconyl nitrate was filtered through a 0.2 micron teflon filter\* (H-85-J, H-85-K, H-85-L) before adding the thorium nitrate, or the entire nitrate solution was filtered through a 0.3 micron nitro-cellulose filter.

The nitrate solution was precipitated into concentrated reagent grade ammonium hydroxide or concentrated ammonium hydroxide diluted with an equal volume of distilled water. An extremely large excess of ammonium hydroxide, a volume equal to the nitrate solution, was used. The ammonium hydroxide was used in pint bottle quantities to minimize the potential for ammonia evaporation. If a small amount of ammonium hydroxide is stored in a large container that is repeatedly opened to the atmosphere, then the concentration of the ammonium hydroxide will be reduced. The precipitation technique was varied from rapid mixing (75 ml/1 sec) of concentrated reactants to slow drip precipitation (75 ml/2 hrs) of low molal nitrate solutions into diluted ammonium hydroxide.

Batch size varied from 75 ml to 150 ml of nitrate solution. During the slow precipitation, the ammonium hydroxide and the hydroxide precipitate were stirred by a teflon coated magnetic stirring bar. The precipitation was usually performed at room temperature, but several samples were precipitated at 0°C by immersing the ammonium hydroxide and nitrate solutions in ice baths prior to precipitation.

The hydroxide precipitate was separated from the liquid products and excess ammonium hydroxide by filtering. An 11 cm buchener funnel with

---

\* Millipore Corp., Bedford, MA.



11 cm black label filter paper was used with most sample batches, while in later samples a glass fritted filter was used. A water aspirator connected to a filter flask provided a vacuum to speed the filtering.

Most hydroxide precipitate was washed with acetone then toluene. However, some material was not washed, and other material went through washing cycles of water, acetone, toluene and acetone. Early hydroxide batches were washed in the buchner funnel, the hydroxide gel and washing fluid stirred with a glass stirring rod or wooden tongue depressor. The hydroxide gel occupied about half the volume of the funnel, and the washing fluid was added until the funnel was full. The hydroxide gel was washed three to four times with reagent grade acetone, then another three times with reagent grade toluene. Between each wash, the hydroxide was vacuum filtered. Later hydroxide batches were washed by transferring the gel to a large 300 ml beaker then adding the washing fluid. Stirring was accomplished with a magnetic stirring bar. Again the gel was filtered between washes, three acetone and three toluene.

The resulting hydroxide gel was calcined to an oxide under various conditions, but most was calcined at 600°C or 750°C in air for two hours. The extremes of calcining temperature were 450°C and 900°C. Some early hydroxide batches were calcined under a slight vacuum of about 100 microns of pressure. The furnace used for the vacuum calcining was a rapid quench furnace utilizing a fused silica furnace tube which was used for direct visual observation of the calcining powder. Fused silica boats and aluminum foil boats were used to hold the calcining powder in this furnace. Most hydroxide gel was calcined in commercial laboratory

furnaces under ambient atmosphere. Fused silica crucibles with alumina covers were used with the covers slightly ajar to allow the decomposition products to escape.

After calcination, the oxide powder for most of the samples was milled, either in a vibratory mill for 2 to 20 hours, or in a labscale "attrition" mill for 2 hours. Stabilized  $ZrO_2$  media 3/16" in diameter was used. All milling was done in a fluid, either acetone, methanol or, in one case, distilled water with the Ph adjusted to about 1.5 with HCl. The attrition milling was performed by placing two layers of  $ZrO_2$  media, a 10 to 20 gram powder charge and the milling fluid in a 2" polypropelene jar with a magnetic stirring bar to provide the milling action.

For early samples, the organic fluid was allowed to evaporate and milling media was removed. In later samples the powder slurry was washed through a 48 micron nylon screen to remove the milling media, milling media debris and large agglomerates. The organic fluid was either burned or allowed to evaporate for 20 hours. One sample's powder was passed through both 48 micron and 15 micron nylon screens as an aqueous slurry of a pH of about 1.5. The water was eliminated from this slurry by repeated dilution with acetone; the acetone was allowed to evaporate.

The soft "mud cake" structure left from all the fluid evaporations was broken by hand, in early samples by a spatula as the powder was poured into a die and in later samples by shaking the powder while it was in a polypropylene jar before any die pressing.

### III.B.1b. Powders produced from oxalates

Thorium nitrate was dissolved in distilled water and an appropriate

mass of unmilled, unstabilized  $ZrO_2$  with an average particle size of 0.3 micron was added to produce powders with 0<sup>m</sup>/o to 20<sup>m</sup>/o  $ZrO_2$  remainder  $ThO_2$  in 5<sup>m</sup>/o  $ZrO_2$  increments. The agglomerated  $ZrO_2$  was dispersed in the nitrate solution by stirring only. This suspension was slowly dripped into a stirred excess of a concentrated aqueous solution of oxalic acid, precipitating thorium oxalate around the  $ZrO_2$  agglomerates. The precipitate was filtered and washed while in the filter with acetone and toluene.

Simultaneous precipitation of thorium and zirconyl oxalate from thorium/zirconyl nitrate solutions was attempted. The thorium/zirconyl nitrate solution was slowly dripped into a stirred, saturated aqueous solution of oxalic acid (75 ml/1/2 hour to 2 hours). The precipitate was filtered and washed with acetone and toluene. Precipitation of zirconyl oxalate, from dilute and saturated aqueous solutions of zirconyl nitrate, and zirconyl chloride, was attempted. Concentrated aqueous solutions of oxalic acid were used. The acid was introduced into the nitrate and the nitrate into the acid. After filtering and washing, the oxalate precipitate was calcined at 750°C in air for 2 hours in fused silica crucibles. None of the oxalate derived powders were milled.

### III.B.1c. Densification of powders

#### (i) Sintering

Oxide powders derived from both hydroxide and oxalate precursors were used for sintering studies to obtain dense samples for subsequent characterization. Oxalate-derived powders were uniaxially die pressed at 60 MPa in a single acting piston steel die lubricated on the die and piston surfaces with oleic acid. A small amount of acetone was used



as a powder lubricant/binder. These pressed pieces were then wrapped in aluminum foil, placed in a rubber bag, the air evacuated from the bag and isostatically pressed at 200 MPa.

Powders derived from hydroxides were uniaxially die pressed at 7 MPa in a graphite die lined with grafoil<sup>\*</sup> using a small amount of acetone as a powder binder/lubricant. These pellets were isostatically pressed in a manner similar to the oxalate-derived samples, but at a higher pressure, 275 MPa.

The samples derived from oxalates were wrapped in platinum foil (not air-tight) and sintered at 1700°C in air for 24 hours. The furnace was at temperature and the green pieces were introduced to the hot zone in less than 15 minutes. The samples were withdrawn from the hot zone in 20 to 30 minutes. A horizontal molybdenum wound H<sub>2</sub> furnace with an alumina tube with manual temperature control was used. The temperature was read by a Pt-10% Rh, Pt thermocouple and potentiometer checked by an optical pyrometer.

The isostatically pressed pellets of powder derived from hydroxides were sliced into wedge-shaped sections with a razor blade prior to sintering. The sections were sintered in a vertical molybdenum wound H<sub>2</sub> furnace with an alumina tube and manual temperature control at 1500°C and 1600°C for times between 0.5 and 2 hours. The sintering atmosphere was either O<sub>2</sub> or high purity H<sub>2</sub> dried by silica gel and a liquid N<sub>2</sub> cold trap to eliminate residual H<sub>2</sub>O and thus O<sub>2</sub>. In oxidizing atmospheres, the samples were suspended by Pt-10% Rh wires; in reducing atmospheres the

---

<sup>\*</sup> Union Carbide, Chicago, Ill.

samples were contained in an alumina crucible suspended by tungsten wire. The temperature was monitored by an optical pyrometer or a Pt-10% Rh, Pt thermocouple and potentiometer. In reducing atmospheres, the thermocouple was encased in an alumina thermocouple protection tube. Insertion and withdrawal times from the hot zone were between 15 and 40 minutes.

(ii) Hot Pressing

Hot pressing was performed in an inductively heated vacuum hot press<sup>\*</sup> operating at 10 kilo Hertz. Both temperature and pressing pressure were controlled manually. Graphite dies were used, a 1" inner diameter, 6" outer diameter die of ATJ graphite and a 2" inner diameter, 6" outer diameter die of HPD - 1 Poco graphite<sup>+</sup>. Both dies were machined such that a gap of about 12 thousandths of an inch was available for graphoil<sup>++</sup> which lined the die wall and plunger faces. In later sample runs, the die and graphoil were washed with methanol prior to use.

Temperature measurement was by optical pyrometer or a Pt-10% Rh, Pt thermocouple encased in an alumina protection tube. The optical pyrometer was focused on the die wall side, midway down the die, the highest temperature taken as the sample temperature. Observation port windows were cleaned every second run. On several runs, a mirror made from a glass slide and sputtered Pt was used to sight into a 1/8" hole drilled to mimic a "black body radiator."

At room temperature, a pressure of 60 MPa was applied to the die to compact the powder, then released. The chamber was brought to a

---

<sup>\*</sup>GCA, Vacuum Industries Inc, Somerville, Ma.

<sup>+</sup>Union Oil Co., Poco, Decatur, Tx.

<sup>++</sup>Union Carbide, Chicago, Ill.

vacuum of less than  $10^{-4}$  torr before heating began. A period of 15 minutes to 2 hours was necessary for this. During heating, a hold at about  $600^{\circ}\text{C}$  for 15 minutes to 1 hour was usually necessary to complete outgassing to about  $5 \times 10^{-4}$  torr. Various pressing pressure and heating rate cycles were used. Typically, as the temperature neared about  $800^{\circ}\text{C}$ , the pressing pressure was slowly increased at about 20 MPa/minute, while the temperature increased at 10 to  $30^{\circ}\text{C}/\text{minute}$ . In less than an hour, the temperature was raised to between  $1400$  to  $1700^{\circ}\text{C}$ ; temperature and pressure were held as constant as possible. Densification was monitored by a micrometer head mounted to the load train. When the run was complete, the power was shut off and the die and sample were allowed to cool. Typically, the pressing pressure (34 to 55 MPa) was reduced slowly and was zero when the die cooled to about  $1200^{\circ}\text{C}$ .

Several experiments were modifications of the usual sintering or hot pressing procedures. Two samples were uniaxially pressed in a graphite die to 7 MPa, and heated to  $900^{\circ}\text{C}$  in air for two hours to eliminate carbon impurities and volatile compounds. One was then heated for two hours in a high purity  $\text{H}_2$  atmosphere that had been dried by silica and liquid  $\text{N}_2$  cold trap. These samples were then wrapped in Pt foil and hot pressed. Only a small amount of shrinkage occurred during these firings, so that the sample plus the foil were snug in the hot pressing die.

Several sintered samples that had reached greater than 93% were pseudoisostatically hot pressed. The sintered samples were wrapped in Pt foil, embedded in carbon powder in a uniaxial hot pressing die and hot pressed at about  $1600^{\circ}\text{C}$ . The carbon provides some lateral constraint but does not flow like a liquid so the stress on the sample is not



completely isostatic.

### III.B.1d. Annealing

Annealing was performed for two reasons: to increase the grain size, and to correct the oxygen deficient stoichiometry of hot-pressed samples. Temperatures used in annealing ranged from 900°C to 2300°C in atmospheres of air, oxygen, nitrogen, argon, normal "welding grade" hydrogen, high purity hydrogen and carbon monoxide. In "inert" or reducing atmospheres, the samples were often wrapped with graphoil or carbon felt during annealing. The high purity hydrogen was dried by silica gel and a liquid nitrogen cold trap. The carbon monoxide was dried by silica gel and an acetone-solid carbon dioxide cold trap. The gas flow system was constructed with copper tubing and swageloc fittings; the gas exit had a two flask bubbler to stop any back diffusion of air. The cold trap was simply twenty turns of copper tubing placed in a large-mouth dewar.

Several furnaces were used for annealing. For air atmospheres and temperatures 900°C to 1200°C, commercial lab furnaces were used. Chromel-alumel thermocouples were sometimes used to check the temperature calibration of these furnaces. A carbon element resistance furnace, with the furnace tube being the element, was used for temperatures from 1200°C to 2300°C in argon atmosphere. Temperature in this furnace was controlled manually. The hot press and die were used for several annealings at 1500 to 1600°C in a vacuum. Temperatures in the carbon tube furnace and hot press were measured by an optical pyrometer.

The furnace used for most annealings was an alumina tube with molybdenum windings protected from oxidation by hydrogen. Temperature was controlled manually via a variac for most annealings, but during the

last series of annealings, the temperature was controlled with an "on-off" controller\* switching between two variacs with slightly different power settings. The power settings were adjusted manually for each temperature. The temperature was measured by Pt, 10% Rh-Pt thermocouples protected from the reducing atmospheres by alumina protection tubes. The thermocouple leads were run through a 0°C ice bath and voltage read with a potentiometer\*\* or a digital voltmeter.+

In addition to the graphoil or carbon felt often used with reducing atmospheres, a mixture of carbon and unstabilized zirconia was used to buffer the CO gas equilibrium. Gas flow rates for hydrogen and carbon monoxide were low, less than  $2 \times 10^{-3}$  cm/sec over the sample. Before introduction or withdrawal of the sample from the hot zone (when using reducing gases) in the hydrogen-moly furnace, the existing gas was purged for about 5 minutes by argon. The samples were held in an alumina crucible and lowered, raised, and often suspended by a tungsten wire. In the last annealings, the crucible was supported in the hot zone by alumina rods. Heating and cooling rates were about 20° to 100°C./minute, but not noted or monitored with precision.

### III.B.1e. Sample preparation

Because the mechanical testing, Section IV and some sample characterization steps were simple, Section III.B.2, sample preparation was limited to cutting or breaking hot-pressed samples to a size useful for characterization and producing flat parallel surfaces. Some hot

---

\* Honeywell-Pyr-O-Vane, Minneapolis, Minn.

\*\* Leeds and Northrup - 8690.

+ HP-3465A.

pressed pieces were simply broken by hammers or pliers to produce smaller pieces. Later samples were cut into 5 to 7 mm squares with a diamond saw with the thickness of the sample given by that of the "parent" hot-pressed sample. Usually both sides perpendicular to the hot pressing direction would be ground to flat surfaces, but only one surface would be polished. Most flat surfaces were prepared by hand, using light grinding with a silicon carbide media with grits of 240, 320 and 600, and by polishing with 0.3 micron and 0.06 micron alumina. Water was used as a coolant and alumina slurry medium. Later samples were polished using diamond paste from 9 microns to 0.25 micron on a commercial automatic polisher. Kerosene was used as a cooling fluid for both the diamond saw and diamond polisher.

### III.B.2. Sample Characterization

In addition to mechanical  $K_{IC}$  testing, Section IV, some solid specimens and powders were characterized by SEM/EDAX, TEM, X-ray diffraction, high and low magnification optical microscopy, infra-red spectrometry, and BET. Some zirconia grain sizes were estimated from photographs obtained by SEM or TEM.

Fracture surfaces and polished surfaces were ultrasonically cleaned in methanol and coated with Au, Ag, or Pt for examination with SEM/EDAX. The particular metal coating used would often mask peaks of major elements and minor impurities of particular interest in the EDAX mode. Normal secondary electron and backscattered electron modes were used in SEM.

TEM<sup>\*</sup> specimens were made by slicing about 0.3 mm thick disks with

---

\* J.H. Schneibel did all TEM work



a diamond saw, grinding to about 0.1 mm using 20 micron silicon carbide powder, then polishing with 6, 3, 1 and 0.25 micron diamond paste on both sides. When the polished thickness reached about 50 microns, the samples were mounted on 3 mm diameter copper disks and ion-beam milled at 6 KV with argon ions until perforation occurred. Radiation damage on the sample surfaces and surface roughness were removed with 2 KV ions. The surface was coated with carbon and the samples were examined in a Philips Em 300. Most samples examined were 15<sup>m</sup>/o ZrO<sub>2</sub>-85<sup>m</sup>/o ThO<sub>2</sub>

X-ray analysis was performed on powders and dense samples with a commercial diffractometer\* using copper radiation. Infra-red absorption spectra were obtained using a fast Fourier transform spectrometer. I.R. measurement usually encompassed a circular region about 1/4 inch in diameter. Spectra with and without a sample in place were obtained and a transmittance curve derived from this. The surface area of several early powder samples were obtained via BET.\*\* Many different optical microscopes were used. Densities were measured by the Archimedes technique using toluene as the fluid, or estimated from microscopy.

### III. RESULTS - PROCESSING

#### III.C.1. Powder and Samples made from Hydroxide Precursors

##### III.C.1a. Powder

An oxide powder with a particle size of less than 150 Å and a surface area of greater than 30 m<sup>2</sup>/gr can be made from thorium-zirconium hydroxide. Precipitation speed and the concentration of the reactants significantly

---

\* G.E. and Diano

\*\* Work performed by Tom Coyle

alters the grain size of the alloy and zirconia distribution after the powder has been hot pressed. Hydroxide calcined without organic washing produces large hard agglomerates that make densification difficult. In contrast, hydroxides calcined after organic washing are large, soft agglomerates that are easily milled to smaller sizes and thus make densification to low porosity levels possible. The fluid medium the powder is milled in and the method of drying the fluid/powder slurry also alters the zirconia distribution in a hot pressed specimen. The results of some powder production and processing steps on zirconium distribution and agglomerate hardness are interpreted from the hot pressed specimen utilizing a particular powder. This is unfortunate because of the intervening densification step. The analytical machines (STEM with excellent resolution) necessary to determine chemical composition on the scale of the particle size of these powders ( $150 \text{ \AA}$ ) in an undensified powder mass are unavailable at present.

The "best" sample production method to which variations of powder processing will be compared is as follows (Figure III.2). Hydroxides were precipitated during rapid mixing, 75 ml/sec, of filtered concentrated nitrate solutions (about 0.9 molal) and undiluted ammonium hydroxide. The resulting hydroxide precipitate was thoroughly washed with acetone and toluene. As the toluene replaces the acetone, the gel becomes clear. Toluene is not allowed to fully evaporate at room temperature and the hydroxide gel is calcined at  $600^\circ\text{C}$  in air for two hours. The oxide is attrition milled for two hours in methanol or acetone and screened. After the organic fluid evaporates, the powder is hot pressed at about  $1600^\circ\text{C}$  (for 15 mole % zirconia) for one half hour. The zirconia grain size

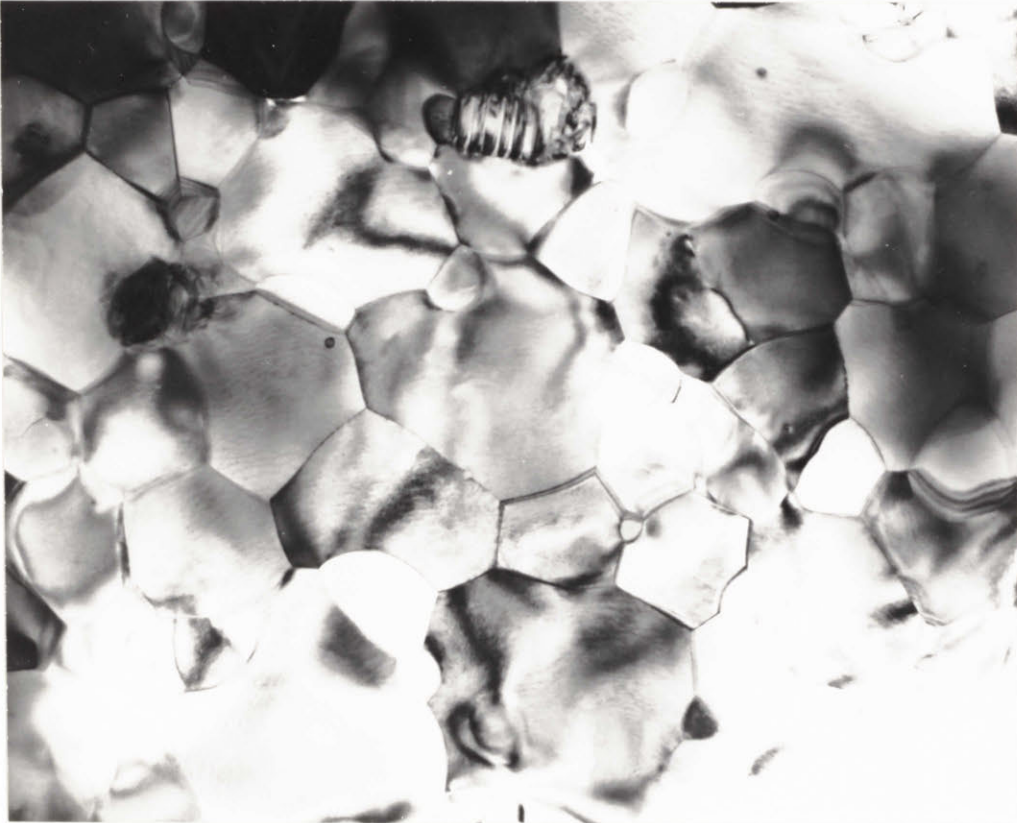
is fine and well distributed (Figures III. 3. and III. 4., samples H-85-I and H-85-Th1, respectively).

When reagent grade thorium and zirconyl nitrate were dissolved in water, often a metallic appearing material of about 1/2 mm length would accumulate on the magnetic stir bar. In addition, the zirconyl nitrate contained material that would not dissolve in about two hours at room temperature at the high concentrations of nitrate used. A filtering step through a 0.3 micron filter was introduced to eliminate these insoluble impurities.

Some hydroxide precipitations of thorium-zirconyl nitrate used a factor of two excess of ammonium hydroxide necessary for the formula  $\text{Th}(\text{OH})_4 - \text{Zr}(\text{OH})_4$  (Table I). The precipitation results in gel difficult to filter if only a small excess of ammonium hydroxide is used. Later samples used a large excess (1500%) of ammonium hydroxide and the gel was easier to filter. If, at this stage, the precipitate is calcined in air, a powder with extremely large (about 1 mm), hard, transparent agglomerates will be formed at temperatures between 450°C - 900°C. Two samples of similar processing histories (see Section III.C.1b and Tables I and II), except for washing the hydroxide with acetone and toluene in one case (H-54-B) and no washing (H-54-C), were hot pressed. H-54-B was 100% dense, H-54-C was porous, less than 95% dense.

Several powder batches were washed with combinations of water-acetone-toluene-acetone. The washed hydroxide was calcined at 600°C and powder evaluated by rubbing between gloved fingers. The acetone-toluene combination had large agglomerates but they were extremely soft and friable. The resulting crushed powder was extremely fine. Other combinations of

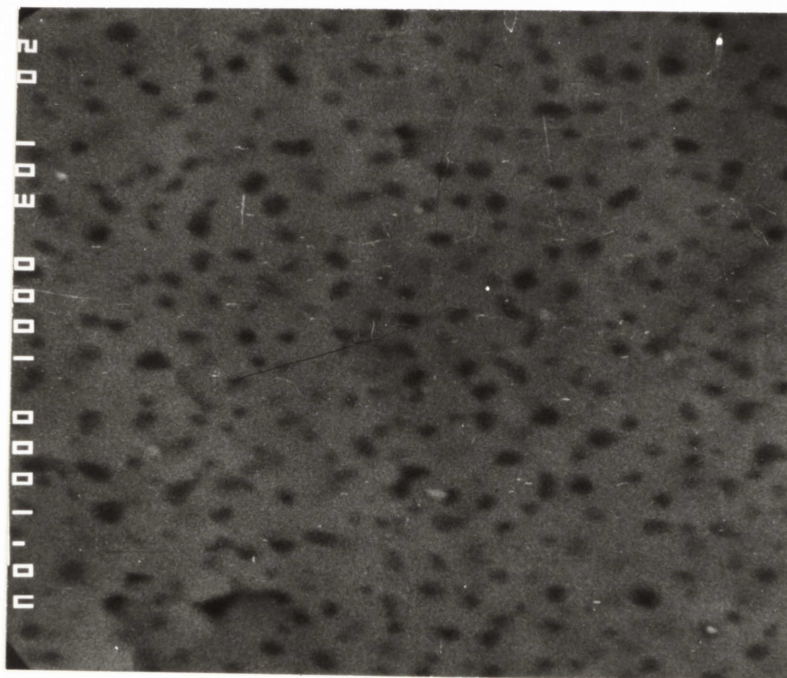




—  
0.3  $\mu\text{m}$

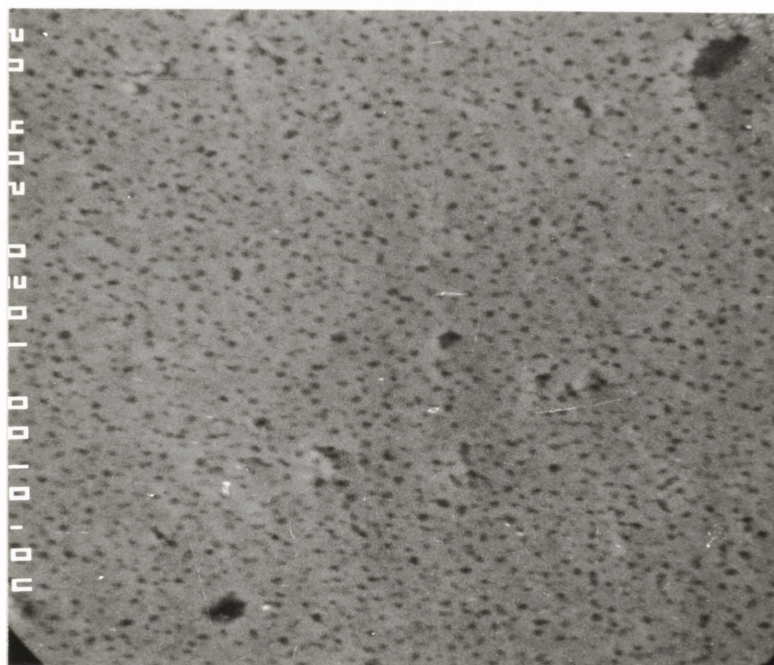
Figure III 3 Grain size of as hot pressed  $\text{ThO}_2$ -15 m/o  $\text{ZrO}_2$ , sample H-85-II. TEM foil and picture by J. Schneibel.

A.



1 μm

B.



3 μm

Figure III 4  $ZrO_2$  grain size, A, and  $ZrO_2$  grain size distribution, B, of as hot pressed  $ThO_2$ -15 m/o  $ZrO_2$ , sample H-85-Th1.

Table I

Sample Nomenclature

H	85	I	3
Powder precursor and densification Mode	Mole % ThO <sub>2</sub>	Parent Sample	Individual Sample #
O - oxalate/sintered			
OH- oxalate/hot pressed			
H - hydroxide/hot pressed			
HS- hydroxide/sintered			
HSF-hydroxide/sintered then pseudo isostatically hot pressed or hydroxide/prefire hot press with Pt wrap			



Table I

ThO<sub>2</sub>-ZrO<sub>2</sub> Produced from Hydroxide Precipitation

Sample	Mole % ZrO <sub>2</sub>	Powder processing <sup>#</sup>			Sample fabrication conditions*	Estimated density	Comments
		NH <sub>4</sub> OH <sup>+</sup>	Wash	Calcine			
H-100-A1	0	15x	Acetone/ Toluene	Vacuum 600°C 2 hr.	HP-1410°C/0.5 hr.	~90%	
H-100-B1	0	2x	H <sub>2</sub> O/Ac. tol./ Ac.	Vacuum 600°C 2 hr.	HP-1560°C/0.5 hr.	~90%	
H-100-C1	0	2x	H <sub>2</sub> O/Ac. tol./Ac.	Vacuum 600°C 2 hr.	HP-1500°C/0.5 hr.	~90%	
H-100-E	0	15x	Ac./tol.	Air 600°C 2 hr.	HP-1600°C.4hr. 34 MPa	~98%	No pressing pressure until 1350°C then 34 MPa hot tears. Large height/dia- meter ratio 2-3
H-100-F	0	15x	Ac./tol.	Air 600°C 2 hr.	HP-1600°C/0.5 hr. 34 MPa	~98%	3.4 MPa applied from room temp. to 1600°C then 34 MPa. Large height/diameter ratio 2-3. Hot tears
H-95-A1	5	2x	H <sub>2</sub> O/Ac./ tol./Ac.	Vacuum 600°C 2 hr.	HP-1450°C/0.5 hr.	~90%	

<sup>+</sup>Factor of NH<sub>4</sub>OH in excess of that needed for stoichiometric precipitation

<sup>#</sup>all 0.6 molal nitrate solutions except H-85-G, H-85-F

<sup>§</sup>0.3 molal nitrate solution

\* all hot pressings at 55 MPa except as noted; HP-hot pressed, An-annealed

TABLE I

Sample	Mole % ZrO <sub>2</sub>	NH <sub>4</sub> OH	Wash	Calcine	Samples fabrication Conditions*	Estimated density	Comments
H-90-A1	10	2X	Unknown	Vacuum 500°C 2hr	HP-1400°C/1 hr An-1100°C 29hr. Air	~99	Fractured during annealing
H-90-B1	10	2X	Ac/tol	Vacuum 500°C 2hr	HP-1325°C/1 hr An-1100°C 20hr Air	~90	Did not fracture during annealing
H-90-C1	10	2X	Ac/tol	Air 500°C 2 hr	HP-1500°C/1 hr An-1100°C 20hr Air	-	Fractured during annealing
H-85-A1	15	2X	unknown	Vacuum	HP-1600°C/1 hr An-900°C 20hr Air	~99	Surface layer oxidized and spalled, inner layer still reduced with few Lange cracks
H-85-F <sup>z</sup>	15	15X but diluted 50%	Ac/tol	Air 600°C 2 hr	HP-1585°C/0.5 hr 34 MPa	93 <sup>@</sup>	Milled in 1.5 ph H <sub>2</sub> O. Extremely nonuniform ZrO <sub>2</sub> distribution
H-85-G <sup>#</sup>	15	15X but diluted 50%	Ac/tol	Air 600°C 2 hr	HP-1630°C/0.3 hr 34MPa	93 <sup>@</sup>	Wide ZrO <sub>2</sub> grain size distribution
H-80-A1	20	15X	Ac/tol	Air 450°C 2 hr	HP-1300°C/0.5hr + 1500°C/ 5 min An-1150°C 15hr Air	~95	Outgassing as temp. raised from 1300°C
H-54-C	46	15X	none	Air 600°C 2 h4	HP-1425°C/0.5 hr 34 MPa	~95	Hydroxide intentionally not washed with organics

@ measured; # 0.3 molal nitrate solution; z 0.45 molal nitrate solution

TABLE II

ThO<sub>2</sub>-ZrO<sub>2</sub> Samples from Hydroxides Standard Processing

<u>Sample</u>	<u>Mole % ZrO<sub>2</sub></u>	<u>Fabrication Conditions*</u>	<u>Sample</u>	<u>Mole % ZrO<sub>2</sub></u>	<u>Fabrication Conditions*</u>
H-100 D <sup>@</sup>	0	HP-1580°C/0.5 hr/55 MPa	H-85-I	15	HP-1620°C/0.3 hr/55 MPa
H-97-Th	3	HP-1620°C/0.5 hr/34 MPa	H-85-J	15	HP-1550°C/0.5 hr/34 MPa
H-95-B <sup>@</sup>	5	HP-1560°C/0.5 hr/55 MPa	H-85-K	15	HP-1550°C.9.5 hr/34 MPa
H-90-D <sup>@</sup>	10	HP-1580°C/0.5 hr/55 MPa	H-85-L	15	HP-~1530°C/0.5 hr/34 MPa
H-90-Th	10	HP-1540°C/9.5 hr/55 MPa	H-85-Th	15	HP-~1600°C/0.5 hr/55 MPa
H-85-B <sup>@</sup>	15	HP-1580°C/0.5 hr/55 MPa	H-80-B <sup>@</sup>	20	HP-1560°C/0.5 hr/55 MPa
H-85-C <sup>@</sup>	15	HP-1700°C/0.5 hr/55 MPa	H-80-C <sup>+/#</sup>	20	HP-1625°C/1 hr/34 MPa An-1600°C/13 hr Ar. + CO
H-85-D1 <sup>+</sup>	15	HP-1650°C/3 hr/34 MPa An-1500°C/4 hr Vac/C	H-80-Th	20	HP-1465°C/0.5 hr/55 MPa
H-85-E <sup>+/#</sup>	15	HP-1580°C/0.5 hr/34 MPa HP-1600°C/8 hr	H-75-Th	25	HP-1445°C/0.5 hr/55 MPa
H-85-H	15	HP-1500°C/1.0 hr/34 MPa	H-70-A	30	HP-1500°C/0.5 hr/55 MPa
			H-70-Th	30	HP-1430°C/0.5 hr/55 MPa
			H-54-A	46	HP-1525°C/0.5 hr/34 MPa
			H-54-B	46	HP-1425°C/0.5 hr/34 MPa
			H-54-C <sup>xx</sup>	46	HP-1425°C/0.5 hr/34 MPa

<sup>@</sup> Calcined at 600°C under slight vacuum

<sup>+</sup> Calcined at 750°C; precipitated from solutions of half normal concentrations

\*HP-hot pressed; An-annealed

#Fractured after heat treatment

xxProcessing very similar to H-54-B except no acetone-toluene wash of hydroxide



washing gave powders with harder agglomerates; some agglomerates could not be broken by hand and cut the rubber gloves.

Washed hydroxide, with some toluene remaining in the gel, was calcined in a silica tube furnace attached to a mechanical vacuum pump. At about 150°C in the hot zone, ammonia precipitated on the cool end of the tube. At about 300°C, water began precipitating at the cool end. Evidently, any organic liquid evaporated before the ammonia came off. As the temperature rose from room temperature to between 450°C and 900°C, the gel continuously collapsed, ending at about one-half to one-third the original volume. Under vacuum, the powder was light brown, but if air was allowed in at high temperature, the oxide became white. Normally, after calcining in air, the oxides would be white to whitish yellow; the yellow tinge increasing with the zirconia content.

Powder made from acetone-toluene washed hydroxides calcined at 600°C to 750°C had a BET surface area of 30 to 60 m<sup>2</sup>/gram. TEM photographs show a particle size of less than 150 Å (Figure III.5). The individual particles are agglomerated on a 0.1 micron scale and these agglomerates form larger structures of greater than 2 microns, (Figure III.6). There are powder agglomerates of sizes greater than 50 microns before milling and screening.

X-ray diffraction of any powder revealed only three broad peaks centered on the main peaks for thoria. Evidently this is due to particle size broadening as the contrast in the TEM made the individual particles appear crystalline. There did not appear to be any major influence of calcining temperature between 600°C and 750°C, or atmosphere of air vs. a poor vacuum on powder samples (Table I).



Figure III 5 Particle size of powder made from hydroxide gel. TEM picture by J. Schneibel.

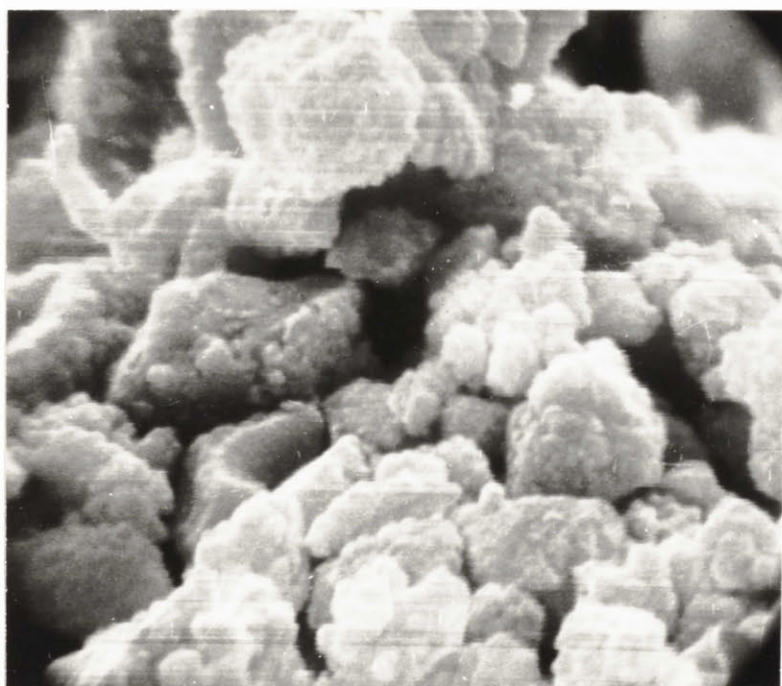


Figure III 6 Agglomerate structure of powder made from hydroxide gel.

As the speed of the precipitation is slowed from 75 ml/sec to 37 ml/hr, and the concentration of the nitrate in aqueous solution lowered from about 0.8 molal to about 0.27 molal, the average zirconia grain size is larger and the grain size distribution is wide (H-85-G, Figure III.7). Samples with similar composition, calcining and hot pressing conditions but higher concentrations of nitrates in solution (Figure III.4) had smaller grain sizes and narrower distributions. H-85-G also contained some porosity, probably as a result of the wider grain size distribution. Grain sizes larger than expected for the hot pressing conditions were seen in other samples (H-80-C, H-85-D, H-85-E). This was attributed to precipitation conditions.

When using acetone during milling, the oxide powder would often change color from white to light brown, indicating some chemical reaction might have been occurring. During vibratory milling the larger agglomerates tended to settle on the bottom of the milling jar and remained unmilled. The attrition milling did not have this problem as the stir bar and milling media created extremely turbulent conditions in the milling jar.

After milling and filtering, the organic fluid would evaporate from the powder in shallow aluminum foil pans over 20 hours. The powder settled during this evaporation and left a powder compact resembling "dried mud". Only in later samples, after H-85-F, was there much effort to crush this structure before hot pressing as it was soft and the researcher thought that it would crush under the action of the hot pressing pressure. In at least two cases, H-85-F and H-85-Th, the researcher was mistaken.

The powder for one sample, H-85-F, was milled for two hours in water



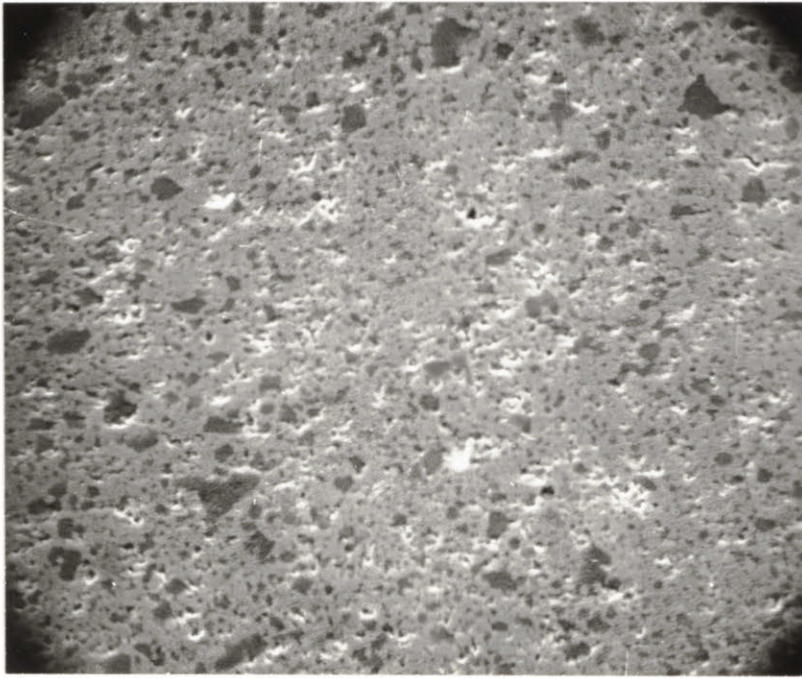


Figure III 7 Example of large  $ZrO_2$  grain size and wide  $ZrO_2$  grain size distribution in as hot pressed  $ThO_2$ -15 m/o  $ZrO_2$ . This microstructure was obtained by a slow hydroxide precipitation, low concentration of nitrate salts (0.27 molal) and diluted  $NH_4OH$ , sample H-85-G.

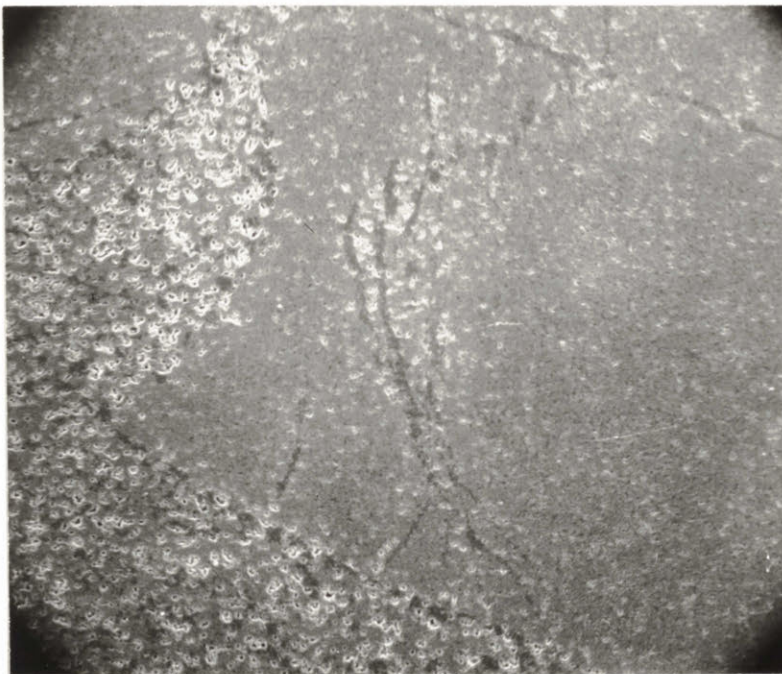


Figure III 8 Extremely non-uniform  $ZrO_2$  distribution in as hot pressed  $ThO_2$ -15 m/o  $ZrO_2$ . Distribution was a result of oxide flocculation by acetone dilution of an aqueous suspension of oxides and drying the acetone and residual water from the oxides.

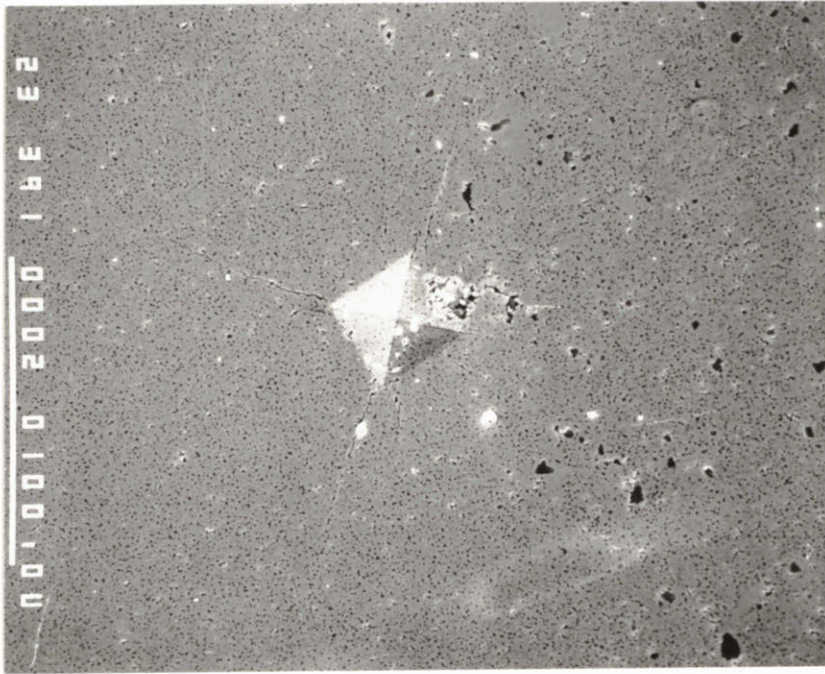
with the pH adjusted to between 1.5 and 2 with HCl. The powder was then filtered through 48 micron and 15 micron screens. The milled powder did not pass through the 15 micron filter easily. A large amount (250 ml) of pH adjusted water was used to wash the powder (about 20 grams) through the filter. The resulting dispersion was allowed to stand over 2 days in a sealed container and no significant settling occurred. The dispersion was repeatedly diluted with acetone to promote flocculation, and the fluid allowed to evaporate. No significant efforts were made to break the resulting "dried mud" structure. The resulting zirconia distribution in the hot pressed piece is shown in Figure III.8. This sample has extremely nonuniform zirconia and porosity distributions. Outlines of the "dried mud" structure can be seen. The unusual aspect of this is that both H-85-G and H-85-F have not spontaneously fractured after 1.5 years. Evidently methonal also can produce a nonuniform zirconia distribution as H-85-Th had several areas where this "dried mud" structure could be seen in Fig. III. 9.

The 48 micron filtering step was introduced after the sample H-85-E fractured after hot pressing because debris from the grinding media were hot pressed into the sample along with the powder.

Although not central to the main theme, two observations were interesting. When a powder that had just been calcined but was at room temperature was sprayed with acetone prior to milling often the acetone would ignite. When this happened, the temperature would often reach high enough for the powder to glow red (about 700°C to 800°C). If the powder did spontaneously ignite the acetone, then the powder after milling was brown. When methanol was used it did not ignite and the powder remained white.



A.



25µm

B.



100µm

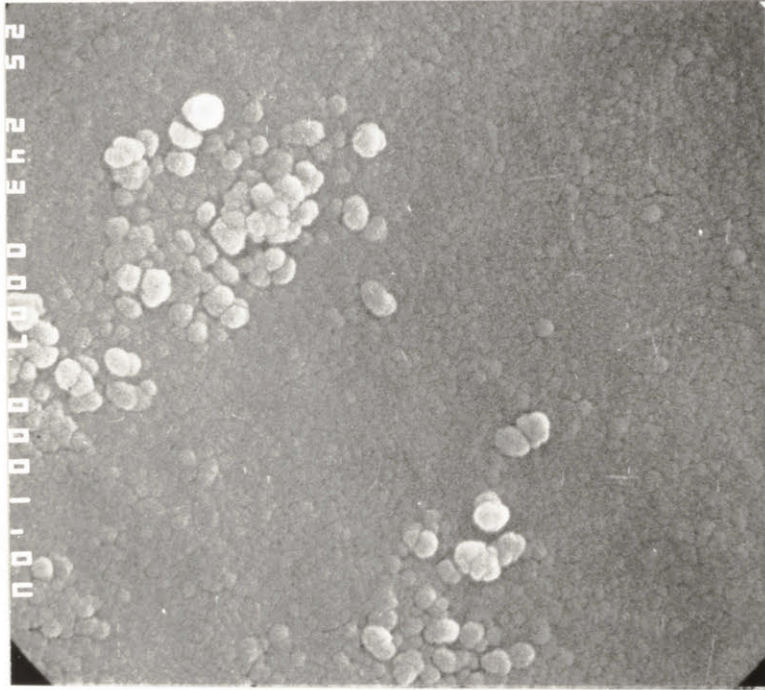
Figure III 9 Non-uniform  $ZrO_2$  grain size distribution. Milled oxide powder dried from methanol. Annealed 10 hours,  $1600^{\circ}C$ , CO atmosphere, sample H-85-Th 40.



One method to produce a high density green ceramic body is slip casting. A methanol slip of milled oxide with a low solids density was placed in the millipore filter apparatus and a filtration casting was attempted. The resulting green body was opaque on the bottom, but a surface layer of about 3 mm deep was translucent to transparent. The top surface was very shiny and extremely good powder packing can be seen in an SEM micrograph (Figure III.10). No information regarding the zirconia phase distribution was obtained, however. This green body was not carefully dried; drying cracks appeared at approximately every 150 microns after a week at room temperature and uncontrolled humidity.

#### III.C.1b. Samples made from Hydroxide Precursors

For thoria + 5 mole % - 46 mole % zirconia, by hot pressing oxide powders made from coprecipitated hydroxides, dense (greater than 99%) two phase samples can be obtained which have a submicron grain size and an average zirconia grain size of 0.3 micron or less. Sintering can also produce submicron grain sizes, but densities were lower (about 95%). Annealing hot pressed materials at high temperatures (greater than 1300°C) to increase the zirconia grain size must be done in a reducing atmosphere to prevent bloating. If a hot pressed material must be oxidized to increase I.R. transmission, the temperature must be low enough to prevent bloating, but high enough to avoid spontaneous fracture. If the grain size is too small and the material heavily contaminated with carbon, then the material will still bloat at 1200°C. At zirconia sizes under one micron, there is significant I.R. transmission for some 15 mole % zirconia materials.



0.3 μm

Figure III 10 Surface of a slip cast/settled green body. Extremely good powder packing and small average pore size resulted in a 3 mm deep transparent to translucent surface layer before any densification.

### III.C.1c. Hot Pressing

There were three major problems associated with hot pressing fine particle size powders to produce thoria-zirconia alloys. If the powder is incompletely calcined, or if the powder has been exposed to the room atmosphere for a period greater than a few days before hot pressing, extensive outgassing occurs as the temperature is raised (H-80-A, H-85-A, Table I). Even though thoria is the oxide with the highest melting point, densification of fine particle size powders can occur between 800°C and 1000°C. If a high pressure is not maintained on the hot press ram, then shrinkage by sintering occurs in the sample before hot pressing begins. The low partial pressure of oxygen and the high carbon activity in the graphite hot pressing die at temperature can lead to incorporation of carbon in the oxide specimen as well as making the specimen oxygen deficient in stoichiometry. This carbon incorporation from the hot pressing die is in addition to any carbon which might have remained as a residue from milling the oxide powder in an organic fluid (all hot pressed specimens were affected by this problem).

The outgassing problem can be solved by increasing the calcining temperature and when hot pressing raising the temperature slowly and not applying the pressing pressure until the maximum temperature is reached. Unfortunately, both these steps can lead to larger grain sizes in the dense specimen. Not applying the pressing pressure until the maximum temperature is reached leads to the powder shrinking away from the die wall. This is due in part to the low density, 20 to 40%, of the green sample. When the pressure is applied at a high temperature, 1400°C to 1600°C, the sample often fractures because the sides are unconstrained



(H-100-E, H-100-F, H-80-B, Tables I and II). The compromise reached between these conflicting goals was to calcine the powder at 600°C to 750°C, outgas the powder up to 800°C, and then apply the pressing pressure that was held continuously until the pressing was complete.

Hot pressing runs are compiled in Tables I and II. Table I contains the early samples where most variations in powder processing were tried. Table II contains samples that have more consistent processing variables.

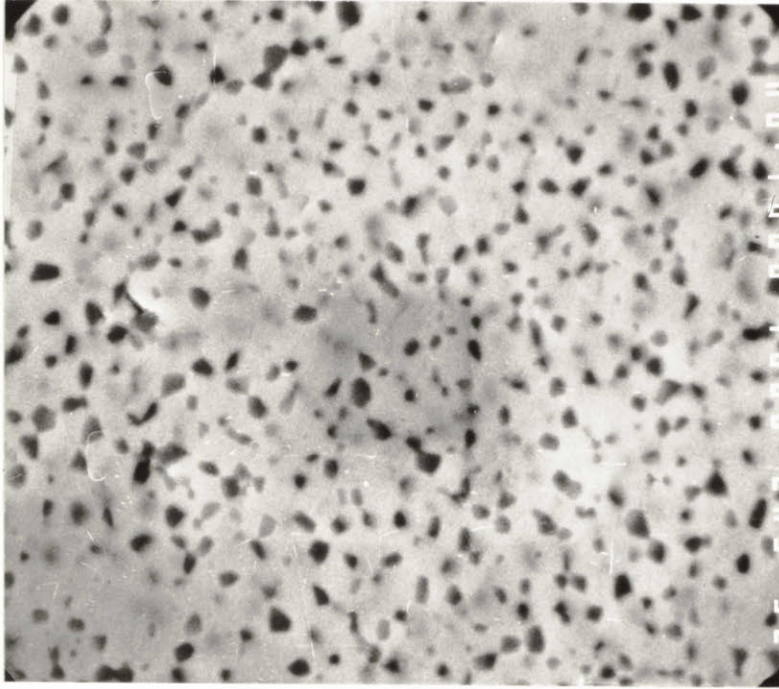
The powder processing/hot pressing conditions in Table I are too scattered to determine whether the low densities of most samples on Table I are due to hot pressing temperature, the type of washing the hydroxide received or annealing in air. Since H-90-A and H-85-A had high densities, the amount of excess ammonium hydroxide seems to be unimportant in achieving high density. During calcining the atmosphere and temperature (between 600°C and 750°C) seem to have no major effect on densification. Calcining temperatures lower than 600°C lead to some outgassing problems (H-80-A). The samples on Table I were not characterized for grain size or zirconia distribution.

As the zirconia content went up, the hot pressing temperature needed to maintain a zirconia grain size below 0.3 microns dropped from about 1600°C for 15 mole % zirconia to 1425°C for 46 mole % zirconia.

The densities of the samples in Table II were judged to be 99 to 100% of theoretical by microscopy. Very few triple points have detectible pores in TEM. No pores were found in SEM and observations via optical microscopy suggest that most residual porosity is isolated and associated with original interagglomerate pores or packing inhomogeneities.

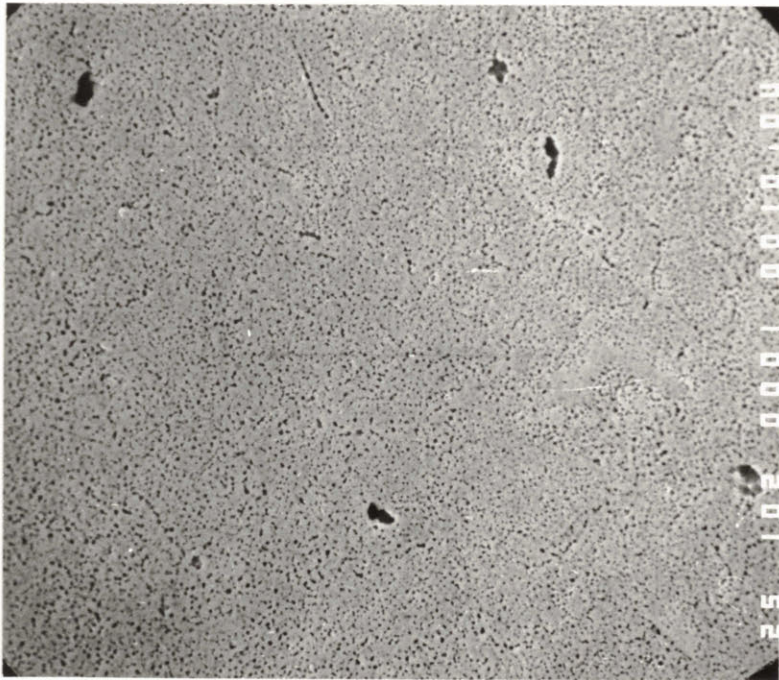
Most of the zirconia grains in these samples were well distributed and similar in size as can be seen in Figures III.4 and III.11. The fine

A.



2  $\mu\text{m}$

B.



10  $\mu\text{m}$

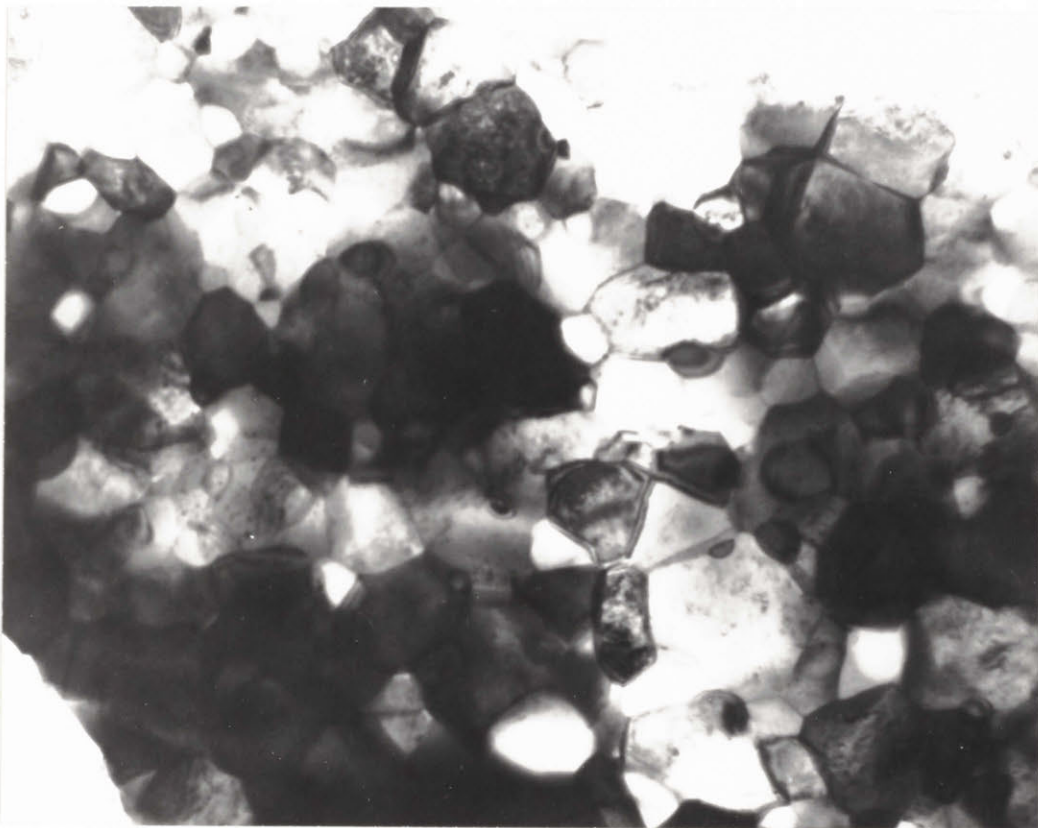
Figure III 11  $\text{ZrO}_2$  grain size and grain size distribution in  $\text{ThO}_2$ -15 m/o  $\text{ZrO}_2$  annealed at  $1600^\circ\text{C}$  for 19 hrs. in a reducing atmosphere. Sample H-85-H9.



grain size in as-pressed samples can be seen in Figures III.3 and III.12. The scarcity of twins or faults in the TEM foil suggests there is little if any monoclinic zirconia in the bulk for as-hot-pressed 15 mole % zirconia. Electron diffraction in the TEM confirms this. X-ray diffraction shows a mixture of tetragonal and monoclinic zirconia in addition to the cubic thoria for a carefully polished surface of as-pressed 15 mole % zirconia with a 0.1-0.3 micron zirconia grain size. The zirconia grains are between the thoria grains, not entrapped within them, and the zirconia grain size is typically somewhat smaller by a factor of 2 to 3 than the thoria grain size. Annealing appears to increase both the zirconia and thoria grain sizes without significantly changing the relative morphology of the microstructures.

The major deficiency in the microstructures is the presence of occasional zirconia grain patches as large as 5 to 10 microns in size. Frequent occurrence of large patches of zirconia may cause flaws from microcracking, leading to low strength or even spontaneous fracture. It was thought that the undissolved material from the zirconyl nitrate solution might be large particles of zirconia or undissolved zirconyl nitrate that would lead to large zirconia patches in the hot pressed piece. To attempt to eliminate the undissolved matter, the zirconyl nitrate solution was filtered through a 0.2 micron filter in samples H-85-J, H-85-K, H-85-L before hydroxide precipitation. In samples as noted in Table II, both nitrate solutions were filtered through a 0.3 micron filter before hydroxide precipitation. Filtering the nitrate solution may reduce the size and number of isolated large zirconia particles. However, the hydroxide precipitation speed and reactant concentrations and how the





—  
0.3  $\mu\text{m}$

Figure III 12 Grain size in as hot pressed  $\text{ThO}_2$ -15 m/o  $\text{ZrO}_2$ , sample H-85-H1. TEM foil and picture by J. Schneibel.

oxide is milled and milling fluid evaporate seem to be the major factors controlling the zirconia spatial variability.

### III.C.1d. Other Densification Schemes

Because of the problem of carbon contamination and oxygen deficiency of the oxide alloy during hot pressing and bloating of the material during reoxidation (see next section), several other methods of attaining a high density were tried: sintering, sintering and pseudo-isostatic hot pressing and hot pressing with a platinum barrier between the sample and die. Samples produced by these methods are listed in Table III

The powder for an initial (unlisted) sintered specimen was calcined at 600°C and prefired in air at 650°C for two hours after the green body was formed. After about 12 hours at room temperature, this sample spontaneously fractured even though the sample was only 40% dense. The fractures were of sufficient energy to toss about 3 mm diameter pieces over 30 cm away from the main sample. Evidently, the calcining at 600°C and prefiring at 650°C left a sufficient amount of metastable tetragonal zirconia that transformed, upon cooling to room temperature, to shatter the porous body.

Powder for subsequent samples was calcined at 800°C in an effort to have a majority of monoclinic zirconia. Sintering at 1500°C - 1600°C gave zirconia grain sizes under 0.5 micron. Increasing temperature and time gave increased density and liquid nitrogen dried, high purity hydrogen atmosphere seems to give a higher density than does oxygen. The section of surface that was originally the surface of the pressed pellet was dense on sample HS-85-A6 but the interior was somewhat porous with the pores being 2 to 8 microns in diameter and spaced every 10 to 20 microns

TABLE III  
 ThO<sub>2</sub>-ZrO<sub>2</sub> Samples, Sintered

Sample	Mole % ZrO <sub>2</sub>	Prefire	Fabrication Conditions*	Density %	Comments
HS-85-A1 <sup>Ⓐ</sup>	15	800°C/1 h/O <sub>2</sub>	S-1500°C/2.5 hr/O <sub>2</sub>	93.5 <sup>+</sup>	White
HS-85-A2 <sup>Ⓐ</sup>	15	800°C/1 h/O <sub>2</sub>	S-1600°C/2.5 hr/O <sub>2</sub>	95.0 <sup>+</sup>	White
HS-85A5 <sup>Ⓐ</sup>	15	800°C/1 h/O <sub>2</sub>	S-1600°C/2.5 hr/H <sub>2</sub>	97.5 <sup>+</sup>	Black
HS-85-A6 <sup>Ⓐ</sup>	15	800°C/1 h/O <sub>2</sub>	S-1600°C/0.5 hr/H <sub>2</sub>	94.5 <sup>+</sup>	Surface Black Interior Grey
HSF-85-A3 <sup>Ⓐ</sup>	15	HS-85-A1	PIP-1630°C/0.3 hr/34 MPa	98.4 <sup>+</sup>	Light grey near
HSF-85-A4 <sup>Ⓐ</sup>	15	HS-85-A2	PIP-1610°C/2hr/34 MPa	99 <sup>+</sup>	surfaces
HSF-85-A8 <sup>Ⓐ</sup>	15	HS-85-A5	PIP-1600°C/2hr/34 MPa	99 <sup>#</sup>	Extensively cracked
HSF-85-A9 <sup>R</sup>	15	HS-85-A8	An-~1200°C/0.5hr/O <sub>2</sub>	99 <sup>#</sup>	Translucent in uncracked portions
HSF-85-B	15	900°C.2hr/Air	HP-1600°C0.5hr/34 MPa**	95 <sup>#</sup>	Grey
HSF-85-C	15	900°C.2hr/Air 1000°C/2hr/H <sub>2</sub>	HP-1600°C/0.5hr/34 MPa**	98.5 <sup>+</sup>	Black as HP'ed Translucent after 1200°C/2hr/O <sub>2</sub> anneal

<sup>Ⓐ</sup> Calcined at 800°C

\* HP-hot pressed; S-sintered; PIP-pseudo-isostatically pressed, i.e., wrapped in Pt foil and embedded in C powder; An-annealed.

\*\* Wrapped in Pt foil.

<sup>+</sup> Measured.

<sup>#</sup> Estimated.

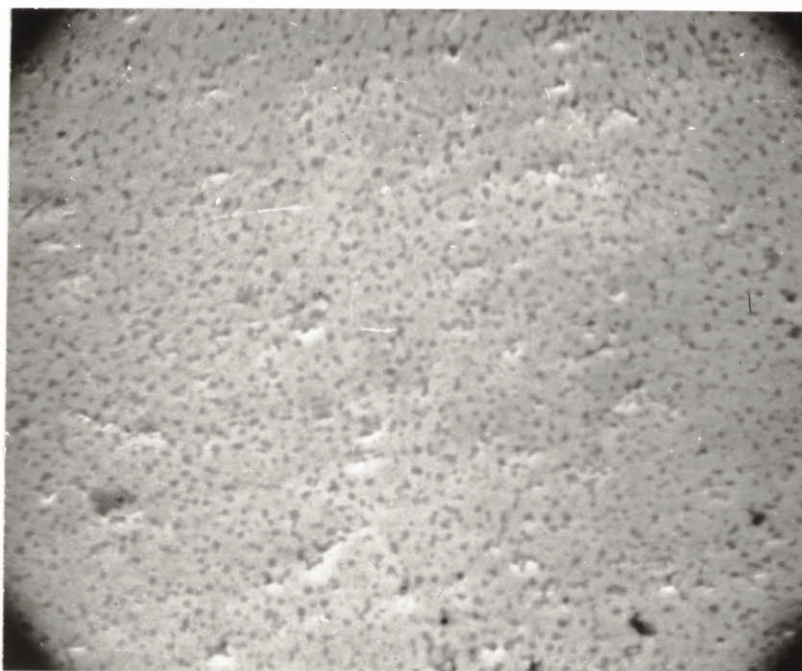


(Figures III.13a and III.13b). The effect of increasing time from 0.5 hours to 2.5 hours at 1600°C was the gradual elimination of these pores (Figures III.14a and III.14b). Evidently the large pores are from poor packing of large agglomerates, the isostatic pressing of the green body crushes the agglomerates filling the pores near the exterior of the sample but not in the interior.

An effort was made to increase the density of three samples by hot pressing/forging the sintered pieces. As the porosity in the sintered specimens was closed, isostatic hot pressing would be an attractive means of increasing the density. An isostatic hot press was not available. Pseudo-isostatic hot pressing was tried instead. The platinum surrounding each sample kept carbon contamination to a minimum. The densities did increase and the least porous sample, H-85-A8, was oxidized afterwards. The grain size remained under 1 micron (Figure III.15). This sample was heavily fractured; Edax indicated a large excess of zirconia on the fracture surfaces. The oxidation did not increase the cracking and several small (about 3 mm diameter) pieces were translucent after oxidation.

Two hot pressing runs were made where the powder was wrapped in platinum foil. The green pellet of HSF-85-B was pre-fired in air at 900°C to eliminate organic residues left from milling the powder. The density was low and thoria grain size was about 2 microns after hot pressing. When two pre-fired treatments were made, the air firing to eliminate organic residue and the  $H_2$  to reduce the oxygen activity during hot pressing, a higher density was achieved. One difficulty encountered with the platinum wrapping was folding or extrusion of the platinum into the sample. This was especially severe in HSF-85-B and HSF-85-C since the initial density was about 40%, hence there was about a factor of 2 too much

A.



5 μm

B.

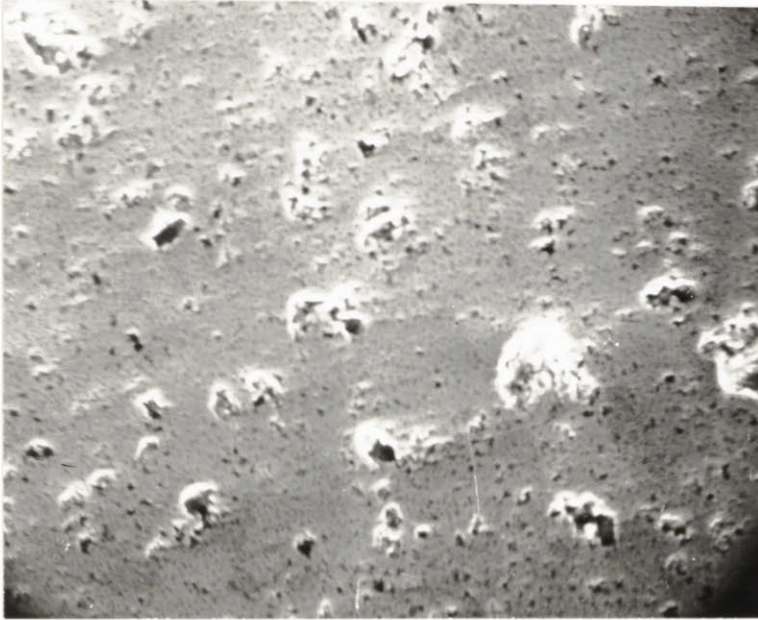


5 μm

Figure III 13 ThO<sub>2</sub>-15 m/o ZrO<sub>2</sub> sintered at 1600°C, 1/2 hr., in dried high purity H<sub>2</sub>. Dense surface, A and porous interior B. Porosity in interior from agglomerates uncrushed by room temperature isostatic pressing. Sample HS-85-A6.

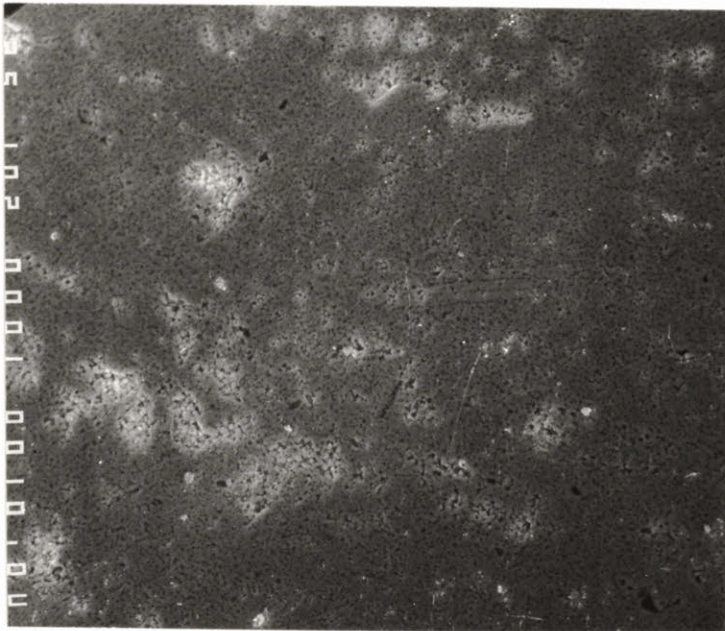


A.



10  $\mu\text{m}$

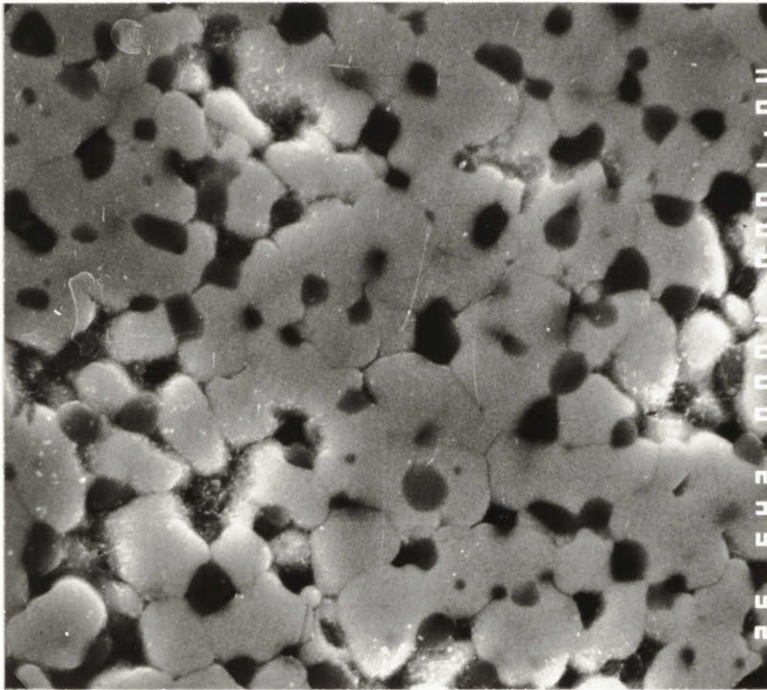
B.



10  $\mu\text{m}$

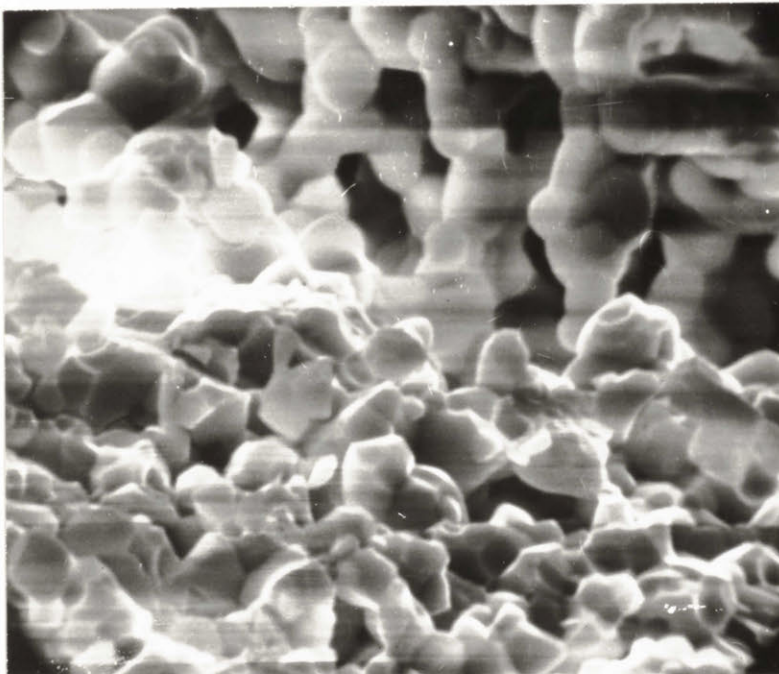
Figure III 14 Large interglomerate pores are gradually eliminated by increasing sintering time at 1600°C, A. 1/2 hr., sample HS-85-A6, B. 2-1/2 hrs., sample HS-85-A5.





2  $\mu\text{m}$

Figure III 15 Grain size of sintered, pseudo isostatically hot pressed then oxidized  $\text{ThO}_2$ -15 m/o  $\text{ZrO}_2$ . Sample HSF-85-A9.



1  $\mu\text{m}$

Figure III 16 Fracture surface of extremely bloated  $\text{ThO}_2$ -20 m/o  $\text{ZrO}_2$ . Sample was oxidized for 4 hrs. in air at  $1600^\circ\text{C}$  after hot pressing. Before oxidation density was greater than 99%. Sample H-80-B10.

platinum for the area of the sides of the samples and this was folded into the samples during densification.

### III.C.1e. Annealing

The main scientific objective of this study was to develop  $K_{IC}$  vs zirconia grain size curves for different volume fractions. The main engineering objective was to develop a method for reliably producing high toughness I.R. windows (and toughness seemed to be a function of zirconia grain size). The quickest way to produce dense samples of varying grain size was to hot press a fine 0.1 to 0.2 zirconia grain size material and anneal at high temperature allowing the grains to grow to desired sizes. In addition, if nonstoichiometry caused by hot pressing or sintering caused absorption in I.R. frequencies, then the samples would need to be oxidized at high temperature to meet the engineering objective.

Samples sintered in  $H_2$  or hot pressed in graphite are black, indicating one or both of the  $ZrO_2$  or  $ThO_2$  has become oxygen deficient. For both sintering and hot pressing, higher densities were obtained with reduced material. Thus, to obtain ultra-fine-grained, dense material, it is desirable to sinter in a reducing atmosphere. Further, annealing for grain growth, or oxidation seems to be affected by residual carbon. Thus, it is useful to summarize the observations from over five hundred annealing experiments.

Oxidation of hot pressed materials to translucency requires annealing times of a few hours at  $1200^\circ C$  and five to ten times longer at  $1000^\circ C$ . Appreciably shorter times are required to oxidize material which has been  $H_2$  sintered or presintered and hot pressed in a Pt wrap. Assuming oxidation is diffusion controlled, a few experiments indicate that at  $1200^\circ C$



the annealing time for hot pressed material is  $t \sim 3 \times 10^6 x^2 - \text{s/cm}^2$  (where  $x$  is the sample half thickness) and  $\text{H}_2$  sintered materials  $t \sim 1 \times 10^6 x^2 - \text{s/cm}^2$ . Presumably, longer reoxidation times are required for hot pressed samples because both a change in stoichiometry and oxidation of entrapped carbon must occur. Generally, oxidation can occur at temperatures below those necessary for grain growth or sintering. For moderate grain growth and coarsening of  $\text{ZrO}_2$  particles to 1 micron or so,  $1600^\circ\text{C}$  is convenient for 15%  $\text{ZrO}_2$ , but it may be appreciably too high for higher  $\text{ZrO}_2$  contents. Thus, if fracture occurs below  $1200^\circ\text{C}$ , and it often did (see Table I), the effective temperatures range where oxidation can be accomplished without creep or grain growth is limited.

At higher temperatures ( $1500\text{--}1600^\circ\text{C}$ ), bloating during oxidation can cause the density to drop below 80% (Table IV); the pores are irregularly spaced and some are extremely large, Figure III.16. At lower temperatures, extremely fine pores ( $\sim 500 \text{ \AA}$ ) are found along grain boundaries after oxidation, Figure III.17. Apparently, these fine pores result when the temperature is too low for significant creep of the materials. Thus, after oxidation at  $1200^\circ\text{C}$  fine-grained (about 0.2 micron) materials have larger pores (H-85-I) whereas larger grained (about 1 micron) materials may only have very fine pores. As the zirconia content increases, the creep rate should increase, if grain size remains constant.

Several factors suggest that the bloating of hot pressed material is primarily caused by internal oxidation of carbon. Bloating at  $1600^\circ\text{C}$  has been observed in air,  $\text{N}_2$  and  $\text{H}_2$  and apparently occurs in any atmosphere except when the  $P_{\text{O}_2}$  is low enough to prevent oxidation of carbon. The lack of bloating under sufficiently reducing conditions also suggests



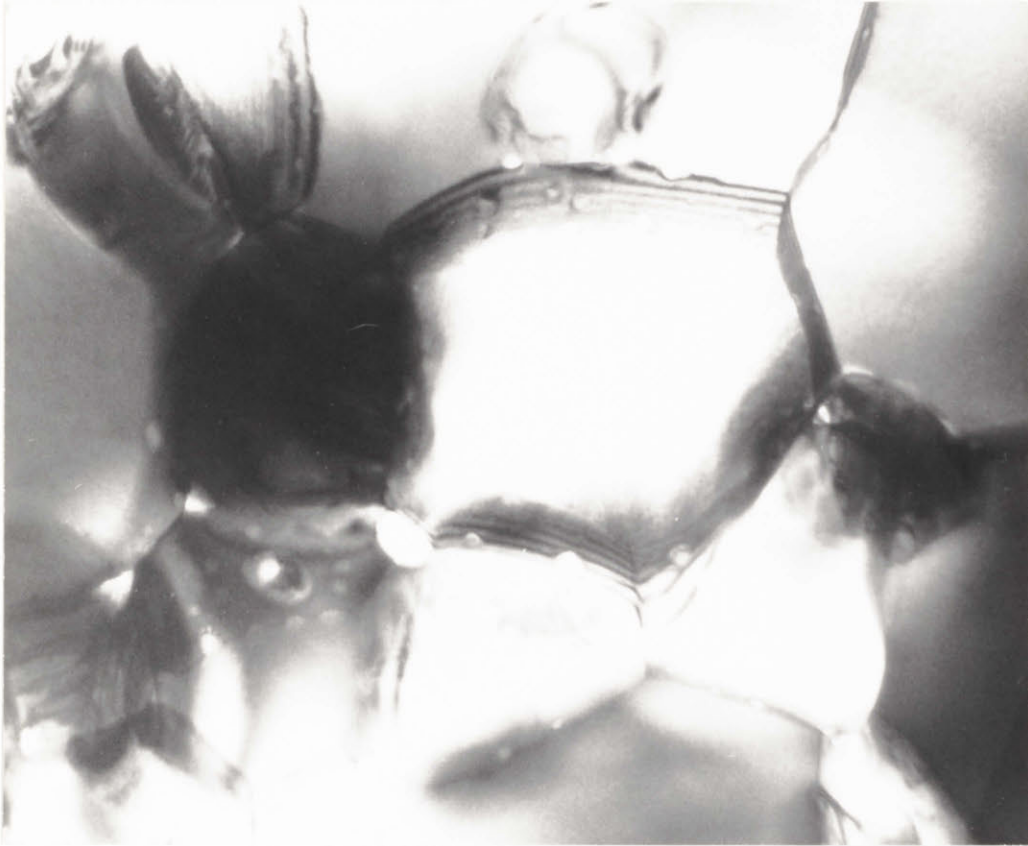
Table IV

Effect of Air Annealing Hot Pressed  $\text{ThO}_2\text{-ZrO}_2$ 

Sample	Mole % $\text{ThO}_2$	Anneal Condition <sup>+</sup>	Density	
			g/cc	% <sup>@</sup>
H-85-B	85	-	9.45	(99.7)
H-85-B2	85	1400C/1 hr.	9.30	(98.1)
H-85-B3	85	1400C/4 hr.	9.35	(98.6)
H-85-B4	85	1400C/16 hr.	9.15	(96.5)
H-85-B5	85	1500C/1 hr.	9.15	(96.5)
H-85-B6	85	1500C/1 hr.	8.55	(90.2)
H-85-B7	85	1500C/16 hr.	8.90	(93.9)
H-85-B8	85	1600C/16 hr.	7.00	(73.8)
H-85-B9	85	1600C/13 hr. in Ar + CO, + 1200C/2.5 hr.	9.36	(98.7)

<sup>+</sup>Annealings in Air Unless Noted.

<sup>@</sup>Theoretical Density Approximated Using 10.0 g/cc for the  $\text{ThO}_2$  and for  $\text{ZrO}_2$  the average of 5.56 g/cc and 6.10 g/cc for the monoclinic and tetragonal phases.



—  
0.2  $\mu\text{m}$

Figure III 17 Fine pores ( $\sim 500 \text{ \AA}$ ) along grain boundaries caused by oxidation at  $1200^\circ\text{C}$ . Sample H-85-D2. TEM foil and picture by J. Schneibel.

H<sub>2</sub>O or other residual gasses entrapped in the ceramic do not cause significant bloating. The presumption that the residual carbon is present in hot pressed material as a condensed phase or in solution, and that it is oxidized to CO<sub>2</sub> under an oxidizing anneal, is consistent with an IR absorption peak at 2350 cm<sup>-1</sup> which is evident in the IR spectra of oxidized material H-85-D2, H-85-B9, OH-95-A1, OH-95-A2. There were no absorption peaks in an as-pressed sample, H-70-A (see Figure A.A.2 in Appendix A).

The source of the entrapped carbon is unclear. It may come from the graphite dies. However, several observations suggest that an additional source of carbon may be residue from organic solvents. Sometimes acetone washed hydroxides are dark colored if calcined below 700°C. Also, powders milled in either acetone or methanol are sometimes darkened upon addition of the organic or after heating in the 200-600°C range. Darker areas in H-85-11 correlated with more intense bloating during oxidation of the as-pressed piece at 1230°C; in H-85-11 the residue from organic solvents was exceptionally heavy. Presumably the organic solvents was exceptionally heavy. Presumably the organic residue can be oxidized and removed during sintering or pre-firing in oxygen, perhaps even in H<sub>2</sub>, but remains during hot pressing in graphite.

Annealing thoria-zirconia alloys under extremely reducing conditions can cause difficulties also. At about 1630°C ZrC becomes stable with respect to ZrO<sub>2</sub> at a CO partial pressure of about 1 atmosphere (JANAF Thermodynamical Tables). ZrC was detected by X-ray diffraction on the surfaces of several samples. Hence, careful control of the annealing atmosphere is necessary for materials contaminated with carbon. An



annealing atmosphere of CO buffered with a carbon-zirconia mixture and temperatures below about 1630°C was adequate to prevent ZrC formation and minimize bloating during grain growth anneals.

When the temperature and atmosphere precautions were taken, then for 15 mole % zirconia specimens the zirconia grain size could be varied from as hot pressed (as small as 0.2 micron) to greater than one micron after about 60 hours at 1600°C. Longer times would be used for materials with less than 15 mole % zirconia and shorter times and lower temperatures for higher mole %. This was sufficient to cover the zirconia grain sizes of interest for  $K_{IC}$  measurement and spontaneous fracture behavior, Section IV.

### III.C.2. Results on Samples Produced from Oxalate Precursors

Densities of samples sintered with oxide powders derived from thorium oxalate and suspended  $ZrO_2$  are given in Table V. The  $ZrO_2$  phase in the bulk could not be identified from standard X-ray diffractometry using Cu radiation because of the  $ThO_2$  background radiation masked the  $ZrO_2$  peaks; a layer only about 10 microns deep yields diffraction information. Further, the solubility of  $ZrO_2$  in  $ThO_2$  is not known but is estimated to be 3%. Thus the theoretical density for each composition can also only be estimated. From these estimates of the theoretical densities the porosities in the sintered samples was 1 to 7% with higher values for the higher  $ZrO_2$  contents; metallographic and SEM examination was consistent with these estimates. Higher  $ZrO_2$  content led to lower densities. Optical and scanning electron microscopy (SEM) indicated the  $ThO_2$  grain sizes were typically 6 to 12 microns, with finer sizes in the samples with higher  $ZrO_2$  contents. Many  $ZrO_2$  particles were 0.5-2 microns, but some were as

Table V

ThO<sub>2</sub>-ZrO<sub>2</sub> Samples Produced from Oxalate Precipitation

Sample	Mole % ThO <sub>2</sub>	Sintering Conditions		Density *		Comments
				g/cc	%	
OS-80-A	80	1700°C	24 hr	8.65	(93.0)	
OS-85-A	85	1700°C	24 hr	9.10	(96.0)	
OS-90-A	90	1700°C	24 hr	9.39	(97.2)	Using unmilled
OS-95-A	95	1700°C	24 hr	9.56	(97.2)	ZrO <sub>2</sub>
OS-100-A	100	1700°C	24 hr	9.91	(99.1)	
OS-100-B	100	1700°C	24 hr	9.64	(96.4)	
OH-95-A	~99-95	H.P. 1525C/45 min/ 55 MPa		-	-	Attempted to co-
OH-95-A1	~99-95	+ An. 1000C/20 hr		9.90	-	precipitate oxalates Transparent

\* Theoretical Density Approximated Using 10.0 g/cc for the ThO<sub>2</sub> and for ZrO<sub>2</sub> the average of 5.56 g/cc and 6.10 g/cc for the monoclinic and tetragonal phases.

large as 10 microns.

Several powder batches were prepared by precipitating zirconyl and thorium oxalates from nitrate solution and calcining at 750-800°C. It was found that mixing zirconyl nitrate solution with a concentrated solution of oxalic acid gave a precipitate which soon redissolved. Thus it was concluded that the zirconium content in the oxalate "coprecipitated" samples was much less than expected from the Th:Zr ratio for the salts, and coprecipitation of oxalates was discontinued.

One hot-pressed sample was fabricated using this low ZrO<sub>2</sub> content powder, however (Table V). After hot pressing, this sample (OH-95-A) was black. This sample was transparent after oxidation at 1000°C for 20 hours in air (Appendix A, Figure A.2). A grain size of about 1 micron was measured during SEM examination and there was no evidence of a second phase. After 13 hours at 1600°C in a carbon tube furnace under flowing Ar followed by an oxidizing annealing at 1200°C for 2.5 hours, the sample was not transparent but weakly translucent (Appendix A, Figure A.A.2). After annealing at 2300°C in the carbon tube furnace, SEM examination showed the existence of a second phase. Whether the second phase was zirconia, zirconium carbide or thorium carbide was not determined.

#### III.D. Discussion, Powder Processing Sample Fabrication

The method previously described for producing fine grained ThO<sub>2</sub>-ZrO<sub>2</sub> samples from hydroxide precursors was adequate for most objectives of the study. Variations in processing can produce different grain sizes and grain size distributions. Gross control over the grain size distribution was achieved but minor variations still occurred. Segregation of zirconium/zirconia can occur at many stages during powder processing:



precipitation, washing with organic fluids, milling and settling from milling. Carbon contamination was not completely eliminated. Fabrication of useful samples for the engineering objective from oxalate precursors failed but the samples produced had microstructures appropriate for mechanical property study.

Fine particle size ( $150 \text{ \AA}$ ) thorium-zirconium oxide powder can be obtained by rapid mixing of concentrated aqueous nitrates and ammonium hydroxide. After hot pressing the grain sizes are larger and zirconia distribution is wider if lower concentrations and slower mixing is used. The precipitated gel is probably individual thorium hydroxide and zirconium hydroxide particles that calcine to the  $150 \text{ \AA}$  oxide particles. There are several possible combined effects on the precipitate gel when a slow dilute precipitation is used. The dilution reduces the supersaturation which can lower the nucleation rate leading to larger individual hydroxide particles. During precipitation the pH changes slowly and individual hydroxide particles may preferentially agglomerate with like hydroxides. The length of time used in the slow precipitation may allow segregation of the hydroxides independent of the range of pH change. Ostwald ripening may also take place during a slow precipitation. Some segregation agglomeration, or Ostwald ripening may also occur during washing with organic fluids.

With the exception of H-85-F, organic fluids were used during milling to promote agglomeration (soft) of unlike oxides while milling to reduce the size of the hard agglomerates from calcining. Reducing the hard agglomerate size too much was deemed undesirable as the scale of the zirconia distribution after calcining was unknown. The segregation of

zirconia for both H-85-F and H-85-Th 40 seems to have occurred at least during evaporation of the organic fluid immediately before hot pressing because the segregation appeared to be remnants of a "mud cake" structure. Carefully controlled pH changes in an aqueous suspension of thorium-zirconium oxides might result in the desired uniform zirconia distribution.

Drying and calcining of hydroxide gel or an oxide suspension from a polar fluid medium can produce large agglomerates. As the polar fluid dries the hydroxide/oxide particles rearrange themselves into local areas of dense packing. When the hydroxide is calcined these densely packed areas sinter at the calcining temperature because of the fine particle size, forming large dense agglomerates. Washing the hydroxide gel with acetone and toluene replaces the polar fluids, changing the solvents dielectric constant and probably changing the surface charge on the particles. As the toluene evaporates and burns, hydroxide particle rearrangement does not occur to the same magnitude as occurs with a polar medium. Burning the toluene may also "blow" the hydroxide apart or leave a carbon layer on the hydroxide particles (Hong and Coble). Hence during calcination the hydroxide/oxide does not sinter at the same rate. This results in large but soft agglomerates. If an oxide is being slipcast, ions or salts in the water can deposit at contacts between particles (Cannon 1981). This can be useful if the green body is easily broken but harmful as the ions or salts may increase vapor phase transport causing coarsening during initial stage sintering.

Hot pressing specimens in graphite dies and controlling the atmosphere during grain growth annealing was adequate to obtain a range of grain sizes for the scientific objectives of the study. It was not

completely adequate for the engineering objectives. The oxidation of carbon contaminated samples at low temperatures often results in a fractured or bloated sample and appears to be successful only for limited ranges of grain size, temperature and zirconia composition. No samples large enough for I.R. and  $K_{IC}$  tests were produced by sintering and pseudo-isostatic hot pressing. The zirconia grain sizes obtained by this method were in the useful range.

One question that was not answered was whether the carbon or a low partial pressure of oxygen was necessary to maintain a small grain size during densification. The last samples densified (Th in sample designations) were not fired in oxygen prior to hot pressing because of this uncertainty. Available SEM pictures indicated no major effect of atmosphere on the grain growth rate, aside from bloating effects.

The carbon contamination came from both the graphite die and from the organic fluid used during powder milling. The best method of achieving theoretical density, a small grain size and no carbon contamination appears to be oxidation of a green body, sintering to the closed pore stage and isostatic hot pressing to full density.

### III.E. Conclusions

1. Fine grain size ( $< 0.5$  micron) dense  $\text{ThO}_2\text{-ZrO}_2$  can be obtained for a wide range of  $\text{ZrO}_2$  compositions by hot pressing oxide powders from hydroxide precursors.
2. Washing the Th-Zr hydroxide with organic fluids produces soft, easily milled agglomerates.
3. Carbon contamination can be a problem.



4. Initial experiments to eliminate carbon contamination were promising.

5. Gross  $ZrO_2$  grain size distribution and spatial distribution can be controlled; exacting control over the  $ZrO_2$  grain size/spatial distribution was not achieved.

#### IV. FRACTURE TOUGHNESS AND PHASE TRANSFORMATION

##### IV.A. Introduction

Griffith provided the basic understanding for the subsequent field of fracture mechanics; in brittle materials fracture originates at flaws or cracks. Irwin provided the basis by which the resistance to fracture of brittle materials could be compared, the stress intensity concept. If the flaw size distribution and stress distribution within a ceramic body are known, the fracture stress can be quantitatively predicted from the critical stress intensity factor (Evans and Langdon). Other mechanical properties of ceramics such as thermal shock and thermal or stress cycling fatigue can be at least qualitatively related to fracture toughness, flaw size distribution, slow crack growth velocity vs. stress intensity curves and relevant thermo-elastic properties. Erosion and wear are not as quantitatively related to  $K_{IC}$  due to the complex elastic-plastic processes occurring during erosion but  $K_{IC}$  is still an important materials property.

Fracture toughness can be measured by many sample geometries and methods (Evans and Langdon). Double cantilever beam, double torsion and single edge notched beam are particularly suited to ceramic materials due to their simple sample geometries. A new method now routinely applied to ceramics is the Vickers microhardness indentation test (Evans and Charles). This method is particularly simple and allows the use of small sample sizes.

That surface compressive stresses can exist when T-ZrO<sub>2</sub> bearing alloys are ground or machined was noted in Section II. With the diamond machining that must often be used with these ZrO<sub>2</sub> toughened ceramics,

compressive stress zones would be expected in all fracture toughness geometries unless extreme care is taken to eliminate these stressed zones after machining. The microhardness test needs an optically reflective smooth surface and a surface with minimal curvature.

Compressive surface stresses can exist during microhardness testing.

If a compressive layer of a large depth is present then a unique bulk  $K_{IC}$  will not be found. A linearly rising  $K_{IC}$  vs.  $C^{1/2}$  dependence would be expected for a microhardness test on a surface with a compressive stress layer which is deeper than the crack (Marshall and Lawn, 1977). Virkar (1981) has predicted and found experimentally that even without any surface stress a rising  $K_{IC}$  vs.  $C^{1/2}$  dependence could be expected for microhardness  $K_{IC}$  tests on T-ZrO<sub>2</sub> transformationally toughened materials. As the crack propagates in the semi-finite body, the crack tip stresses transform the T-ZrO<sub>2</sub> in a zone surrounding the crack. If the volume expansion produces a uniform compressive stress on the crack surface, this stress can result in an increase in the measured  $K_{IC}$  as the absolute crack size gets larger. This simple analysis is only correct if the compressive zone is as wide as the crack length, which will not be true for most cracks. However, such considerations should be modified and used to account for the compressive and tensile stresses that will be created in the volume near the crack by the roughly hemispherical plastic/elastic transformation zone around the Vickers indentation.

Usual mode I crack considerations are based on the assumption that the crack surface is stress free. This assumption is true when an idealized flat crack experiences a uniform tensile stress. As the



material near the crack strains in response to stress, a crack opening displacement (C.O.D.) occurs and the two crack surfaces are physically separated and no stress will be transmitted across the crack. With a uniform compressive stress the situation is different; the crack surfaces are closed and support compressive stresses. Measurement of an increase in  $K_{IC}$  due to a uniform compressive stress as measured by a uniform tensile stress is not effected by the initial lack of C.O.D. because as the crack is opened by the tensile field the compressive stress is not supported at the critical C.O.D. ( $K_{IC}$ ).

Stress fields which vary produce situations that are not amenable to the previous simple analyses. The compressive stress that can be supported across the crack plane depends decisively on the local C.O.D. and the critical C.O.D. necessary near the crack tip for crack propagation at  $K_{IC}$ . There can be situations where the local C.O.D. is zero and the crack supports compressive stresses while the crack tip is at  $K_{IC}$  and propagating. Thus, there are situations where transformation zones behind the crack tip may assist crack propagation. Alternatively if the C.O.D. is positive, compressive stress can reduce  $K_I$  for the crack, but stresses in regions for which the polar angle relative to the crack tip approaches  $\pi$  will have little effect. Thus, proper modelling of the local C.O.D. and of the extent of the compressive zone is essential.

Recent examinations of the microhardness fracture toughness test via simplified elastic/plastic fracture mechanics methods have raised some doubts as to the correlation of the results obtained with this method and other testing geometries and the accuracy of the theoretically obtained formulas for  $K_{IC}$  (Lawn et al., 1980, Anstis et al., 1981, Bhat, 1981).

Different formulas derived theoretically for determining fracture toughness are given in each paper (and the papers have overlapping authors); when identical data is used the theoretically derived formulas give  $K_{IC}$ 's that differ by a factor of two. The differences result from approximations used in treating the residual stresses due to plastic deformation around the hardness indent. Despite the forgoing arguments, Becher (1981) has found excellent agreement between double cantilever beam and indentation fracture energies measured by the empirical Evans and Charles curve ( $\gamma_{IC} = (K_{IC})^2/2E$ ) for well characterized  $Al_2O_3$ - $ZrO_2$  alloys that showed toughening behavior. We anticipate that by using the empirically derived curve of Evans and Charles and avoiding surface compressive stresses a good comparison between toughened materials can be obtained via indentation toughness measurement.

The fracture toughness of  $ThO_2$  (8% porosity) was reported for room temperature,  $1.1 \text{ MPam}^{1/2}$  (Matzke, 1980) and as a function of temperature ( $1.1 \text{ MPam}^{1/2}$  at  $25^\circ\text{C}$  to  $0.8 \text{ MPam}^{1/2}$  at  $400^\circ\text{C}$ ) using Hertzian indentation (Inoue and Matzke, 1981).

Direct methods for phase identification include TEM, X-ray diffraction and Raman scattering. Indirect methods include thermal expansion and elastic modulus measurements. If thermal expansion curves on heating and cooling show distinctive breaks, sometimes even contraction on heating or expansion on cooling, and significant hysteresis, the M $\rightarrow$ T and T $\rightarrow$ M transformations are probably occurring. If the thermal expansion behavior is not repeatable in the sense that some permanent length change occurs upon thermal cycling, then microcracking or creep deformation is taking place. Elastic modulus measurements as a function

of temperature produce more direct evidence for the occurrence of microcracking which implies transformation.

#### IV.B. Experimental Method

In early experiments, little effort was expended in examining effects of various types of surface finishing techniques or low temperature annealing on  $K_{IC}$ . Later data were obtained that proved both polishing and annealing were important. Thus, experimental methods became standardized.

As noted in Section III, most samples were ground and polished through three grits of SiC and two of  $Al_2O_3$ . After the initial polish a flat surface was obtained, and for further measurement after a grain growth annealing, the maximum SiC grit used was 20 microns, followed by the  $Al_2O_3$ . Usually only the  $Al_2O_3$  was necessary. Samples with Th in their designation (Tables VII and X) were polished mechanically using a maximum diamond size of 3 microns, unless otherwise noted. This was followed by 1 micron diamond, 0.3 micron  $Al_2O_3$  and 0.06 micron  $Al_2O_3$ . After annealing, only alumina polishing was necessary to obtain a surface smooth enough to perform  $K_{IC}$  measurements.

Several annealing experiments at temperatures of 1200°C to 1250°C were performed. The polishing method was noted and  $K_{IC}$  measured. The sample was wrapped in graphoil and annealed for about one-half hour in a reducing or a zirconia-carbon buffered CO atmosphere. The minimum polishing necessary to produce a flat surface after the 1200°C to 1250°C annealing was only 0.3 micron and 0.06 micron  $Al_2O_3$ .  $K_{IC}$  was then measured after careful polishing.



$K_{IC}$  was measured by using the Vickers microhardness indentation technique and calculated using the empirical curve of Evans and Charles (Figure IV.1). For dense, uncracked samples,  $E_0$  of 240 GPa was used for all  $ZrO_2$  mole fractions. To approximately account for the effects of porosity and microcracking,  $E$  was modified by the relation  $E = H (E_0/H_0)$  where  $H_0$  was taken as 11 GPa (measured on dense samples) and  $H$  was the hardness for a given sample. Indentation loads varied from 0.1 to 6 Kg; the reported data are from 1 Kg and 2 Kg loads except as noted. Semi-quantitative spectrographic impurity analysis was performed on a few samples. X-ray, SEM and TEM characterization was described above.

#### IV.C. Results

##### IV.C.1. Spontaneous Fracture

Spontaneous fracture in  $ZrO_2$  bearing ceramic alloys can arise from several possible causes. First, the T- $ZrO_2$  may transform to M- $ZrO_2$ . During and after transformation, cracks may form and grow. If a sufficient density and length of cracks are formed, the material macroscopically fails. Secondly, if an annealing treatment is performed at a different partial pressure of oxygen from that for the fabrication step, during annealing the thoria and zirconia lattice parameters may change at different rates (Lange, 1980). If the annealing step is at a low temperature, diffusional creep processes may not reduce stresses caused by the lattice parameter changes. A third process is the creation of pores (containing gases at high pressures) by chemical reactions.

All processes that create local areas of high tensile and shear stress,  $\Delta\alpha\Delta T$ ,  $\Delta P_{O_2}$  expansion, and high pressure pores can aid the trans-

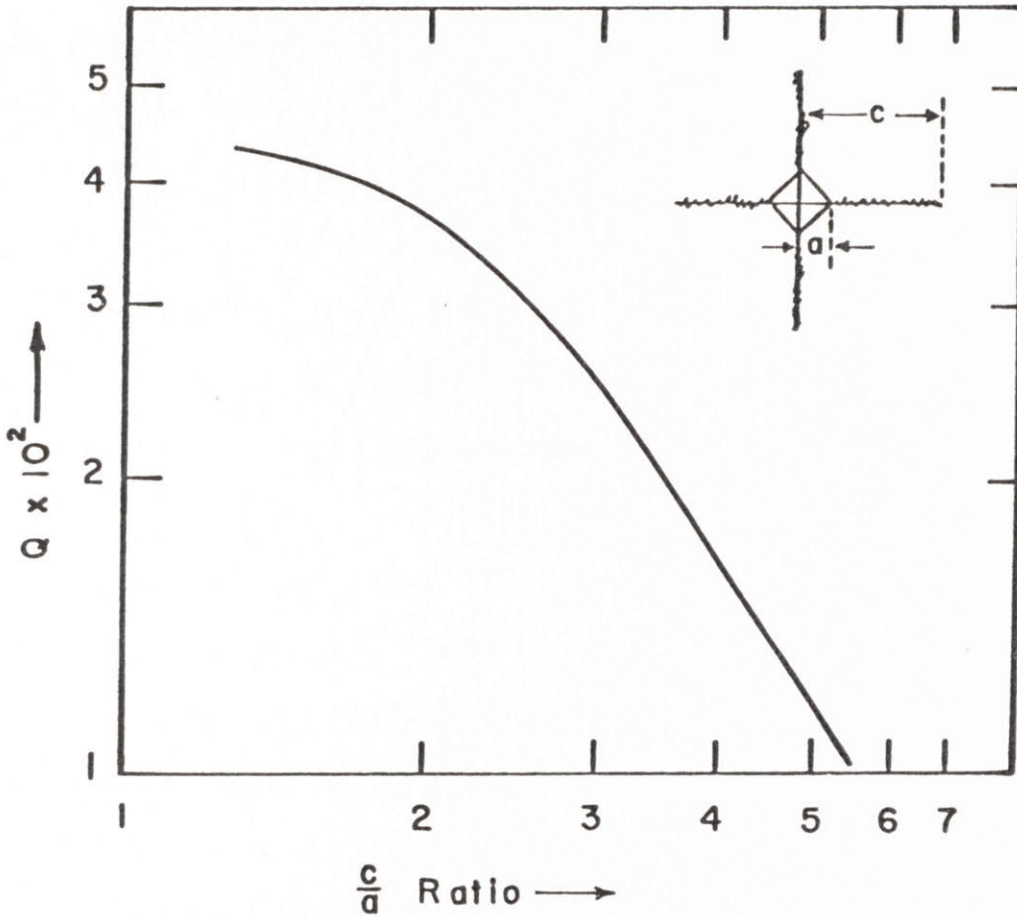


Figure IV 1 Empirical curve of Evans and Charles used for fracture toughness measurement.

$$Q = \frac{3 K_{IC}}{H(a)^{1/2}} \left( \frac{H}{3E} \right)^{.4}, \quad c = \text{crack length}$$

from center of indent impression,  $a$  = half indent diagonal.

formation of T-ZrO<sub>2</sub> to M-ZrO<sub>2</sub>. The pores also act as elastic inhomogeneities with sharp (dihedral angle) edges that aid microcrack formation. If an oxide ceramic at room temperature has high local body stress, the ceramic can fracture over a period of time by slow crack growth via water vapor corrosion.

Numerous samples that were dense, whole and intact after hot-pressing fractured into greater than ten pieces after oxidation at 900°C and 1100°C. In several instances a major portion of the macroscopic fracture occurred on cooling. The sample was observed to be unfractured while at temperature but to fracture during slow cooling, often accompanied by loud acoustic emissions. Macroscopic fracture did not occur as a result of oxidation in sample H-90-B1 which was only about 90% dense before the oxidizing anneal, but did occur in otherwise similar samples which were denser. Sample H-85-A1 was of particular interest. Dense and unfractured after hot-pressing, the sample was annealed in air at 900°C for 20 hours. This time and temperature was insufficient to oxidize the full thickness of the sample as the interior was still dark gray after annealing. The exterior, however, was fractured so extensively that the outer 1 mm was reduced to dust. The interior also fractured but large, 3 cm diameter, pieces remained. At higher temperatures (>1200°C), the entire sample could have been oxidized in less than 4 hrs without fracture.

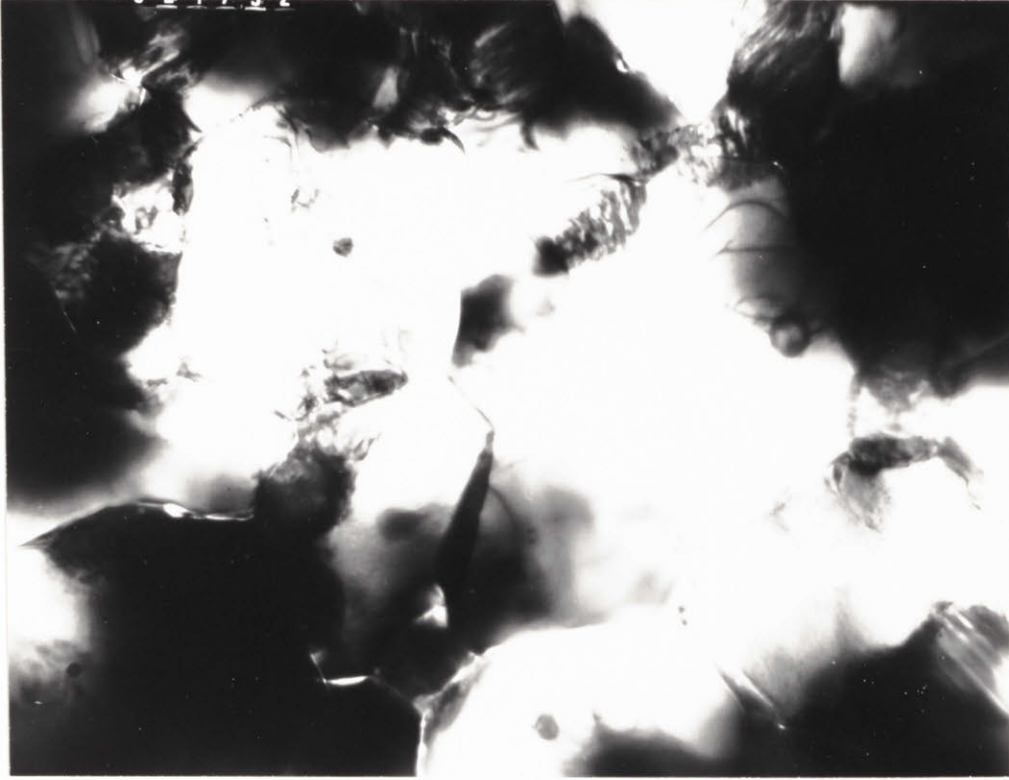
If the partial pressure of oxygen is the same during sample fabrication and grain growth annealing, the sample may still fracture. H-85-E and H-80-C both fractured into many pieces after hot-pressing and annealing; both had average ZrO<sub>2</sub> sizes of 1 micron or greater. H-70-A and H-54-A were fractured into several pieces after hot-pressing.



After extensive grain growth annealing, most samples would fracture or contain cracks large enough to be seen without magnification: H-85-H, -J, -K, -L, -Th, H-70-A and H-54-A, -B. For the dense 15 m/o to 20 m/o  $ZrO_2$  material, the average  $ZrO_2$  grain size at which the fracture often occurred was 1 to 2 microns. Some grains or areas of adjacent  $ZrO_2$  grains reached 10 microns without macroscopic failure. The average  $ZrO_2$  grain size for spontaneous fracture in higher  $ZrO_2$  concentration materials was smaller, 0.3 to 0.4 micron for 30 m/o and 46 m/o  $ZrO_2$ .

Several samples appeared to fail via slow crack growth at room temperature. H-80-C was whole and intact immediately after annealing. After 12 hours at room temperature, it had cracked into several pieces and a slight pressure by twisting the sample by hand resulted in many (greater than 20) pieces. H-85-D2 was a sample of particular interest. After grain growth anneals, the thick sample (about .5 cm) was sliced into three thin (about 1mm) sections, then oxidized at 1230°C. After oxidation, the majority of the sample (about 90%) was translucent. Areas within the sample were opaque and the opaque regions grew at the expense of the translucent region over a period of about 1.5 years, at room temperature and normal atmospheric humidity, until the majority of the sample (about 70%) was opaque. TEM examination revealed ultra fine porosity in the translucent region (Figure III.17) and micro-cracking in the opaque region (Figure IV.2).

Although samples H-85-F and H-85-G both contained large (20 micron or larger) areas of zirconia grains, they were not fractured in a macroscopic sense. The as-sintered surfaces of sintered samples produced from oxalates contained many cracks 10 microns to about 100 microns in



1  $\mu\text{m}$

Figure IV 2 Dislocations, microcracks and twinned  $\text{ZrO}_2$  in  $\text{ThO}_2$ -15 m/o  $\text{ZrO}_2$ . Foil from sample H-85-D2. Foil and TEM picture by J. Schneibel.

length (Figure IV.3a). The interiors of the oxalate precursor sintered samples observed after polishing did not contain cracks large enough to be seen by optical microscopy or SEM. However, fractured surfaces revealed much microcracking (Figure IV.3b). These hot-pressed and sintered samples do not seem to be susceptible to macroscopic failure despite the large  $ZrO_2$  grain size and wide grain size/spatial distribution. The porosity probably accounts for this.

#### IV.C.2. Fracture Toughness

The accuracy and variability of data obtained by the microhardness method of  $K_{IC}$  measurement can depend on two material parameters and possibly the changing perception of an investigator. The homogeneity of a material on the size scale affecting the crack tip and homogeneity on the size scale of the distance between the most widely spaced indents can alter reported  $K_{IC}$ 's. Section III presented several examples where the second size scale might affect  $K_{IC}$  measurement, the definition of the size scale affecting the crack tip is at present elusive.

As most of the data to be reported was obtained over a three year period by optical microscopy with little photographic record, a discussion of possible measurement error due to shifting bias of the investigator is warranted. Crack tips can be difficult to define in both optical microscopy and SEM. As the  $ThO_2-ZrO_2$  were intended for optical purposes, most specimens were somewhat transparent for 10-100 $\mu$ m depths into the specimens. This caused difficulty in focusing on a polished surface. In addition, scattering from the interior could obscure the crack tip position. Gold coating of surfaces reduced both problems. The crack tip position was defined as the maximum distance

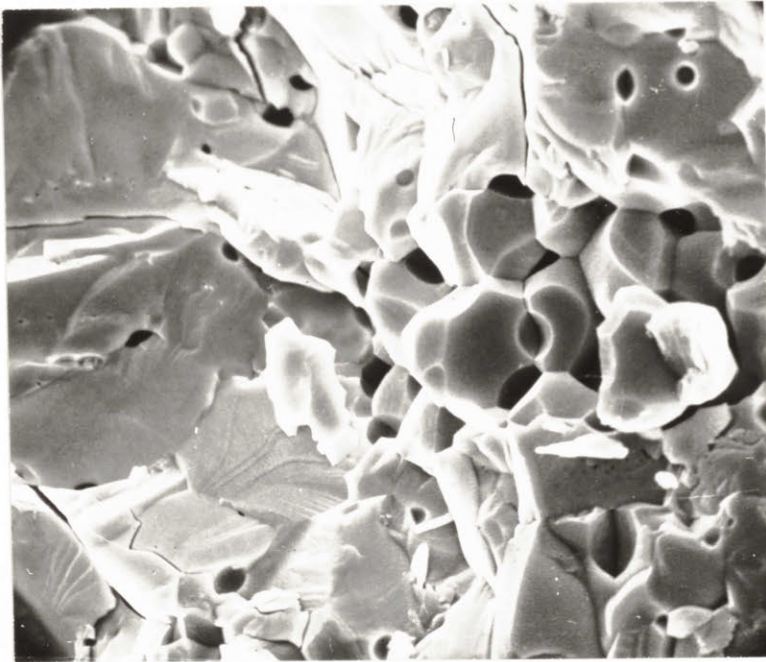


A.



5  $\mu$ m

B.



5  $\mu$ m

Figure IV 3 Microcracks in  $\text{ThO}_2$ -15 m/o  $\text{ZrO}_2$  sintered sample. Powder from thorium oxalate and  $\text{ZrO}_2$ . As sintered surface A, and fracture surface, B.

any radial/median crack obtained and was found by altering the focus of the microhardness microscope. Smooth surfaces presented less difficulty in finding crack tips as surface roughness could obscure the tips. The author became more critical and measured crack lengths may have become slightly longer as the project continued. Thus  $K_{IC}$ 's calculated may have decreased slightly over the course of the project.

What is the possible magnitude of this decrease? For a hardness of 9.5GPa the crack lengths and indent impression lengths are listed in Table VI and drawn schematically in Figure IV.4 for various  $K_{IC}$ 's at 1 kg and 2 kg loads. The differences in crack lengths for  $K_{IC}$  values  $0.5 \text{ MPam}^{1/2}$  apart are all  $>10$  microns. The author believes that he could have biased the crack length (C) measurements by +5 microns over a three year period. Considering this and the crack length differences between various  $K_{IC}$ 's, differences between  $K_{IC}$ 's of  $0.5 \text{ MPam}^{1/2}$  are viewed as significant while differences of  $\sim 0.2 \text{ MPam}^{1/2}$  between samples measured several years apart may not be significant.  $K_{IC}$ 's for individual indents on one sample for one load typically varied by less than  $\pm 0.15 \text{ MPam}^{1/2}$  from the average  $K_{IC}$ . Variability between average values of  $K_{IC}$  measured at 1 kg and 2 kg loads for a single sample was usually less than  $0.3 \text{ MPam}^{1/2}$ . Hence measurement difficulties are viewed as the limitation on accuracy and significance for the fracture toughnesses to be reported, variability within samples and between indentation loads is less important. One example is available where a photographic record (SEM) of a  $K_{IC}$  measurement taken early in the project can be compared to the written record and there is little difference between the two calculated  $K_{IC}$ 's (H-85-B9, see below).

Table VI

Crack Sizes for H = 9.5 GPa

For 1 kg indent, half indent diagonal, a=22 microns.

<u><math>K_{IC}</math>, MPam<sup>1/2</sup></u>	<u>C, microns</u>	<u>c/a ratio</u>
1.5	77	3.52
2.0	64	2.91
2.5	52	2.36
3.0	41	1.85
3.5	<26	1-1.2

For 2 kg indent, half indent diagonal, a=31 microns.

<u><math>K_{IC}</math>, MPam<sup>1/2</sup></u>	<u>C, microns</u>	<u>c/a ratio</u>
1.5	122	3.92
2.0	103	3.32
2.5	86	2.78
3.0	73	2.35
3.5	61	1.95
4.0	42	<1.35



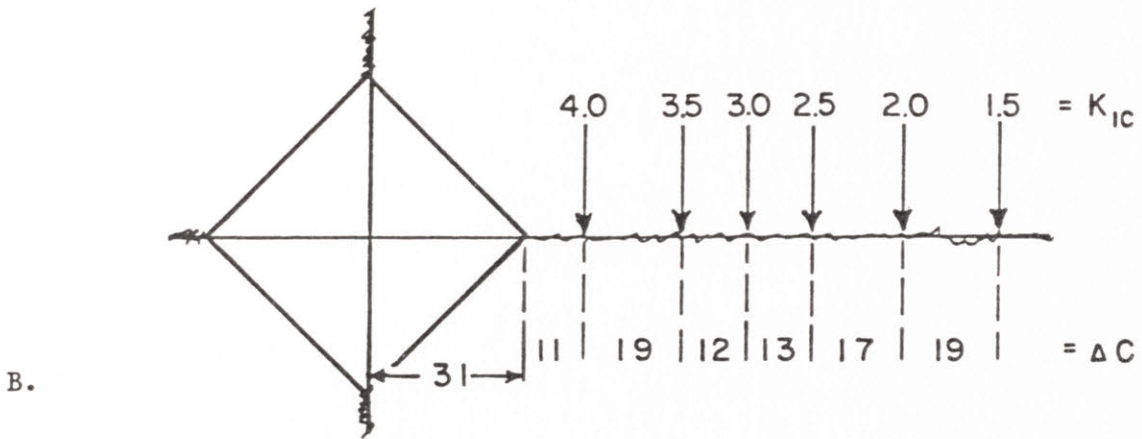
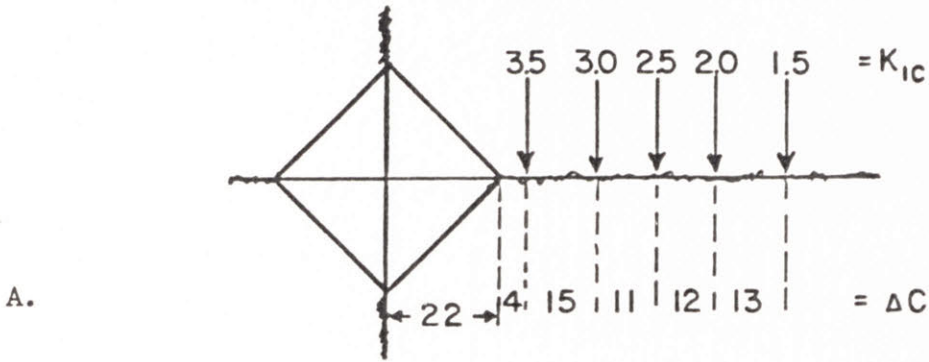


Figure IV 4 Schematic of crack sizes for various  $K_{IC}$ 's,  $H = 9.5$  GPa,  $E_0 = 240$  GPa,  $H_0 = 11$  GPa. A, 1 Kg load; B, 2 Kg load. Lower numbers are distance in microns between crack sizes for given toughnesses, upper numbers ( $\text{MPa m}^{1/2}$ ).

The effect of  $ZrO_2$  content on the fracture toughness of dense  $ThO_2$ - $ZrO_2$  at  $ZrO_2$  grain sizes of 0.1-0.3 micron and normal size distributions is shown in Figure IV.5. The volume fraction of the  $ZrO_2$  phase(s) is 3-6% less than the molar fraction, because the molar density of the  $ZrO_2$  is somewhat higher than that for  $ThO_2$ . Only data from materials greater than 98% dense are plotted. The fracture toughness increases with  $ZrO_2$  content for the as-hot-pressed materials. The minimum fracture toughness at these grain sizes can be below the solid line.

With the microhardness indentation technique,  $K_{IC}$  values can depend on the surface preparation for  $ZrO_2$  toughened materials. The measured toughness can be high after a rough grind and polish. For  $ThO_2$ , -20 m/o  $ZrO_2$ , -30 m/o  $ZrO_2$  and -46 m/o  $ZrO_2$  alloys, a surface rough ground with 35 micron grit abrasive to intentionally produce a surface compressive layer followed by minimal polishing routinely gave a measured  $K_{IC}$  value 0.7-1.2  $MPam^{1/2}$  higher than on a surface that was only polished with grit sizes less than 3 micron or was as-annealed, Figure IV.5, Table VII. Isolated measurements on H-70-Th1 were as high as 5.8  $MPam^{1/2}$ . These surface preparation conditions are distinguished in Fig. IV.5 and subsequently. Early data where compressive surface layers were not intentionally produced are labeled "ground and polished" on Fig. IV.5 and subsequently; these seem to produce higher measured  $K_{IC}$ 's than similar samples only lightly polished with 3 micron diamond.

The explanation for these observations may involve compressive stresses and/or microcracking near the surface caused by the T to M transformation induced by grinding and polishing. Although it is thought that either careful polishing or polishing and brief low temperature re-annealing should give representative results, re-annealing

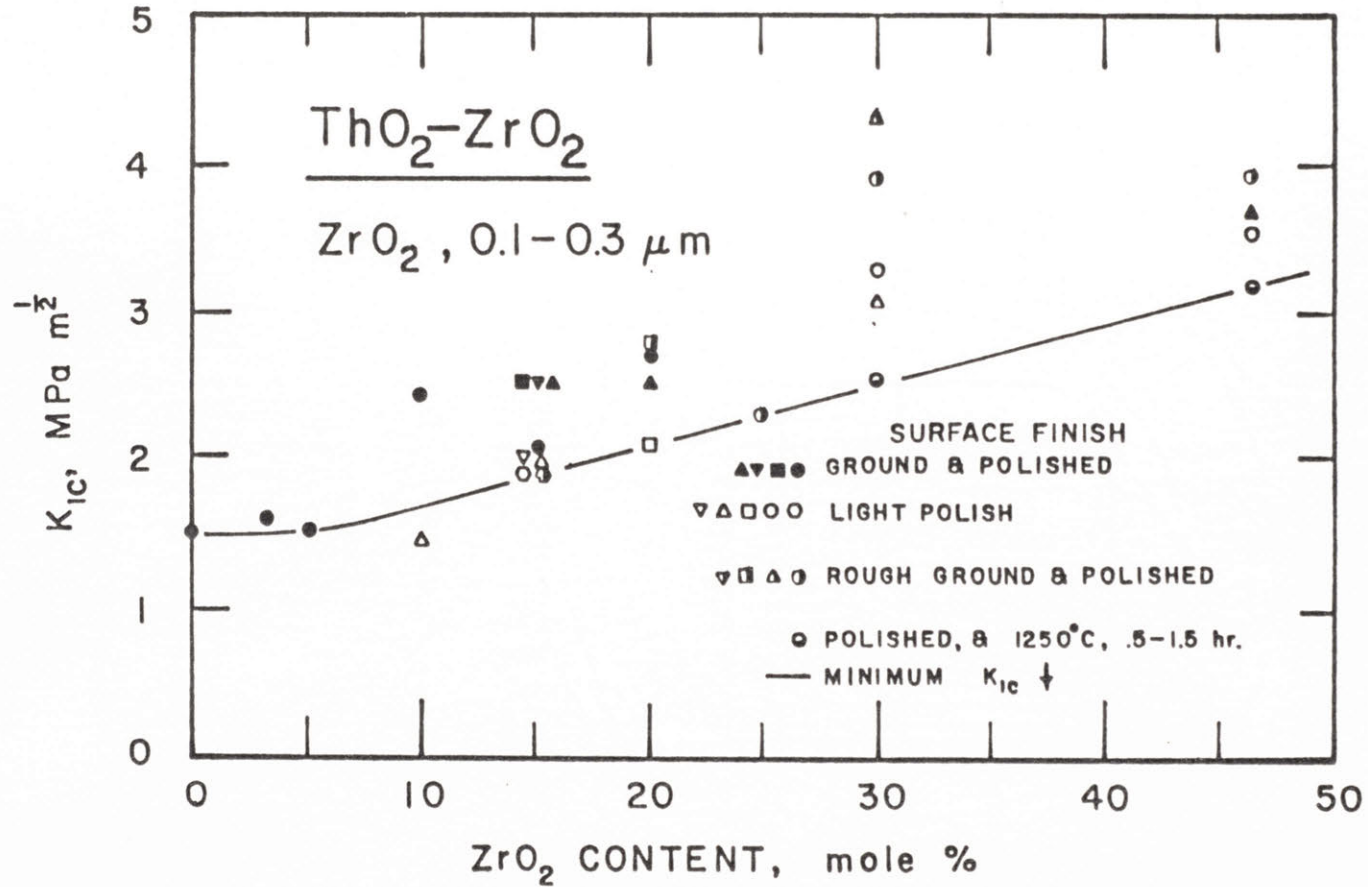


Figure IV 5 Effect of ZrO<sub>2</sub> content on the toughness of dense ThO<sub>2</sub>+ZrO<sub>2</sub>. The ZrO<sub>2</sub> grain size was 0.1-0.3 μm in all samples. Minimum K<sub>1c</sub> for these ZrO<sub>2</sub> grain sizes is at or below the solid line. The volume fraction of particles is 3-6% less than the molar fraction.



Table VII

Effects of Surface Condition

A. Attempts to induce surface compressive layers

Sample #	M%ZrO <sub>2</sub>	K <sub>IC</sub> MPam <sup>1/2</sup>	H GPa	Grain size	Surface <sup>+</sup> finish	Comments
H-80-Th 1 a	20	2.1	11.5	.2	3	as hped
b	20	2.8	11.2	.2	35	
H-75-Th 1 a	25	-	-	.1	3	as hped
b	25	2.3	10.3	.1	35	
H-70-Th 1 a	30	3.1	12.4	.1	3	as hped
b	30	4.3	12.3	.1	35	

B. Effect of 1/2 hr 1250°C annealing, reducing atmosphere

Sample #	M%ZrO <sub>2</sub>	K <sub>IC</sub> , MPam <sup>1/2</sup>	H, GPa	Surface finish <sup>+</sup>	
H-85-I 4 (H-85-I + 15 hr at 1600°C)	15	before anneal	2.9	10.4	35
		after anneal	2.3	10.0	0.3
H-70-A1 (as hped)	30	before anneal	4.0-3.5	10.7	35
		after anneal	2.5	10.7	0.3
H-54-B6 (as hped)	46	before anneal	3.9-3.5	10.8	35
		after 1.5 hr anneal		10.9	0.3
		rough grinding <sup>3.1</sup> and polish	4.1	10.7	35
		additional 1/2 hr. 1250°C reducing atm. anneal	3.2	10.8	0.3

<sup>+</sup>Maximum grit size used in grinding/polishing before and after annealing in microns.

lowers the measured  $K_{IC}$  and may not restore the bulk condition (Table VIIb). The present observations are insufficient to be certain whether these results indicate a hysteresis in the transformation or other damage which affects the toughness.

The effect of  $ZrO_2$  content on the fracture toughness of annealed  $ThO_2-ZrO_2$  is shown in Figure IV.6. Only data from materials greater than 98% dense after annealing are plotted. These data indicate both the effect of  $ZrO_2$  grain size and surface preparation. The data plotted are the highest values of  $K_{IC}$  found after all anneals for each hot pressed material. They do not necessarily represent the maximum achievable toughnesses for a particular  $ZrO_2$  content and surface condition as there are only limited data for most compositions, but they do indicate that higher toughnesses were achieved with particle sizes larger than 0.1-0.3 microns, at least with the lower  $ZrO_2$  contents. The high values are associated with grinding but not necessarily simply with surface compressive stresses. However for some samples the  $K_{IC}$  would increase with annealing whereas the  $K_{IC}$  of similar samples would decrease with annealing for the same  $ZrO_2$  grain size range with the same  $ZrO_2$  content. The differences between these samples depended on surface preparation and sometimes other factors. At the highest  $ZrO_2$  contents, the range of annealing temperature and time (grain size) that could be used to improve the  $K_{IC}$  was extremely limited, Table VIII. Most anneals resulted in fractured samples.

Although sintered samples from oxalate precursors had a poor density due to large  $ZrO_2$  agglomerates, their  $K_{IC}$  and fracture behavior was interesting. A trend of increasing fracture toughness with increasing

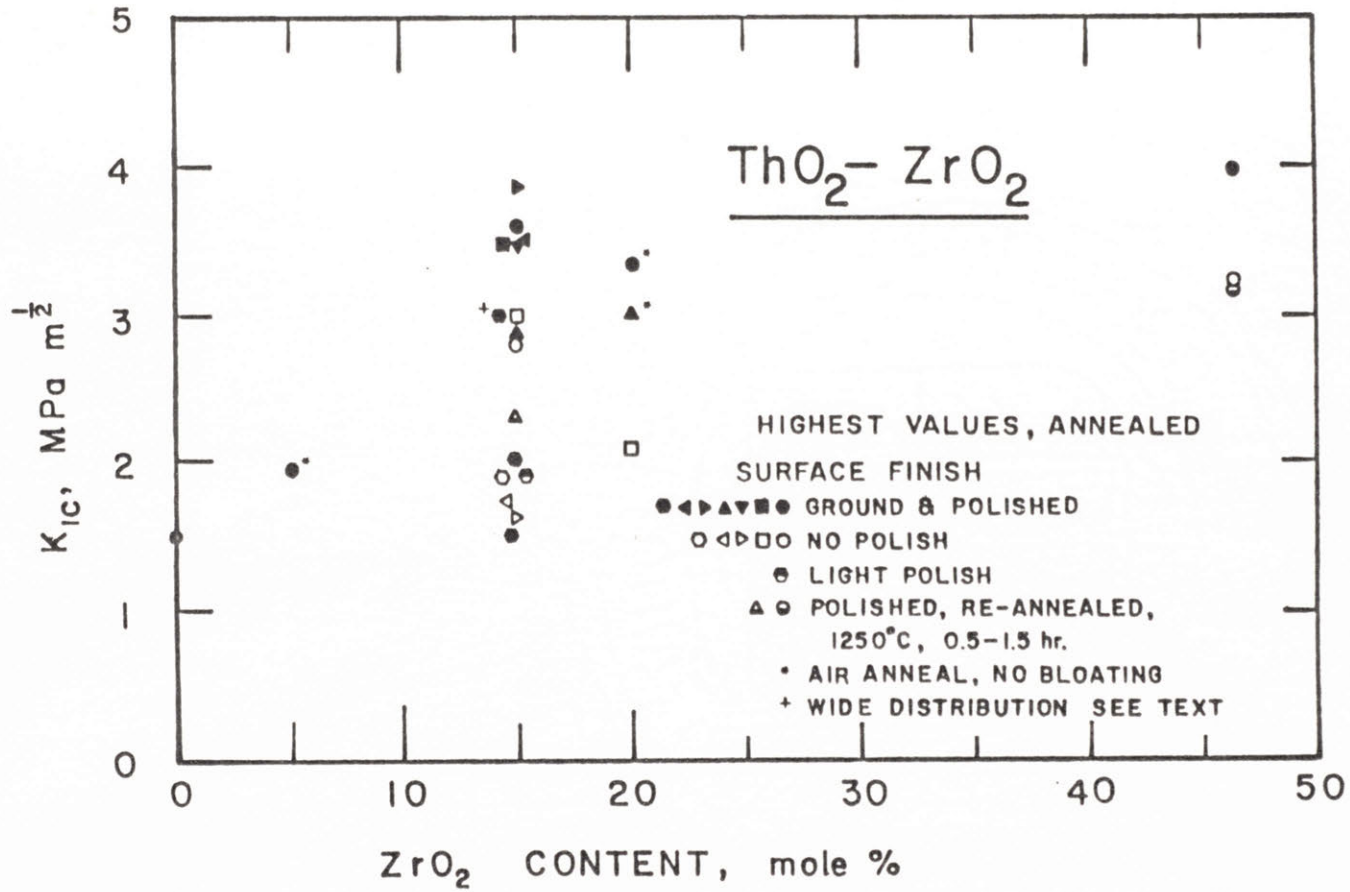


Figure IV 6 Effect of ZrO<sub>2</sub> content on the toughness of dense ThO<sub>2</sub>+ZrO<sub>2</sub>. The annealed values are the highest measurements to date on unbloomed samples for each hot pressed material. The volume fraction of particles is 3-6% less than the molar fraction.



Table VIII

Toughness of Annealed ThO<sub>2</sub>-46 m/o ZrO<sub>2</sub>

K<sub>IC</sub>, MPam<sup>1/2</sup>/H, GPa

<u>H-54-B #</u>	<u>Anneal</u>	<u>K<sub>IC</sub>, MPam<sup>1/2</sup>/H, GPa</u>		<u>Comments</u>
		<u>As annealed surface</u>	<u>Polished</u>	
B1			3.5/10.5	
B5	1250°C/.5 hr		3.9/10.8	
B6	1250°C/1.5 hr	3.1/10.9	4.1/10.7	
B8	1250°C/5 hr + 1250°C/0.5 hr	3.4/10.3	3.8/10/7	
B10	1300°C.1 hr + 1350°C/4 hr + 1250°C/4 hr + 1250°C/.5 hr	3.2/10.7		
B4	1350°C/1.5 hr + 1250°C/.5 hr	3.1/10.6	4.2/11	
B3	1450°C/ 1 hr		4/9	Overaged
B2	1600°C/ 3 hr			Fractured
H-54-A				
A1	-	-	4.0/9.1	
A6	1250°C/ .5 hr			Fractured
A7	1250°C/.5 hr			surface cracked
A5	1350°C/1.5 hr			fractured
A4	1450°C/1 hr			fractured
A3	1600°C/4.5 hr			fractured

ZrO<sub>2</sub> content is found in these samples, Fig. IV.7. Two significant differences occur between the sintered and hot pressed materials. The hardness for the sintered material is low, 6-4 GN/m<sup>2</sup> at higher ZrO<sub>2</sub> contents, compared to the hot pressed material 11-9.5 GN/m<sup>2</sup> (not overaged). At higher ZrO<sub>2</sub> mole fractions, the crack patterns produced by the indentation are not regular, there is multiple cracking near the corners of the indent impressions and often cracks propagate from the edge of the impression perpendicular to the impression side (Fig. IV.8). Thus, the values given for K<sub>IC</sub> of sintered material for 15 and 20 m/o ZrO<sub>2</sub> in Fig. IV.7 are only approximate.

The effect of annealing time at 1600°C on fracture toughness for ThO<sub>2</sub> + 15 m/o ZrO<sub>2</sub> is shown in Figure IV.9. As the particle size (annealing time) increases, the toughness can, but does not always increase to a peak before it decreases. The range of average ZrO<sub>2</sub> grain sizes covered during annealing at the shorter times given in Fig. IV.9 is similar for the separate samples, 0.3-0.8 microns.

A possible source of uncertainty results because some of the data shown for annealed samples of H-85-B that were ground and then polished are from pieces which were oxidized at 1200°C after the grain growth anneal at 1600°C in a reducing atmosphere. The data from H-85-D, H-85-H, H-85-I and H-85-Th samples were taken with reduced pieces. Also for most curves the data were from repeat annealings of a single piece; for H-85-Th individual samples were annealed once, except as noted in Table X.

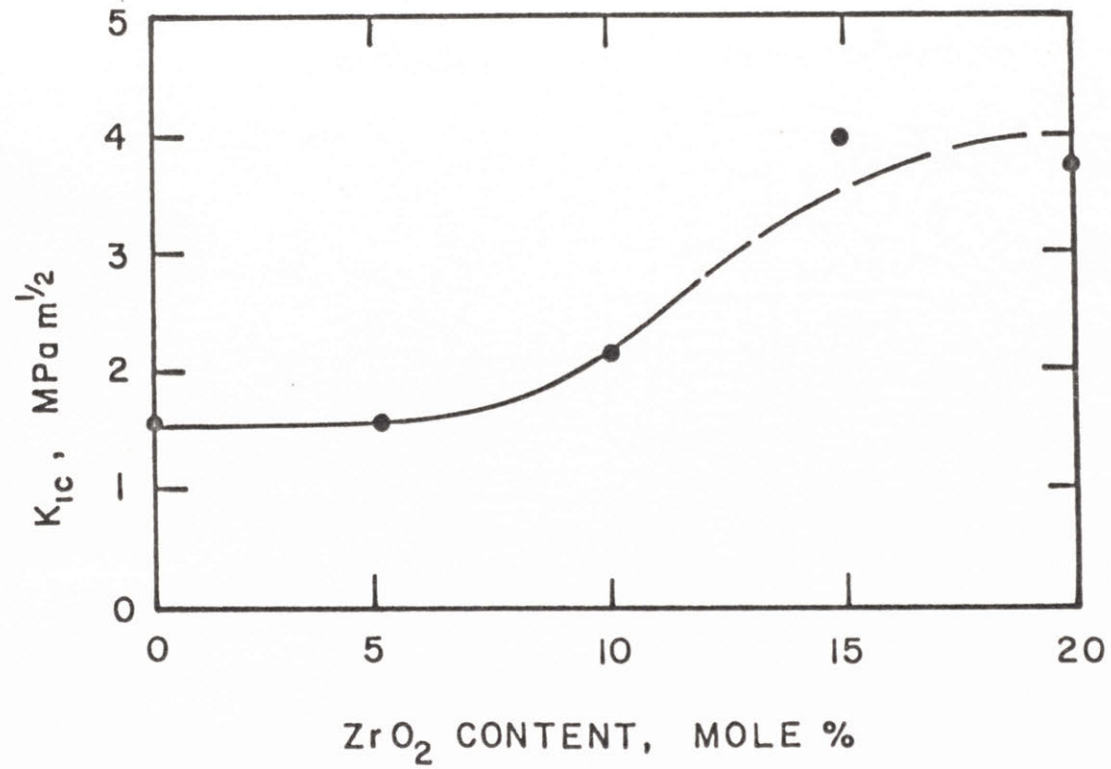
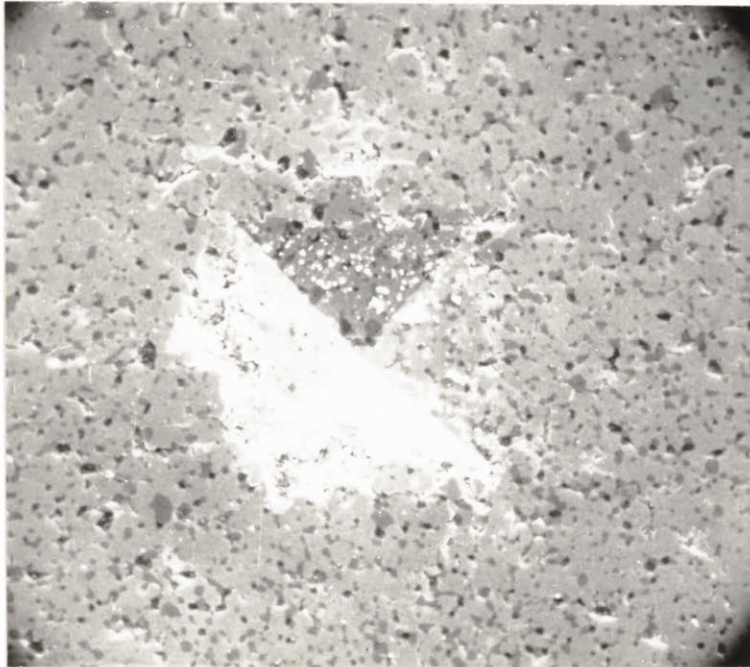


Figure IV 7 Approximate  $K_{IC}$  for porous sintered specimens. Densities greater than 93%. All surfaces were ground and polished.





—  
20  $\mu\text{m}$

Figure IV 8 Indent impression in  $\text{ThO}_2$ -20 m/o  $\text{ZrO}_2$ . Sintered, oxide powder from thorium oxalate and  $\text{ZrO}_2$ . 1 Kg load.

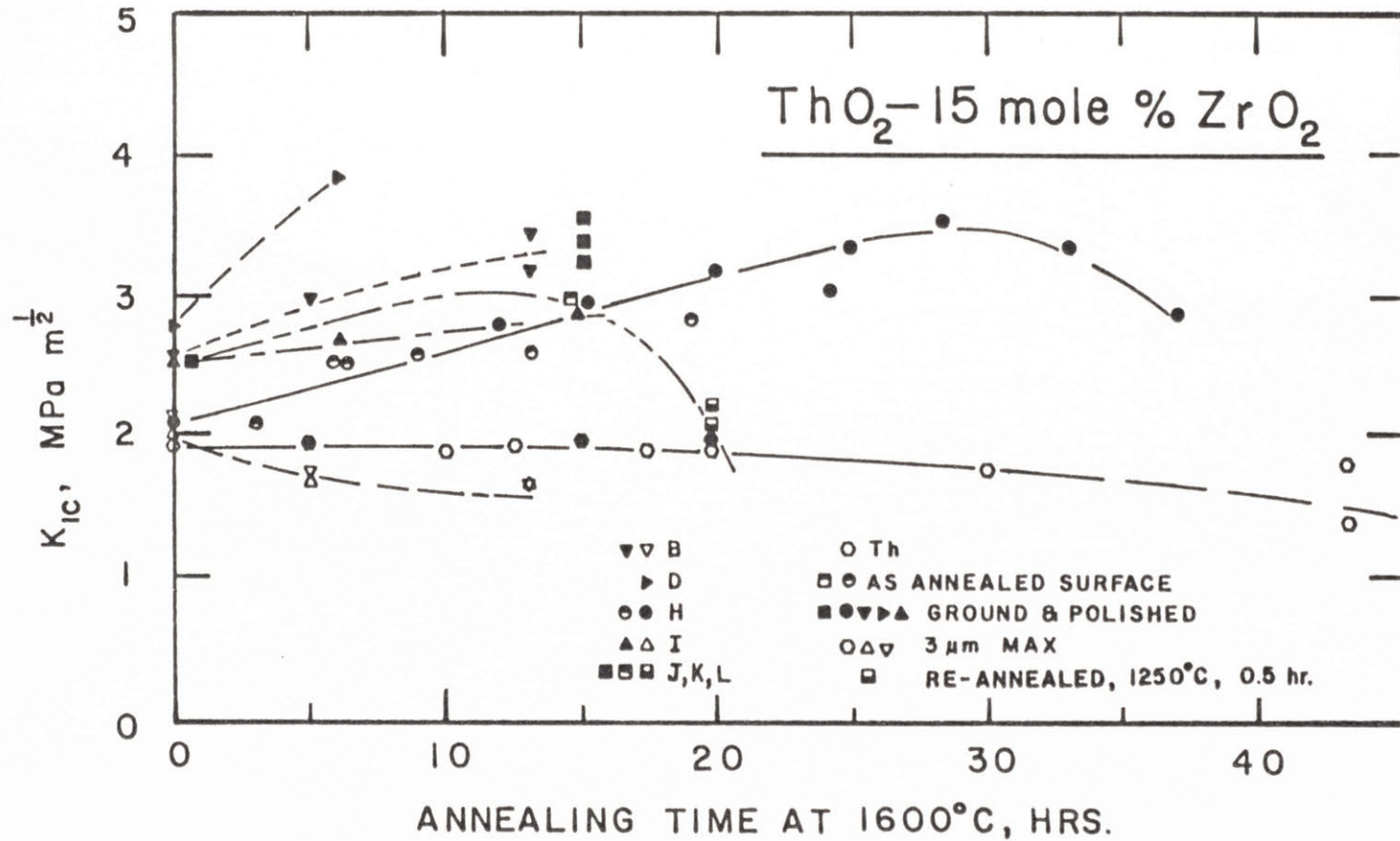


Figure IV 9 Effect of annealing on the toughness of hot pressed  $\text{ThO}_2$  + 15 m/o  $\text{ZrO}_2$ . The curves reflect the dependence of  $K_{IC}$  on particle size,  $\sim 0.3$  to  $>1.0$  micron, as the volume fraction of  $\text{ZrO}_2$  is constant at  $\sim 11\%$ .

No increase in  $K_{IC}$  as annealing time (grain size) increased was found for samples from parent hot pressings H-85-B, H-85-I, and H-85-Th when the maximum grit size for polishing was 3 microns or less. If samples from parent hot-pressings H-85-B and H-85-I were ground with 35 and 20 micron SiC before annealing and/or  $K_{IC}$  testing then an increased  $K_{IC}$  was measured, as annealing time (grain size) increased. Most of sample H-85-Th was exceptional in that rough grinding was usually ineffective after any annealing condition.

One experiment suggests an effect of grinding and thermal cycling on  $K_{IC}$ . A portion of H-85-B was polished on both sides with a maximum grit size of 3 microns, then annealed at 1600°C for 13 hrs. A  $K_{IC}$  of 1.6 MPam<sup>1/2</sup> was measured (H-85-B15 Table IX). One side of the sample was then rough ground and polished and  $K_{IC}$  measured as 2.1 MPam<sup>1/2</sup>. The sample was annealed for an additional 5 hrs. at 1600°C (now H-85-B16) and both sides were rough ground and polished. The side that had been ground before the 5 hr anneal now had a  $K_{IC}$  of 2.3 MPam<sup>1/2</sup> while the side that was rough ground and polished only after the 5 hr anneal had a  $K_{IC}$  of 1.8 MPam<sup>1/2</sup>, Table IX.

For most individual samples from parent hot pressing, H-85-Th no grain size, grinding, annealing or oxidation combination achieved a  $K_{IC}$  above 2.1 MPam<sup>1/2</sup>, Fig. IV.9, Table X. These samples had a medium to narrow ZrO<sub>2</sub> grain size distribution with fairly uniform ZrO<sub>2</sub> spatial distribution, Fig. III.4 and IV.10. Since this result at first seemed to be anomalous, a semiquantitative impurity analysis was performed for several samples exhibiting high toughness and some with low toughness for similar ZrO<sub>2</sub> grain sizes (Table XI). No chemical difference that



Table IX

Toughness of Miscellaneous Samples

Sample #	M%ZrO <sub>2</sub>	K <sub>IC</sub> MPam <sup>1/2</sup>	H,GPa	Grain size	Surface <sup>+</sup> finish	Comments
H-97-Th	3	1.6	9.8	-	35	As Hped
OH-95-A1	1-5	1.6	9.9	1	55	1000°C 20hr air anneal
H-90-Th	10	1.4	9.3	.3	35	As hped
H-80-Th 1 a	20	2.1	11.5	.2	3	As hped
H-80-Th 1 b	20	2.8	11.2	.2	35*	
H-80-Th-3	20	2.0	10.2	-	3	10hrs 1600°C
H-80-Th-4	20	1.5	10.2	-	3	20hrs 1600°C
H-80-Th-5	20	2.1	11.3	-	3	5hrs 1500°C
HSF-85-C	15	~2	~11	.3	3	As hped
H-85-G	15	3.1	9.6	-	55	wide size dist. see text & fig III.7

<sup>+</sup> maximum grit size used in grinding/polishing in microns.

\* attempted to induce surface compressive layer.

Table IX  
(Cont'd.)

<u>Sample #</u>	<u>m/o ZrO<sub>2</sub></u>	<u>K<sub>IC</sub>,<sup>1/2</sup> MPam</u>	<u>H GPa</u>	<u>Grain size</u>	<u>Surface Finish<sup>+</sup></u>	<u>Comments</u>
H-85-D2 a	15	3.8	9.4	.6	55	Optical-measured Fall 1979
b	15	2.6	9.4	.6	55	SEM - measured Fall 1981 not microcracked
c	15	3.4	9.6	.6	55	SEM - measured Fall 1981, microcracked
H-85-B9 a	15	3.4	9.6	-	55	optical - measured summer 1979
b	15	3.3	9.7	-	55	SEM - taken 1979
H-85-B10 a	15	3.2	-	-	55	optical - measured 1979
b	15	2.6	9.7	-	55	optical - measured Fall 1981
H-85-B15 a	15	1.6	9.8		3	13 hr at 1600°C
b	15	2.1	9.4		55*	
H-85-B16 a	15	2.3	9.8		55*	H-85-B15 + 5hr 1600°C
b	15	1.8	9.8		55*	surface (a) rough ground before anneal
H-85-H4 a	15	2.5	-		-	oxidized at 1220°C before
b	15	2.1	-		-	5 hr (a) and 10 hr (b) anneal at 1600°C; heavily microcracked by TEM

<sup>+</sup> maximum grit size used in grinding/polishing in microns.

\* attempted to induce surface compressive layer.

Table X

Toughness of Heat Treated Samples of H-85-Th

<u>Sample #</u>	<u>K<sub>IC</sub>,<sup>1/2</sup> MPam</u>	<u>H GPa</u>	<u>Grain size microns</u>	<u>Grain<sup>*</sup> size dist.</u>	<u>Surface<sup>+</sup> finish</u>	<u>Comments<sup>@</sup></u>
Th 1 a	1.9	10.9	.3	m	3	as hped; X-ray confirmed
b	~2.0	~11	.3	m	35	T-ZrO <sub>2</sub> on 3 μm surface
Th 11 a	1.9	10.7	.4-.5	m	3	5 hr
b	1.8	9.4	.4-.5	m	35	
Th 6 a	1.9	10.2	.5-.6	m	3	10 hr
b	~2.0	~10	.5-.6	m	35	
Th 40		see text		n to w	35	§35 micron then 5 hr 1600°C CO 35 micron then 5 hr 1600°C CO then 35 micron
Th 14	~2.0	~10.0	-	-	3	12.5 hr
Th 15 a	~2.0	~10	.6	m	3	15 hr
b	1.8	9.6	.6	m	35	
Th 16	~2.0	~10	-	-	3	17.5 hr
Th 2 a	1.9	10.2	.8	m	3	20 hr; X-ray confirmed
b	2.0	9.4	.8	m	35	T-ZrO <sub>2</sub> on 3μm surface
Th 12	~2.0	~10	-	-	35 <sup>=</sup>	¢20 hr C-T furnace, ZrC on surface. No T-ZrO <sub>2</sub> observed by X-ray



TABLE X

Parent Sample H-85-Th (cont'd.)

<u>Sample #</u>	<u><math>K_{IC}</math>, MPam<sup>1/2</sup></u>	<u>H, GPa</u>	<u>Grain size, microns</u>	<u>Grain<sup>*</sup> size dist.</u>	<u>Surface<sup>+</sup> finish</u>	<u>Comments</u>
Th 13	~2.0	~10	-	-	3	20hr + oxi- dized at 1230°C 2 hr
Th 7	1.7	10.1	1.0	m	3	30 hrs
Th 8	1.9	10.1	-	-	3	43 hrs 2 heatings
Th 5	1.4	9.9	-	-	3	43 hr 1 heating
Th 4	<1.1	8.4	1-1.5	m to W	3	65 hrs 2 heatings No T-ZrO <sub>2</sub> observed by X-ray

\* Grain size distribution n=narrow, m-medium, w=wide, see text and figures in Sections III and IV.

+ maximum grit size used in grinding/polishing in microns 35 microns was used in an attempt to induce surface compressive layers.

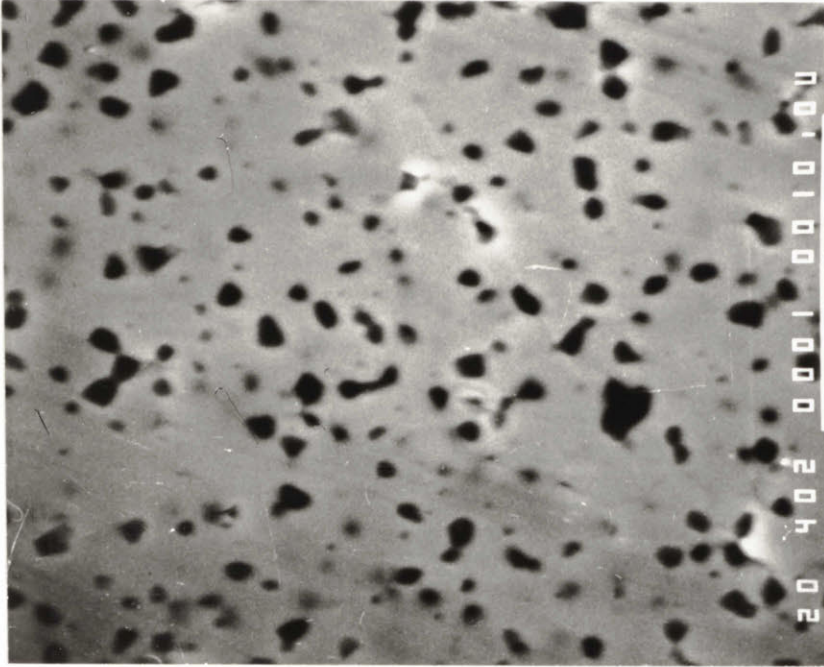
@ annealing time at 1600°C in CO-ZrO<sub>2</sub>+C buffered, single heating and cooling unless otherwise noted.

§ See section IVE-Speculation, for reasoning behind this grinding heat treatment.

ç Surface ground before  $K_{IC}$  test.

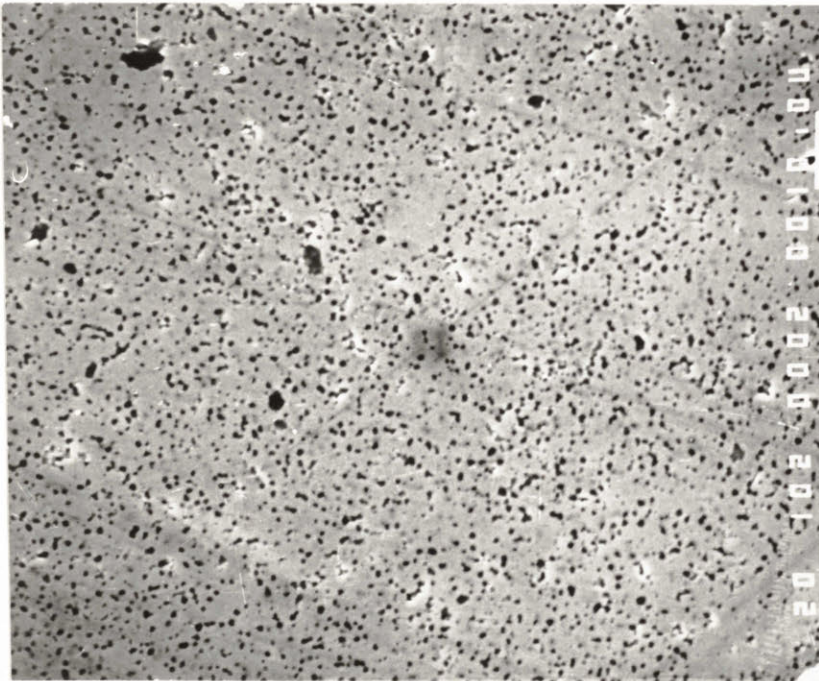
= Grinding not intended to produce compressive layer, intended to remove ZrC on surface.

A.



3 μm

B.



10 μm

Figure IV 10 Medium  $ZrO_2$  grain size distribution is annealed  $ThO_2$ -15 m/o  $ZrO_2$ . Single 10 hr. anneal in  $ZrO_2$ -C buffered CO at  $1600^\circ C$ . Sample H-85-Th 6.

Table XI

Semiquantitative Impurity Analysis (PPM)

	$K_{IC} \text{MPAm}^{1/2}$	Ag	Al	Ca	Cu	Fe	Mg	Si
H-85-B1	2.5	<1	--	1-10	1-10	--	<1	1-10
H-85-B10	3.1	1-10	--	1-10	1-10	--	--	1-10
H-85-D2	2.6	--	--	1-10	1-10	10-100	<1	1-10
H-85-H14	2.9	--	10-100	1-10	1-10	1-10	--	1-10
H-85-I1	2.0	--	--	1-10	1-10	--	--	1-10
H-85-Th1	1.9	--	1-10	10-100	--	--	1-10	1-10
H-85-Th2	1.9	--	1-10	1-10	1-10	1-10	1-10	1-10
H-70-Th1	3.1	1-10	1-10	10-100	1-10	1-10	1-10	1-10

No Hf observed above detection limit of .1-.2%.

All samples contained Th and Zr at greater than 10%.

Silver probably from silver paint used for SEM examination.

Iron in H-85-D2 observable as brown spots in oxidized material.



could explain the low fracture toughness of H-85-Th was found. T-ZrO<sub>2</sub> detected by X-ray diffraction was present in several samples that had low toughness (Table X).

Several samples from parent sample H-85-Th had a varying spatial distribution of the ZrO<sub>2</sub> grain size distribution (Fig. III.9 a & b, sample H-85-Th-40). In a few areas where the ZrO<sub>2</sub> grain size/spatial distribution is particularly narrow, the  $K_{IC}=1.5 \text{ MPam}^{1/2}$ , Fig. IV.11. Where the ZrO<sub>2</sub> grain size distribution was wider  $K_{IC}=2.0 \text{ MPam}^{1/2}$  as in Fig. IV.12. This is a typical distribution for H-85-Th samples whose  $K_{IC}$  data appear on Fig. IV.9, Where the ZrO<sub>2</sub> grain size/spatial distribution was wide to bimodal,  $K_{IC}>3 \text{ MPam}^{1/2}$ , Fig. IV.13. This was the result for a 1.5 cm x 0.7 cm surface of a single 0.5 cm thick sample. In areas where the spatial distribution of the grain size distribution varied abruptly, so did the  $K_{IC}$ , Fig. III.9. The crack lengths on the uniform side of the indent are large, but the crack length on the bimodal ZrO<sub>2</sub> spatial distribution side is small.

The available data produces the division of  $K_{IC}$  vs average ZrO<sub>2</sub> grain size into the classes seen in Fig. IV.14. The ZrO<sub>2</sub> grain size/spatial distribution is a major factor in determining the measured fracture toughness for dense ThO<sub>2</sub>-15 m/o ZrO<sub>2</sub>. Grinding and polishing methods used prior to annealing and/or  $K_{IC}$  testing also play an important role. If ThO<sub>2</sub>-15 m/o ZrO<sub>2</sub> alloys with "medium" grain size distributions are not rough ground prior to polishing, then  $K_{IC}$  vs ZrO<sub>2</sub> grain size simply decreases over ~0.3 to 1.0 micron grain size range.

Information that indicates  $K_{IC}$  measurement by optical microscopy in the early stages of the program are accurate is contained in



Figure IV 11 Narrow ZrO<sub>2</sub> grain size distribution in ThO<sub>2</sub>-15 m/o ZrO<sub>2</sub>, sample H-85-Th 40.  $K_{IC} = 1.5 \text{ MPam}^{1/2}$  @ 1 Kg.

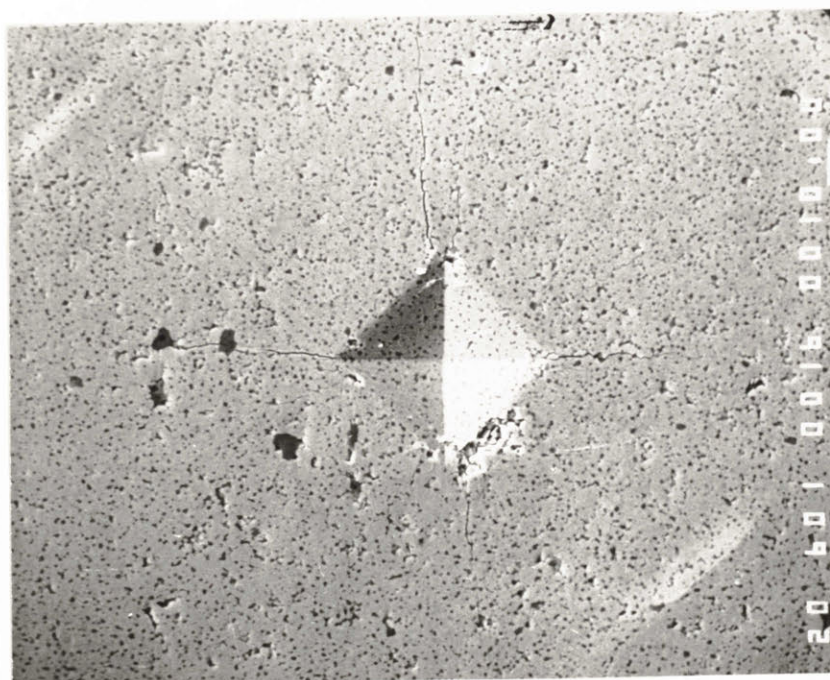
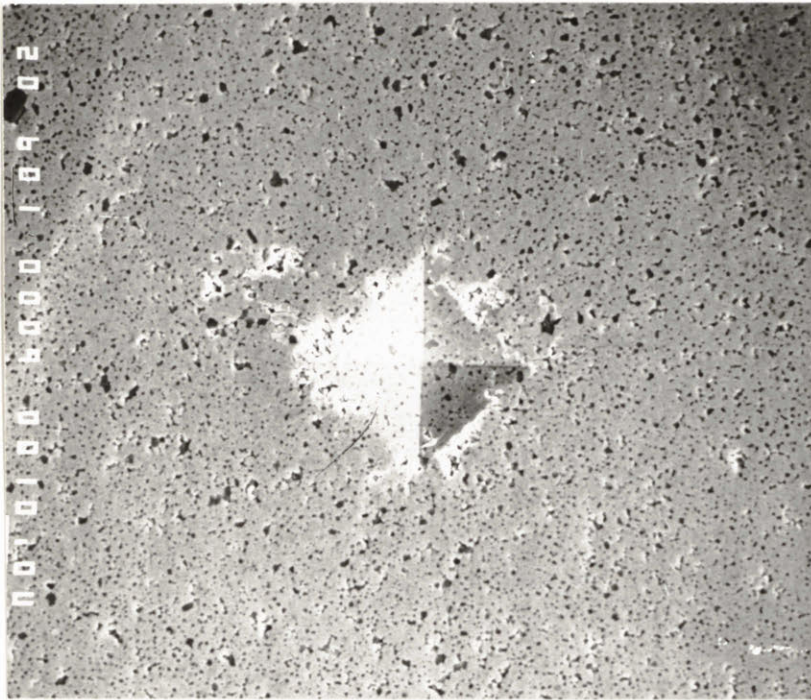


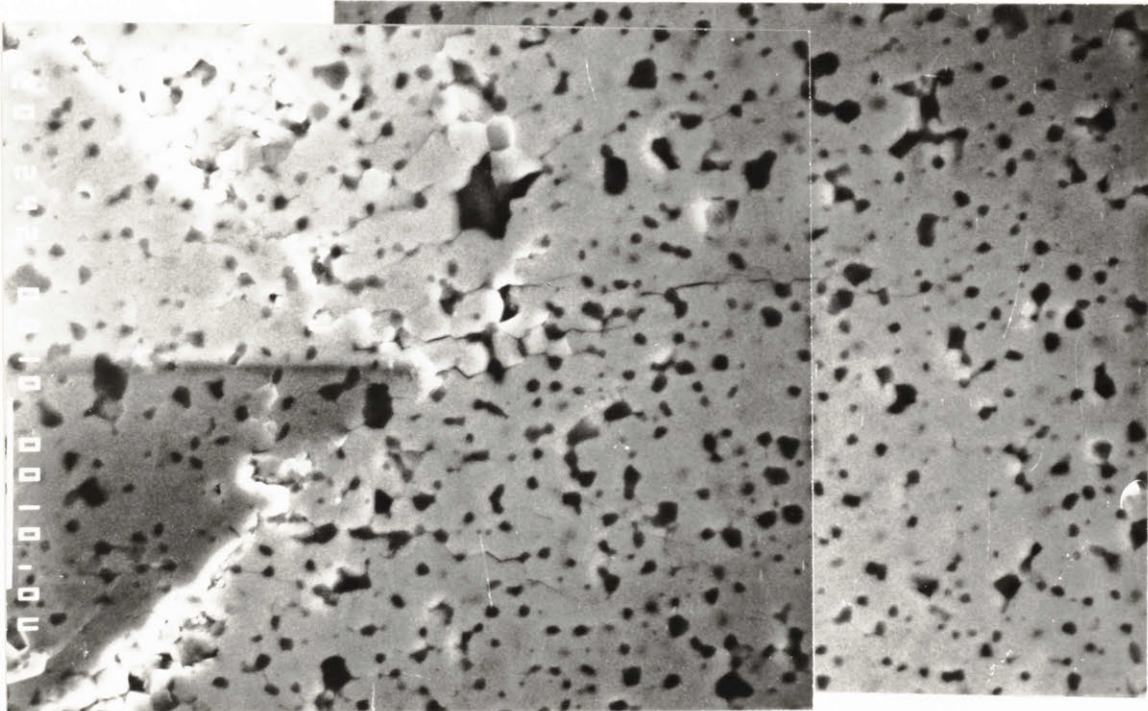
Figure IV 12 Medium ZrO<sub>2</sub> grain size distribution in ThO<sub>2</sub>-15 m/o ZrO<sub>2</sub>, sample H-85-Th 40.  $K_{IC} = 2.0 \text{ MPam}^{1/2}$  @ 1 Kg. This is a typical distribution for most H-85-Th samples.



A.



20µm



B.

5µm

Figure IV 13 Wide  $ZrO_2$  grain size/spatial distribution in  $ThO_2$ -15 m/o  $ZrO_2$ , sample H-85-Th 40.  $K_{IC} \sim 3.0 MPam^{1/2}$  @ 1 Kg. Entire indent A, right corner B.



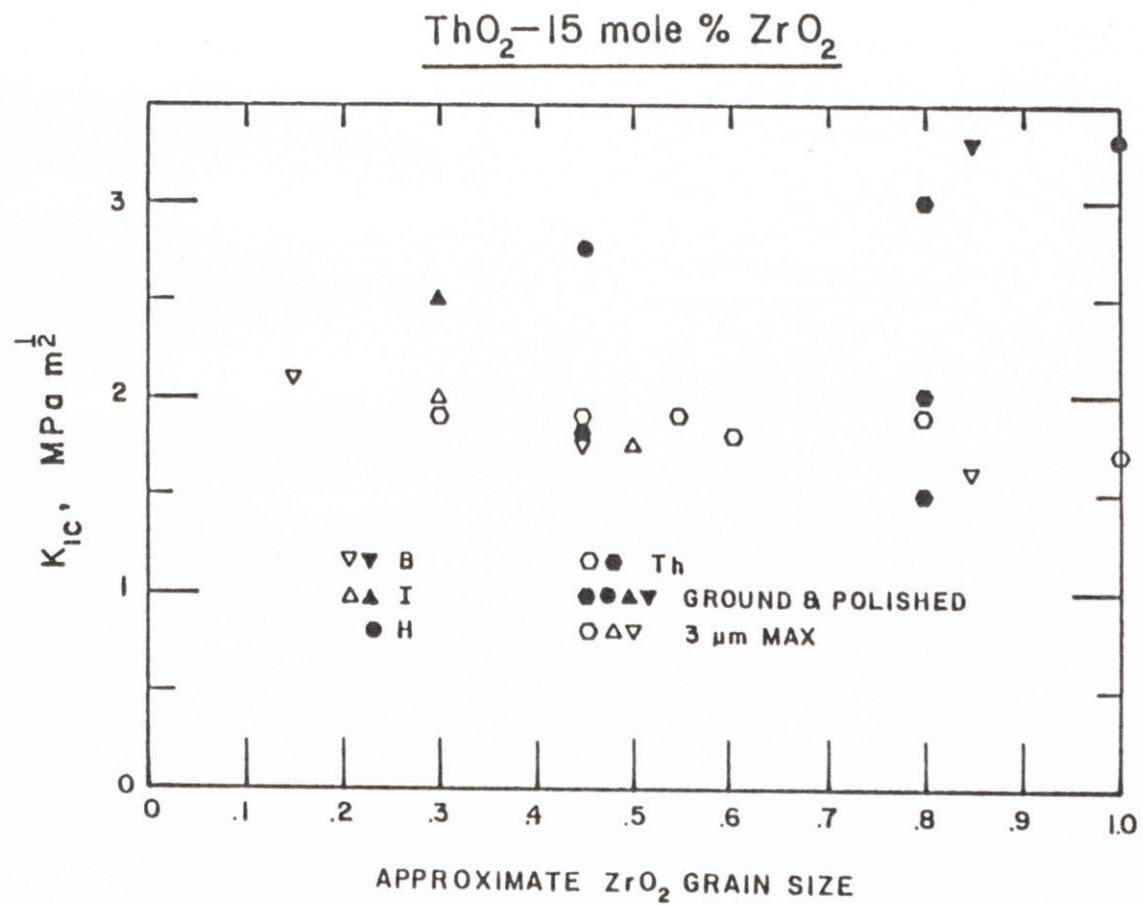
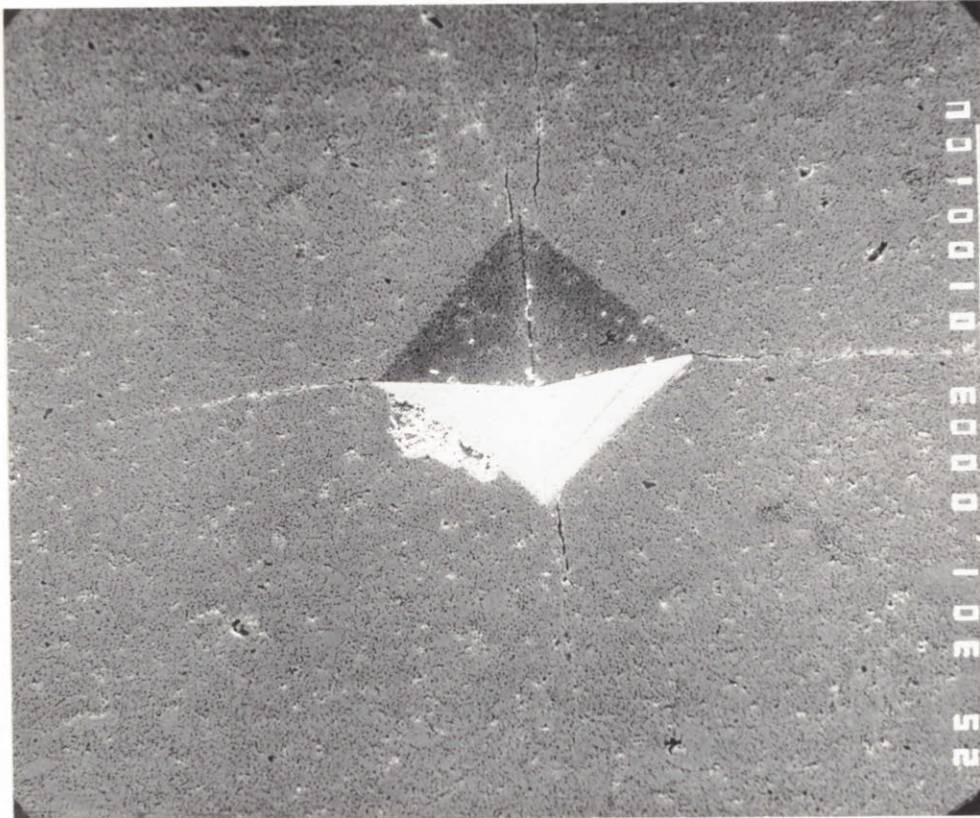


Figure IV 14 Fracture toughness vs. approximate ZrO<sub>2</sub> grain size for ThO<sub>2</sub>-15 m/o ZrO<sub>2</sub>. Accuracy of  $K_{IC}$   $\sim \pm 0.15$  MPa m<sup>1/2</sup>, accuracy of ZrO<sub>2</sub> grain size  $\sim \pm 0.1$  micron.

Table IX and Fig. IV.15. The  $K_{IC}$ 's calculated from optical measurements of H-85-B9 were  $3.6 \text{ MPam}^{1/2}$  at 2 kg and  $3.4 \text{ MPam}^{1/2}$  at 6 kg. By measuring the diagonal length and crack lengths from Fig. IV.15 (taken within six months of the optical measurement) a  $K_{IC}=3.3 \text{ MPam}^{1/2}$  at 6 kg is calculated, Table IX. Evidently, the measurements from early in the project are accurate.

Two 15 m/o  $\text{ZrO}_2$  samples, H-85-B10 and H-85-D2, that had high measured fracture toughness early in the program had lower fracture toughnesses when measured 2 years later, Table IX. H-85-D2 was oxidized 2 years ago; the surface was reground and polished before the second measurement. The surface of H-85-B10 was probably ground and polished before the first measurement, and was not repolished for the second. As the data from early measurements appears reliable, these differences in  $K_{IC}$  may be related to slightly different surfaces being measured, or to degradation due to slow crack growth. Most of sample H-85-D2 had undergone microcracking, Fig. IV-2, but H-85-B10 has not evidently changed.

A sample (H-85-H4) which after hot pressing and oxidation at  $1220^\circ\text{C}$  for 3.5 hours in air was annealed at  $1600^\circ\text{C}$  in a reducing atmosphere had a lower peak  $K_{IC}$  ( $2.5 \text{ MPam}^{1/2}$ ) that occurred at a smaller grain size than other H-85-H samples Table IX. TEM foils of this sample had many microcracks but fine  $\text{ZrO}_2$  grains, less than 0.4 micron, that were largely transformed. The density was 9.26 g/cc,  $\sim 97.7\%$  after the last anneal. This suggests that the porosity produced by the  $1220^\circ\text{C}$  oxidation produces flaws which act as crack nuclei when the T- $\text{ZrO}_2$  transforms and that the  $1600^\circ\text{C}$  anneal did not close these flaws or cracks.



50  $\mu\text{m}$

Figure IV 15 Indent in  $\text{ThO}_2$ -15 m/o  $\text{ZrO}_2$ , sample H-85-B9.  $K_{IC} = 3.3$   
 $\text{MPam}^{1/2}$  @ 6 Kg.



High gas pressure in the pores may assist the T-ZrO<sub>2</sub>→M-ZrO<sub>2</sub> transformation, contributing to this phenomenon. Alternatively, perhaps the high gas pressure in the pores may crack the ceramic along the grain boundaries during thermal cycling from the oxidation temperature to room temperature and back to 1600°C independent of the T→M or M→T ZrO<sub>2</sub> transformations.

#### IV.C.3 Grain Size and Phase Transformation

SEM and TEM observations on ThO<sub>2</sub> + 15 m/o ZrO<sub>2</sub> showed that underaged materials with low K<sub>IC</sub> have fine (less than 0.5 micron) ZrO<sub>2</sub> and ThO<sub>2</sub> grains and that the ZrO<sub>2</sub> is largely tetragonal. The microstructures for several samples indicate that K<sub>IC</sub> of >3MPam<sup>1/2</sup> can be obtained with ZrO<sub>2</sub> particles of about 0.5 to 1 micron with 15 m/o ZrO<sub>2</sub>.

From the limited work with higher ZrO<sub>2</sub> contents, two things are clear. With 0.1-0.3 micron ZrO<sub>2</sub> the toughness is higher with 30-46 m/o ZrO<sub>2</sub> than with 15 m/o ZrO<sub>2</sub>. Further, the results of a few annealings indicate these materials are overaged when the average ZrO<sub>2</sub> size is somewhere near 0.3-0.4 micron, which is much smaller than the size for peak toughness in 15 m/o ZrO<sub>2</sub>. The maximum toughness is unknown but K<sub>IC</sub> 3-4MPam<sup>1/2</sup> with d ~ 0.3 micron is achievable.

The typical hardness values for small grain sized (0.1-0.3 micron) 15 m/o ZrO<sub>2</sub> materials were ~11 GPa. As grain size increased, H~10 GPa and at ~0.8 micron H~9 to 10 GPa. Overaged materials had lower microhardness values and usually could be qualitatively evaluated from the polishing behavior. Overaged materials were easily ground (i.e., soft) but difficult to polish to a low surface roughness due to pull-out problems. TEM observations on some larger grain sized

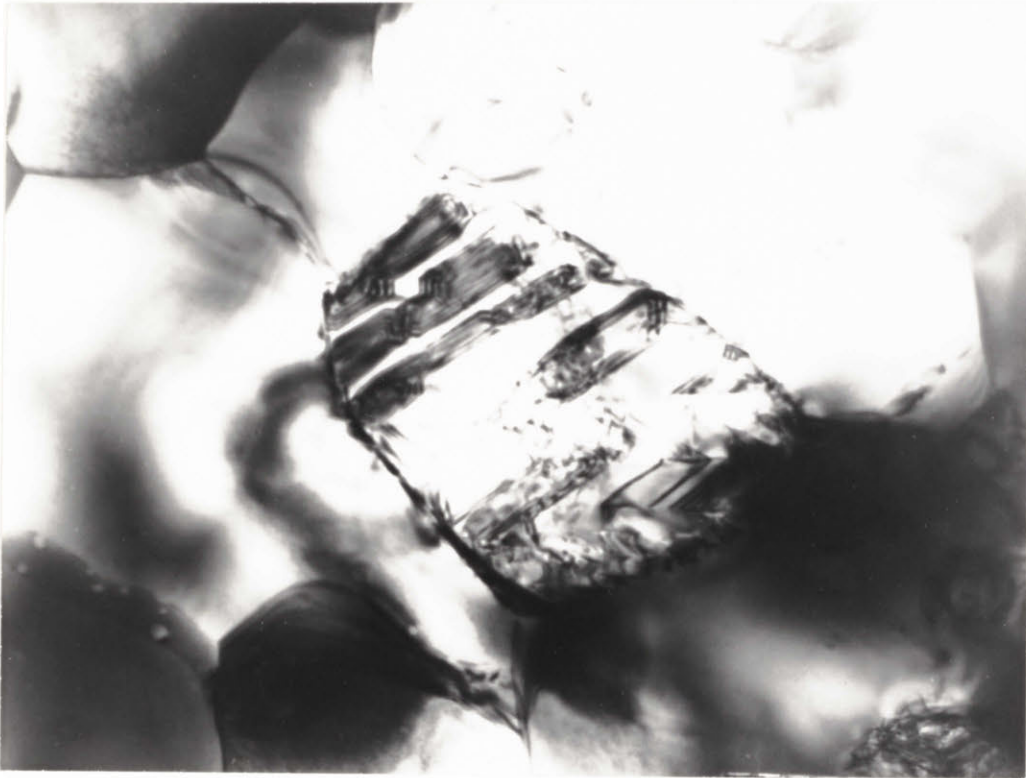
15 m/o  $ZrO_2$  materials revealed extensively transformed  $ZrO_2$ , and appreciable microcracking, similar to Fig. IV.2. The ratio of T:M content when the toughness was high was not determined.

Extremely few dislocations were observed in TEM foils of fine (0.5 micron)  $ZrO_2$  grain size material. Foils made from H-85-F had a high dislocation density in grains that were untwinned (probably  $ThO_2$  grains). Foils made from regions H-85-D2 which had microcracked also had dislocations in untwinned grains but the density was not as high as in H-85-F, Figure IV.2.

#### IV.D. Discussion

T- $ZrO_2$  can exist in  $ThO_2$ - $ZrO_2$  alloys when the  $ZrO_2$  grain size is 0.1 to 0.3 micron. In  $ThO_2$ -15 m/o  $ZrO_2$  this was confirmed by TEM and X-ray diffraction. The toughness of  $ThO_2$ - $ZrO_2$  alloys at  $ZrO_2$  grain sizes of 0.1-0.3 micron increases with  $ZrO_2$  content from  $1.5 \text{ MPam}^{1/2}$  to  $>3 \text{ MPam}^{1/2}$  over the 5 m/o to 46 m/o  $ZrO_2$  range. For some 15 m/o  $ZrO_2$  samples the toughness can increase to a peak and then decrease over the 0.3 to 1 micron  $ZrO_2$  grain size range.

The propensity for microcracking and macroscopic failure depends critically on the detailed microstructure. Well distributed pores (as small as  $500 \text{ \AA}$ ) with high pressure gas in them in nearly dense materials can contribute to microcracking.  $ZrO_2$  grains as large as 1.5 microns in dense materials can transform in the presence of pores and not microcrack (Figure IV.16). Slow crack growth can occur in internally stressed  $ThO_2$ - $ZrO_2$  bodies and other ceramics (Dole et al., 1978b). Dense bodies of 15 m%  $ZrO_2$  macroscopically fail when the average  $ZrO_2$  grain size is 1-2 microns. Dense bodies of 46 m%  $ZrO_2$  macroscopically



—  
0.5  $\mu\text{m}$

Figure IV 16 Large M-ZrO<sub>2</sub> in TEM foil without apparent microcracking, sample H-85-D2. TEM foil and picture by J. Schneibel.



pically fail when the average  $ZrO_2$  grain size is about 0.3 micron. At slightly smaller  $ZrO_2$  grain sizes, indentions in 46 m%  $ZrO_2$  produce cracks that propagate across the sample.

Bodies containing 3-7% porosity do not macroscopically fail when the  $ZrO_2$  grain size distribution varies from 1 to 5 microns. A 7% porous body with  $ZrO_2$  grain sizes of 1-5 microns did not fail even when it contained continuous regions of  $ZrO_2$  greater than 100 microns. Microcracks appear on as sintered surfaces but evidently do not proceed to macroscopic fracture because of the porosity in the 1 micron size range.

The majority of  $K_{IC}$  measurements were made on reduced non-stoichiometric  $ZrO_2$ . Carniglia et al. showed that non-stoichiometry does not affect the T→M transformation temperature. The carbon contained in the unoxidized samples did not inhibit the T→M transformation as numerous unoxidized samples exhibited high toughness.

Grinding and polishing vs. polishing with 3 micron diamond or less, is important in producing high  $K_{IC}$ 's. Grinding seems to produce a compressive surface layer. This is supported by some observations by Schneibel during preparation of TEM foils. As he prepared samples of  $ThO_2-ZrO_2$  he often observed buckling in thin 100 micron thick disks. Both surfaces of the buckled disk had been ground by 20 micron SiC; buckling occurred when one side of the sample was then polished with a finer grit size (less than 6 microns). This phenomenon was useful because the disk could then be inverted and the central section thinned with the finer grit sizes. This operation left a thicker section on the exterior of the foil.

Microcrack toughening is occurring in porous 3-7% materials with large  $ZrO_2$  grains and wide size distributions (apparently the sintered materials were substantially transformed after cooling). Cracks emanating from indent sides, the multiple cracks from corners and massive crack branching are good evidence for microcracking, Fig. IV.8. Dense materials with wide  $ZrO_2$  grain size distributions also appear to have a substantial contribution to toughening from microcracking, these materials also have much multiple cracking near indent corners, Fig. IV.13. Indentations in dense materials with high toughness but no intentional surface stress do not show these microcracking features. Only one or two cracks emanate from indent corners, massive branching does not occur and the cracks are straight and regular. Transformation in TEM foils can occur without microcracking, Figure IV.16, and probably no microcracking in the bulk is necessary for transformation. In dense, medium grain size distribution  $ThO_2$ - $ZrO_2$  alloys transformation toughening may be the dominant toughening mechanism. The highest toughnesses measured on as-annealed surfaces of 15, 30, and 46%  $ZrO_2$  materials, Fig. IV.6, indicate the toughening which can result from this. The higher toughness measured in some rough ground specimens may be due largely to a compressive surface layer.

A compressive surface layer results only if T→M transformation occurs. If any factor can limit the transformation during both grinding and crack propagation, then no increase in  $K_{IC}$  will result; H-85-Th 40 with a fine grain size distribution (Figure IV.11) may be an example of this. A scarcity of nuclei would seem to be the most likely factor inhibiting transformation under these conditions. If so, grinding

damage or the high stress fields near large  $M\text{-ZrO}_2$  particles may assist nucleation of additional  $M\text{-ZrO}_2$  or microcracking at crack tips during indentation testing. What atomic structures or defects act as nuclei are not known.

There must be a scarcity of microcrack nuclei in order for transformed particles to not cause local microcracking in dense material. This may explain why large grained, dense materials do not show toughening and are susceptible to macroscopic failure by slow growth of isolated cracks.

The T $\rightarrow$ M transformation of fine grain size  $ZrO_2$  in  $ThO_2$  appears to be nucleation controlled. Thermodynamic arguments simply cannot predict the T $\rightarrow$ M $\rightarrow$ T temperature hysteresis typically reported for polycrystalline  $ZrO_2$  or the "critical"  $ZrO_2$  grain sizes for transformation observed in different matrices. Further, intragranular  $ZrO_2$  particles in  $Al_2O_3$  grains do not have a "critical" particle size for transformation. The best evidence for nucleation control in this study is TEM foils in which most of the  $ZrO_2$  was tetragonal as shown in Figures III.4 and III.13. The TEM foils used varied in thickness from 200 Å to 800 Å. As the T- $ZrO_2$  (phase determined by electron diffraction) were up to 0.3 micron grain size or larger, the diameter to thickness ratio of the T- $ZrO_2$  varied from 3 to 10. When the diameter to thickness ratio is 10 there are smaller dilatational strain energy barriers and much smaller distortional strain energy and interfacial energy barriers for the grain to transform. If thermodynamic conditions were the only constraints, the grain could buckle and twin out of the foil plane reducing the strain energy barrier further. No special treatment



except careful thinning is needed to produce  $\text{ThO}_2$ -15 m%  $\text{ZrO}_2$  foils with T- $\text{ZrO}_2$  maintained in them. Microcracking was not necessary for the transformation to occur in foils, as shown in Figure IV.16. Microcracking is probably not necessary for transformation in the bulk. The lack of much toughening under any combination of grain size, grinding or oxidation for samples from H-85-Th that had narrow or medium grain size distributions and lack of toughening for H-85-B and H-85-I that were not ground is also evidence supporting nucleation arguments. This poses the question, "Why did such lack of toughening behavior occur in  $\text{ThO}_2$ - $\text{ZrO}_2$  that has not been observed in other materials?" For T- $\text{ZrO}_2$  dispersed as a second phase in a dissimilar oxide (type 3 microstructures)  $\text{ThO}_2$  has the best matched thermal expansion coefficients. For  $\text{ThO}_2$ ,  $\alpha = 10.7 \times 10^{-6} (\text{°C})^{-1}$  (Lang and Kundson, Ohnystand and Rose, Wachtman et al.); for tetragonal  $\text{ZrO}_2$ ,  $\alpha \approx 12.6 \times 10^{-6} (\text{°C})^{-1}$ ,  $\alpha_c \approx 14.3 \times 10^{-6} (\text{°C})^{-1}$  (Lang 1964), with both measurements for 1200°C to 2000°C. Elastic moduli are close as well, for  $\text{ThO}_2$ ,  $E \approx 240$  GPa (Lang and Knudson) and for  $\text{ZrO}_2$ ,  $E \approx 220$  GPa (Garvie et al. 1980).  $\text{Al}_2\text{O}_3$  and mullite matrices place the T- $\text{ZrO}_2$  grains under a large amount of tensile strain due to their smaller thermal expansion coefficients.  $\text{ThO}_2$  may be a better matrix material for T- $\text{ZrO}_2$  than T- $\text{ZrO}_2$  itself due to the anisotropic thermal expansion coefficient of zirconia. If the wide  $\text{ZrO}_2$  grain size/spatial distributions contain aggregates of many T- $\text{ZrO}_2$  grains then high stresses can be produced along T- $\text{ZrO}_2$ -T- $\text{ZrO}_2$  grain boundaries. Alternatively, the T- $\text{ZrO}_2$  grain boundaries may provide nuclei.

#### IV.E. Speculation Regarding Nucleation

Glissile lattice dislocations in  $\text{ThO}_2$  impinging on  $\text{T-ZrO}_2$  may trigger the  $\text{T}\rightarrow\text{M}$  transformation. Lattice dislocations in  $\text{ThO}_2$  that are generated at high temperature, may be glissile at room temperature in the tensile stress field of a crack. Lattice dislocations in both  $\text{ZrO}_2$  and  $\text{ThO}_2$  can be generated and moved by rough grinding at room temperature.

The following reasoning led to the thermo-mechanical treatment given to several samples that was an attempt at increasing the  $\text{M-ZrO}_2$  nucleation probability. It was assumed that lattice dislocations in  $\text{ThO}_2$  that impinged on  $\text{T-ZrO}_2$  would produce  $\text{M-ZrO}_2$ . The reverse  $\text{M}\rightarrow\text{T}$  transformation produces dislocations or faults in  $\text{T-ZrO}_2$  that are not fully eliminated by climbing to the grain boundaries during a short grain growth anneal. The  $\text{T}\rightarrow\text{M}$  transformation occurs upon cooling, nucleated by the dislocations or faults remaining in the  $\text{T-ZrO}_2$ . More dislocations in  $\text{ThO}_2$  are now produced that can be moved by grinding. This triggers more  $\text{T}\rightarrow\text{M}$  transformation at room temperature during grinding and/or during indentation tests leading to a high  $K_{\text{IC}}$ .

This reasoning seems to be incorrect as the  $K_{\text{IC}}$  is low  $1.5 \text{ MPam}^{1/2}$  for a region of fine grain size distribution in one sample that received this thermo-mechanical treatment (Figure IV.11), although the surface layer of high nucleation probability may be thin and too rough grinding after annealing may eliminate the layer.

There is little evidence in this study supporting a lattice dislocation theory of martensite nucleation in  $\text{T-ZrO}_2$ . We observed dislocations in  $\text{ThO}_2$  grains only in samples where there was substantial  $\text{M-ZrO}_2$ . The dislocations probably are generated when the  $\text{T}\rightarrow\text{M}$  transformation occurs

at high temperatures ( $>600^{\circ}\text{C}$  ?). Less than five dislocations were seen in pictures from foils that contained greater than five hundred T-ZrO<sub>2</sub> grains.

Al<sub>2</sub>O<sub>3</sub>-ZrO<sub>2</sub> is extremely tough yet it is improbable that extensive lattice dislocation motion occurs in the stress field of a propagating tensile crack in this material at room temperature. No lattice dislocations appear in any published TEM picture of Al<sub>2</sub>O<sub>3</sub>-ZrO<sub>2</sub> (due to the repeated annealing necessary to obtain T-ZrO<sub>2</sub> in foils of this material?) yet the T-ZrO<sub>2</sub> does transform in the foil. In ThO<sub>2</sub>-ZrO<sub>2</sub> the grain size/spatial distribution seems to be extremely important, evidently due to the large anisotropy in thermal expansion coefficient in T-ZrO<sub>2</sub>. If thermal expansion mismatch is the most important factor for determining the reliability of nucleation of M-ZrO<sub>2</sub> then UO<sub>2</sub> as a matrix material may show grain size/spatial distribution effects similar to ThO<sub>2</sub>.

If lattice dislocations are not nucleation sites then what are? Perhaps grain boundaries or extrinsic defects (dislocations?) in grain boundaries are nucleation sites. If nucleation sites are on grain boundaries then in fine grain size T-ZrO<sub>2</sub> (type 2 microstructures) should the grain size matter? Perhaps the anisotropic thermal expansion coefficient of T-ZrO<sub>2</sub> produces the grain size effect. Stresses along the grain boundaries will depend on grain size, fabrication temperature and cooling rate. At least some second phase oxide is alloyed in the microstructure to reduce the  $-\Delta G_{\text{O}}$ . How does this "stabilizing" oxide alter the thermal expansion coefficients? Can defect clusters act as nuclei? How do defect clusters, long or short range order, effect  $-\Delta G_{\text{O}}$  or the Peierls stress barrier? Some slim evidence exists that minor impurities can hinder the M→T transformation (Fehrenbacher and Jacobson).



The energy of a faulted region serving as a nucleus of  $M\text{-ZrO}_2$  in  $T\text{-ZrO}_2$  can be written as (Olsen and Cohen)

$$\Gamma = t\rho [\Delta G + \Delta U] + 2\gamma_{\text{Interface}}$$

where  $\Gamma$  is the nucleus energy per unit area,  $\rho$  is the molar density,  $t$  the stacking fault thickness,  $\Delta G$  the free energy of transformation  $\Delta U$  the change in strain energy and  $\gamma_{\text{Interface}}$  the interface energy. If we assume  $\Delta G_{M \rightarrow T} \sim 5.94 \times 10^3 \text{ J/mole} - 4.02 \text{ J/mole } ^\circ\text{K}$  (Coughlin and King) and  $t \sim 5 \text{ \AA}$ ,  $T = 950^\circ\text{C}$ ,  $G \sim 100 \text{ GPa}$ , and  $\Delta U \sim \frac{G}{2} R \ln \frac{R}{5\text{\AA}} \left\{ \frac{[\text{expansion } \perp \cdot 5\text{\AA}]^2}{(1-\nu)} \right\}$  (Hull) by approximating the strain energy by a small dislocation loop of radius  $R$  and Burgers vector (expansion  $\perp \cdot 5 \text{ \AA}$ ), perpendicular to the nucleus; and if  $\gamma_{\text{I}} \sim \frac{RG}{2} [(\text{expansion } \parallel \cdot 5 \text{ \AA})^2 (1 + \frac{1}{1-\nu})]$  by approximating the interface energy as 2x (for core energy) the strain energy of a small dislocation loop with Burgers vector parallel to the nucleus.

If the expansion  $\perp = 2.1\%$  and the expansion  $\parallel = 1.44\%$  and  $R = 5 \text{ \AA}$  then

$$\begin{aligned} \Gamma &= 5 \times 10^{-10} \text{ m} [-1.03 \times 10^3 \text{ J/mole} + 6.2 \times 10^2 \text{ JK/mole}] 4.76 \times 10^4 \text{ mole/m}^3 \\ &+ 5 \times 10^{-10} \text{ m} [1.01 \times 10^3 \text{ J/mole}] 4.76 \times 10^4 \text{ mole/m}^3 \sim 1.48 \times 10^{-2} \text{ J/m}^2 \end{aligned}$$

The nucleus energy is positive which indicates that a single dislocation is not a good nucleation site at  $950^\circ\text{C}$ . Using the same approximations at  $0^\circ\text{C}$

$$\begin{aligned} \Gamma &\sim 5 \times 10^{-10} \text{ m} [-4.84 \times 10^3 \text{ J/mole} + 6.2 \times 10^2 \text{ J/mole}] 4.76 \times 10^4 \text{ mole/m}^3 \\ &\sim -7.64 \times 10^{-2} \text{ J/m}^2 \end{aligned}$$

The nucleus energy is negative. The energy balance is extremely sensitive to the assumptions regarding strain energy and interface energy,

unfortunately. Thus, depending upon the values used for volume expansion and shear strains (neglected in the calculation) upon transformation and thermal expansion coefficients for T-ZrO<sub>2</sub>, M-ZrO<sub>2</sub> and the matrix material, different signs for nucleus energy can be obtained for a given temperature. Once an energy for a nucleus becomes zero additional energy is needed to drive the partial dislocations through the Peierls stress barrier.

#### IV.F. CONCLUSIONS

1. Tetragonal zirconia can exist in  $\text{ThO}_2\text{-ZrO}_2$  alloys when the zirconia grain size is 0.1 to 0.3 micron.
2.  $\text{ThO}_2\text{-15 m/o to 46 m/o ZrO}_2$  alloys can have  $K_{IC}$ 's  $> 2X$  above dense  $\text{ThO}_2$  of similar grain sizes. At  $\text{ZrO}_2$  grain sizes of  $\sim 0.1\text{-}0.3$  micron the toughness of dense  $\text{ThO}_2\text{-ZrO}_2$  alloys increases from  $\sim 1.5 \text{ MPam}^{1/2}$  for 5 m/o  $\text{ZrO}_2$  to  $>3 \text{ MPam}^{1/2}$  for 46 m/o  $\text{ZrO}_2$ .
3. The toughness of  $\text{ThO}_2\text{-15 m/o ZrO}_2$  can rise to a peak and then decrease over the 0.3 to 1.0 micron  $\text{ZrO}_2$  grain size range. Dense  $\text{ThO}_2\text{-ZrO}_2$  alloys with higher  $\text{ZrO}_2$  contents, may have similar behavior, but were not made at small enough  $\text{ZrO}_2$  grain sizes to have low  $K_{IC}$ .
4. At large  $\text{ZrO}_2$  grain sizes dense  $\text{ThO}_2\text{-ZrO}_2$  alloys macroscopically fail; the critical  $\text{ZrO}_2$  sizes are 1-2 micron for 15 m/o  $\text{ZrO}_2$  and 0.3 micron grain sizes for 30 m/o to 46 m/o  $\text{ZrO}_2$ .  $\text{ZrO}_2$  bearing ceramic alloys with significant internal stresses can fail by slow crack growth without externally applied stresses.
5. Macroscopic failure and microcracking in  $\text{ThO}_2\text{-ZrO}_2$  depend on the detailed microstructure;  $\text{ZrO}_2$  content,  $\text{ZrO}_2$  grain size, the amount of porosity (0-10%), pore size (500 Å to 10 microns), and distribution of porosity, are important. Fully dense materials  $>99\%$  have a smaller propensity to microcrack than dense materials ( $\sim 98\%$ ) with small amounts of well distributed fine porosity, all other variables being constant. Dense materials with wide  $\text{ZrO}_2$  grain size distributions seem to microcrack easily. Porous materials ( $\sim 95\%$  dense) microcrack easily but do not fail macroscopically.



6. In  $\text{ThO}_2$ -15 m/o  $\text{ZrO}_2$  the  $\text{ZrO}_2$  grain size, the  $\text{ZrO}_2$  grain size distribution and compressive surface layers control the magnitude of the measured  $K_{IC}$ 's. Alloys with higher  $\text{ZrO}_2$  contents seem to have similar behavior.
7. Microcrack toughening does occur in porous  $\text{ThO}_2$ - $\text{ZrO}_2$  alloys and some transformation toughening can occur in dense  $\text{ThO}_2$ - $\text{ZrO}_2$  alloys.
8. The T- $\text{ZrO}_2 \rightarrow \text{M} - \text{ZrO}_2$  transformation can occur in TEM foils of  $\text{ThO}_2$  - 15 m/o  $\text{ZrO}_2$  alloys without microcracking. The T $\rightarrow$ M transformation probably can occur in the bulk without microcracking.
9. The T- $\text{ZrO}_2 \rightarrow \text{M} - \text{ZrO}_2$  transformation seems to be nucleation controlled and may not always occur near a propagating crack. If T $\rightarrow$ M transformation does occur, microcracking may not be due to the limited porosity. The microcrack nucleation might be necessary because transformation toughening and surface compressive stresses can have limited contributions to toughening in  $\text{ThO}_2$ -15 m/o  $\text{ZrO}_2$  alloys. Thus the fracture toughness of  $\text{ThO}_2$ -15 m/o alloys is also apparently nucleation controlled.

## V. STRESS INTENSITY VARIATION CALCULATION

### V.A. Motivation for Model Development

As mentioned previously, no model for either transformation toughening or microcrack toughening is available using three-dimensional elasticity. Different models for microcrack toughening seem to predict different effects with grain size distribution when applied to  $ZrO_2$  ceramic alloys (Section II.A.). No single model covers a mixture of transformation and microcrack toughening. A combination of the models by Evans et al. (1981a) and Evans and Farber (1981) may be able to cover a combination of microcrack and transformation toughening, as the formalism for both models is similar. This formalism either implicitly or explicitly treats the transformed or microcracked region as homogeneous material having different compliance than the untransformed or microcracked material, but having the same value of  $G_c$  or  $K_c$ . Crack extension events and stresses on a scale local to the microcracks or transforming inclusions are not adequately treated by this formalism; the local crack bowing, out of plane deflection, branching or microcrack link-up events have important effects. As  $K_I$  increases the transformation/microcrack zone size increases. Crack extension terminates this, hence if the crack extension is inadequately treated in a model then erroneously high toughening can be predicted. Local variation of stress intensity along a crack near microcracks of transforming inclusions are mandatory for determining the crack extension condition. For the simpler problem of a varying interval stress field, two-dimensional solutions exist for the effect of  $K$ ; the results predict that the maximum  $\Delta K \propto \sigma_a \sqrt{\lambda}$  where  $\sigma_a$  is the amplitude and  $\lambda$  the wavelength of the interval stress field, Kanazawa et al., Evans et al. (1977).

In three dimensions the crack can bow between or deflect around compressive zones. The problem of crack bow through between impenetrable inclusions has been treated at several degrees of approximation. Lange (1970) predicts a higher toughness at smaller interinclusion spacings, i.e., favors smaller inclusions; Evans (1972) and Green and Nicholson (1978) obtain more complicated functions, with toughness depending primarily on volume fraction of inclusions. The problem of penetration into inclusions with internal compressive stresses or other factors has not been treated in three dimensions.

Thus three-dimensional solutions for the local effects on  $K$  of a crack caused by discrete misfitting or transforming inclusions or micro-cracks is needed. Some three-dimensional fracture mechanics methods were briefly examined (Kassier and Sih, 1975 and Panasyuk et al., 1981), but no fully developed theory for local stresses seemed easily applicable. The model described in the following section treats the local variation of stress intensity along a straight front crack near a single misfitting inclusion using three-dimensional elasticity. Finite element methods were avoided as this method seemed to be fully developed and extremely time consuming for the model envisioned.

Three methods of solution are presented. Numerical calculations were performed by two methods, one using Fourier series and a second method using contour integration plus an intuitive method of solution. The numerical values were calculated for four inclusion positions. Limitations of the second method and the applicability of these results to the above problems are discussed. As the intuitive method of solution (referred to as the limited rapid non-rigorous method, LRNR) has a minimum of calculation the method of solution might be generalized to include other



brittle fracture mechanics problems.

#### V.B. Formulation of $\Delta K_I$ Problem

The model developed was one of three-dimensional elasticity with a planar straight crack interacting with the stress field caused by a spherical inclusion that has expanded in volume by  $\Delta V$ , Figure V.1a. Both the matrix material and the inclusion were assumed to be isotropic, linearly elastic with the same elastic moduli. Because the crack is present, the stress field of an expanding inclusion in an infinite matrix must be modified to eliminate stresses present on the half plane describing the crack surface, Figure V.1b. This then leads to a variation of  $K_I$ ,  $K_{II}$ , and  $K_{III}$  in the Z direction ( $\Delta K_I, II, III$ ) that can be added to the unusual  $K_I, II, III$  derived from external loading. Ignoring  $\Delta K_{II}$  and  $\Delta K_{III}$  for the moment, the normal stress present on a plane, a distance  $y_0$  from the center of an expanding spherical inclusion is

$$\sigma_{yy} = -\frac{2}{9} \frac{Ea^3}{(1-\nu)} \left(\frac{\Delta V}{V}\right) \left[\frac{3}{2} \frac{y_0^2}{R^5} - \frac{1}{2R^3}\right] \quad (V.1)$$

where E is Young's elastic modulus,  $\nu$  is Poissons ratio, a the inclusion radius,  $\Delta V/V$  the normalized volume expansion and R the distance from the center of the inclusion (Sokolnikoff, Sesling, McClintok and Argon).

Combining this with an equation from Kassir and Sih that can describe the variation of  $^*K_I$  along Z when a half plane straight front crack in an infinite body is loaded by a point force of magnitude P,

$$\Delta K_I = \frac{(2)^{1/2}}{(\pi)^{3/2}} \left[\frac{P \gamma^{1/2}}{2 \gamma^2 + (Z+\alpha)^2}\right] \quad (V.2)$$

where  $\gamma, \alpha$  is where the point force is applied.  $\gamma, \alpha$  have senses opposite that of X and Z.

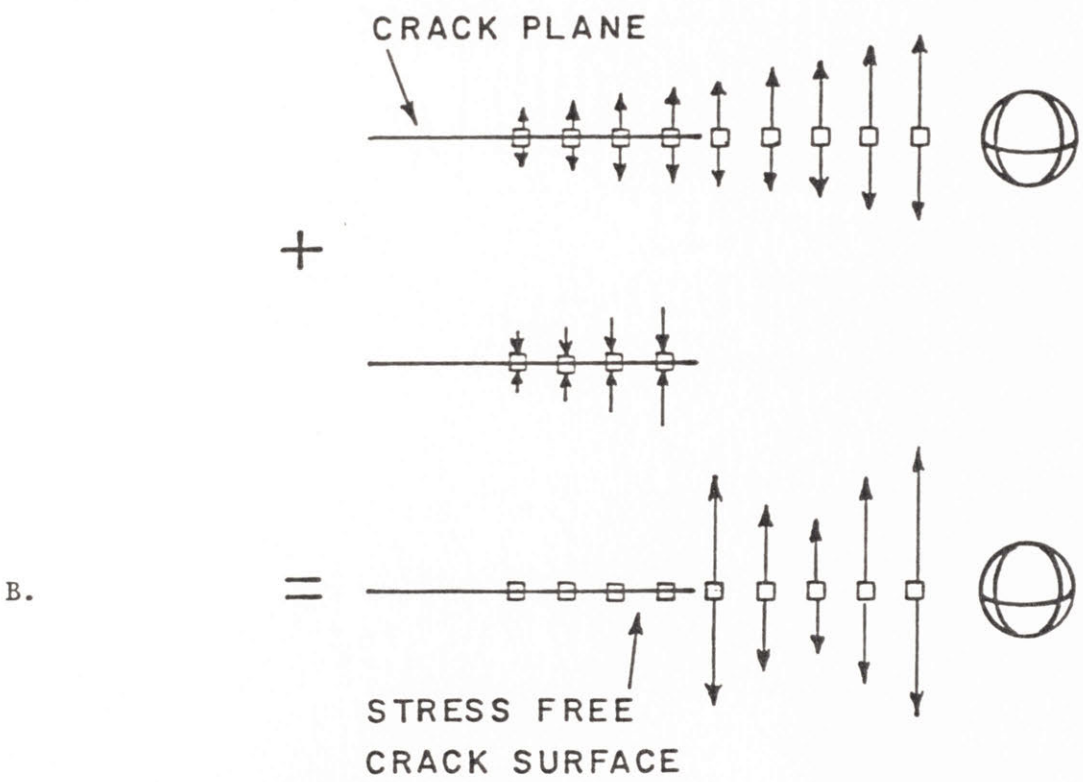
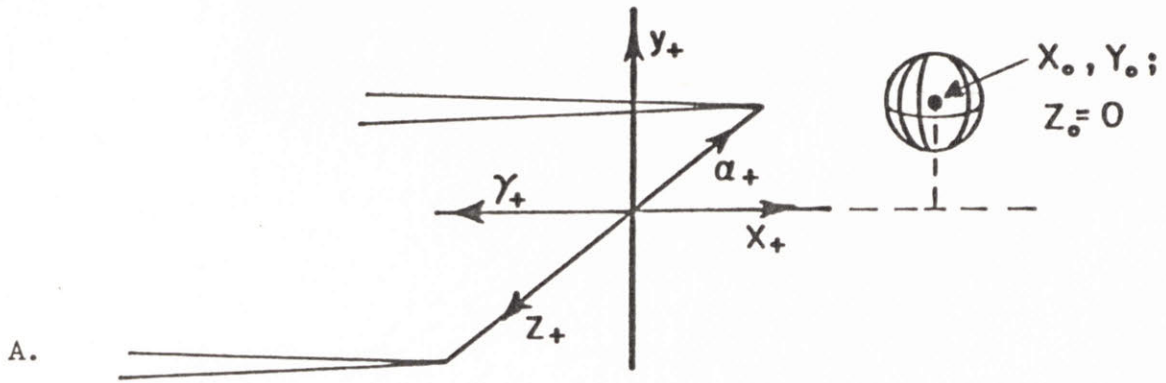


Figure V 1 A. Coordinate orientation and sphere position used for  $\Delta K_I$  calculation.

B. Schematic of stress superposition procedure to obtain stress free crack surface.

Allowing the point force to become a stress distribution  $p(\gamma, \alpha)$ ,

$$\Delta K_I = \frac{(2)^{1/2}}{(\pi)^{3/2}} \int_0^\infty \int_0^\infty \frac{p(\gamma, \alpha) \gamma^{1/2}}{\gamma^2 + (Z + \alpha)^2} d\gamma d\alpha \quad (V.3)$$

and replacing  $p(\gamma, \alpha)$  by  $\sigma_{yy}(\gamma, \alpha)$  from an expanding inclusion at  $x_0, y_0, z_0 = 0$ , Eq. (V.1), to obtain a stress free crack surface where

$$R = [y_0^2 + \alpha^2 + (\gamma + x_0)^2]^{1/2} \quad (V.4)$$

will determine  $\Delta K_I$ .

The combination of Eqs. (V.1), (V.2), and (V.4) using  $y_0, x_0, Z, \gamma$  and  $\alpha$  normalized to  $a$ , produce

$$\Delta K_I = - \left(\frac{2}{\pi}\right)^{3/2} \left(\frac{\Delta V}{V}\right) \frac{E(a)^{1/2}}{9(1-\nu)} \int_0^\infty \int_0^\infty \frac{(\gamma/a)^{1/2}}{(\gamma/a)^2 + (Z/a + \alpha/a)^2} \cdot \left\{ \frac{3y_0^2}{2[y_0/a]^2 + (\alpha/a)^2 + (\gamma/a + x_0/a)^2} \right\}^{5/2} - \frac{1}{2[(y_0/a)^2 + (\alpha/a)^2 + (\gamma/a + x_0/a)^2]^{3/2}} \cdot d\gamma/a d\alpha/a \quad (V.5)$$

Letting  $Z/a + \alpha/a = \zeta/a$  then transforming to polar coordinates simplify this somewhat to

$$K_I = - \left(\frac{2}{\pi}\right)^{3/2} \left(\frac{\Delta V}{V}\right) \frac{E(a)^{1/2}}{9(1-\nu)} \cdot \int_0^\pi (\sin\theta)^{1/2} \cdot \int_0^\infty \frac{3}{2} y_0^2 r^{-1/2} [r^2 + 2r(-Z\cos\theta + x_0\sin\theta) + x_0^2 + y_0^2 + Z^2]^{-5/2} - \frac{1}{2} r^{-1/2} [r^2 + 2r(-Z\cos\theta + x_0\sin\theta) + x_0^2 + y_0^2 + Z^2]^{-3/2} \cdot dr d\theta \quad (V.6)$$

\* Kassir and Sih's  $K_I = K_I(\pi)^{-1/2}$



where normalization to  $a$  is implied by the  $a^{1/2}$  in the constants. Inside the sphere a compressive hydrostatic stress exists of magnitude

$$\left(\frac{\Delta V}{V}\right) \frac{2}{9} \frac{E}{(1-\nu)} \quad (\text{V.7})$$

hence

$$[(x_o/a)^2 + (y_o/a)^2]^{1/2} \geq 1 \quad (\text{V.8})$$

for the stress distribution in Eqs. (V.1), (V.5) and (V.6) to hold.

If the crack penetrates the inclusion, then the stress distribution on the crack surface must be modified.

An iterated superposition method can be used if elastic modulus differences between the matrix and inclusion need to be included. Now the  $\Delta K_I$ , calculated from the volume misfit and the  $K_I$  from external loading produce stresses from the modulus difference. These stresses, when present on the crack surface, must be cancelled. This cancellation now produces a  $\Delta_2 K_I$  which also produces stresses on the crack surface. This iteration scheme can lower or raise the total  $\Delta K_I$  (and  $\Delta K_{II,III}$ ) depending on the sign of the modulus difference and position of the inclusion.

A general formulation of the problem will also include  $K_{II}$  and  $K_{III}$  (Kassir and Sih, 1975)

$$K_I = \frac{2^{1/2}}{\pi^{3/2}} \int_0^\pi \int_0^\infty F_1 \sigma_{yy} \, dr d\theta \quad (V.9a)$$

$$K_{II} = \frac{2^{1/2}}{\pi^{3/2}} \int_0^\pi \int_0^\infty F_1 \tau_{yx} + \frac{2\nu}{2-\nu} (F_2 \tau_{yx} + F_3 \tau_{yz}) \, dr d\theta \quad (V.9b)$$

$$K_{III} = \frac{2^{1/2}}{\pi^{3/2}} \int_0^\pi \int_0^\infty F_1 \tau_{yz} + \frac{2\nu}{2-\nu} (F_3 \tau_{yx} - F_2 \tau_{yz}) \, dr d\theta \quad (V.9c)$$

where  $F_1, F_2, F_3$  are functions of  $\theta$  and  $r$

$$F_1 = r^{-1/2} (\sin\theta)^{1/2} \quad (V.10a)$$

$$F_2 = r^{-1/2} (\sin\theta)^{1/2} (\sin^2\theta - \cos^2\theta) \quad (V.10b)$$

$$F_3 = r^{-1/2} (\sin\theta)^{1/2} 2 \cos\theta \quad (V.10c)$$

and where three separate point force couples  $P_{x_o}, P_{y_o}, P_{z_o}$  in the  $x, y$  and  $z$  directions at  $x_o, y_o,$  and  $z_o$  will produce stress on the crack plane of (Sokolnikoff, McClintok and Argon)

$$\begin{aligned} \sigma_{yy} = & -\frac{P_{z_o}}{D} \frac{(r \cos\theta - z + z_o)}{(R^2)^{3/2}} \left\{ 3 \frac{y_o^2}{R^2} - (1-2\nu) \right\} \\ & + -\frac{P_{x_o}}{D} \frac{(r \sin\theta + x_o)}{(R^2)^{3/2}} \left\{ 3 \frac{y_o^2}{R^2} - (1-2\nu) \right\} \\ & + -\frac{P_{y_o}}{D} \frac{y_o}{(R^2)^{3/2}} \left\{ 3 \frac{y_o^2}{R^2} + (1-2\nu) \right\} \end{aligned} \quad (V.11a)$$

$$\begin{aligned}
\tau_{yx} = & -\frac{3P_{z_0}}{D} \frac{[r\cos\theta - z+z_0][r\sin\theta +x_0] y_0}{(R^2)^{5/2}} \\
& + -\frac{P_{y_0}}{D} \frac{y_0}{(R^2)^{3/2}} \left\{ 3 \frac{(x_0+r\sin\theta)^2}{R^2} + (1-2\nu) \right\} \\
& + -\frac{P_{x_0}}{D} \frac{(r\sin\theta+x_0)}{(R^2)^{3/2}} \left\{ \frac{3y_0^2}{R^2} + (1-2\nu) \right\} \tag{V.11b}
\end{aligned}$$

$$\begin{aligned}
\tau_{yz} = & -\frac{P_{z_0}}{D} \frac{y_0}{(R^2)^{3/2}} \left\{ 3 \frac{(x_0+r\sin\theta)^2}{R^2} + (1-2\nu) \right\} \\
& + -\frac{P_{y_0}}{D} \frac{(r\cos\theta-z+z_0)}{(R^2)^{3/2}} \left\{ 3 \frac{y_0^2}{R^2} + (1-2\nu) \right\} \\
& + -\frac{3P_{x_0}}{D} \frac{y_0[r\sin\theta+x_0][r\cos\theta-z+z_0]}{(R^2)^{3/2}} \tag{V.11c}
\end{aligned}$$

$$\text{where } D = 8\pi (1-\nu) \tag{V.11d}$$

and

$$R^2 = r^2 + 2r[(z_0 - z)\cos\theta + x_0\sin\theta] + (z_0 - z)^2 + x_0^2 + y_0^2 \tag{V.11e}$$

The magnitude of the point forces need not be equal.

The major point of Eqs. (V.10) and (V.11) is that the integrals for  $K_{I,II,III}$  are all of the form



$$\int_0^{\pi} (\sin\theta)^{\ell/2} f(\cos\theta, \cos^2\theta, \sin^2\theta) \cdot$$

$$\cdot \int_0^{\infty} r^{m/2} [r^2 + 2r A (\cos\theta, \sin\theta) + B]^{n/2} dr d\theta \quad (\text{V.12a})$$

$$\ell = 1, 2, 3; m = -1, 1, 3; n = -3, -5 \quad (\text{V.12b})$$

and  $r^2 + 2rA + B \geq 1$  when normalized and when  $r \geq 0$ . The difficulties to be encountered in the general problem are thus well represented by Eq. (V.6).

By using repeated superposition and all  $\Delta K_{I, II, III}$  and  $K_{I, II, III}$  stress field components ( $K_{I, II, III}$  from external loads and  $\Delta K_{I, II, III}$  from interaction of  $K_{I, II, III}$  with an elastic modulus defect or from internal stress fields) of the macroscopic crack for a large number of point forces a useful approximation to a stress free surface and the stress field near the surface can be obtained. This approximation would be of obvious utility in describing the stress field near a single microcrack, an arbitrarily curved crack connected to the half plane macrocrack and other situations of interest.

However, to be useful, the double integral over  $\theta$  and  $r$  must reduce to a few simple terms otherwise the repeated summation over a large number of point forces and  $\Delta K_{I, II, III}$  will be very time consuming. If the variation in  $Z$  of  $\Delta K_I$  for a large number of expanding inclusions with no modulus difference needs to be calculated, a simple expression for the double integral is also needed. The previous situations involve only the interactions between a single elastic defect and its interaction with the macrocrack. If a large number of physically separate defects with

elastic moduli different from the matrix need to be considered, then defect-defect interactions must also be allowed. Situations of this type include many microcracks, crack branching and bowing, and expanding inclusions with moduli differences. For a large number of defects perhaps only near neighbor and next nearest neighbor interactions can be allowed, along with defect-macrocrack interactions.

### V.C. Calculation of $\Delta K_I$

A programmable calculator<sup>\*</sup> and associated hardware and software<sup>\*\*</sup> was used for all numerical calculations. Three methods for obtaining a numerical result were developed, a slow numeric method using Fourier series, a rigorous method and a rapid but non-rigorous method. An analytic solution for  $x_0/a=0$ ,  $z=0$  is available.

#### V.C.1 Fourier Series Method

Equation (V.5) was changed to

$$\Delta K_I = -\left(\frac{2}{\pi}\right)^{3/2} \left(\frac{\Delta V}{V}\right) \frac{E(a)^{1/2}}{9(1-\nu)} \cdot \int_{-\pi/2}^{\pi/2} \int_0^{\pi/2} \frac{(\tan\beta)^{1/2}}{(\tan\beta)^2 + (\tan\xi)^2} \cdot \left(\frac{1}{\cos^2\beta \cos^2\xi}\right) \cdot \left\{\frac{3}{2} y_0^2 [(\tan\xi - z)^2 + (\tan\beta + x_0)^2 + y_0^2]\right\}^{-5/2} - \frac{1}{2} [(\tan\xi - z)^2 + (\tan\beta + x_0)^2 + y_0^2]^{-3/2} d\beta d\xi, \quad (V.13)$$

where  $\eta = \alpha + z$ , then  $x = \tan\beta$ ,  $\eta = \tan\xi$  to reduce the infinite regions of integration to finite regions. Letting

<sup>\*</sup> HP - 41c

<sup>\*\*</sup> Math Pac; Fourier Series and Numerical Integration (Simpson Quadrature) Programs

$$f(\xi, \beta, Z) = \frac{1}{\cos^2 \beta} \left\{ \frac{3}{2} y_o^2 [(\tan \xi - Z)^2 + (\tan \beta + x_o)^2 + y_o^2]^{-5/2} \right. \\ \left. - \frac{1}{2} [(\tan \xi - Z)^2 + (\tan \beta + x_o)^2 + y_o^2]^{-3/2} \right\} \quad (V.14)$$

be represented by a finite Fourier series

$$f(\xi, \beta, Z) = A_o + \sum_{n=1}^9 A_n \cos 2n\xi + B_n \sin 2n\xi \quad (V.15)$$

Then let  $\tan^{-1} \eta = \xi$  and reversing the order of integration,

$$\Delta K_I = C \int_0^{\pi/2} \int_0^{\infty} \frac{(\tan \beta)^{1/2}}{\tan^2 \beta + \eta^2} \cdot \{A_o + \sum_{n=1}^9 A_n(\beta, Z) \cos 2n(\tan^{-1} \eta) \\ + B_n(\beta, Z) \sin 2n(\tan^{-1} \eta)\} d\eta d\beta \quad (V.16a)$$

where

$$C = -\left(\frac{2}{\pi}\right)^{3/2} \left(\frac{\Delta V}{V}\right) \frac{Ea^{1/2}}{9(1-\nu)} \quad (V.16b)$$

Performing the  $\eta$  integration (Appendix C)

$$\Delta K_I = C \int_0^{\pi/2} \frac{\pi}{(\tan \beta)^{1/2}} \{A_o(\beta, Z) + \sum_{n=1}^9 A_n(\beta, Z) \left(\frac{1-\tan \beta}{1+\tan \beta}\right)^n\} d\beta \quad (V.17)$$

If we let

$$\int_0^{\pi/2} f(\beta, Z) d\beta \sim \sum_{m=1}^{32} \frac{\pi}{64} f\left(\frac{(2m-1)\pi}{64}, Z\right) \quad (V.18)$$

then

$$\Delta K_I \sim C \sum_{m=1}^{32} \sum_{n=0}^9 \frac{\pi}{64} \frac{A_n(\beta_f, Z)}{(\tan \beta_f)^{1/2}} \left(\frac{1-\tan \beta_f}{1+\tan \beta_f}\right)^n \quad (V.19a)$$



where

$$\beta_{\text{finite}} = \frac{(2m-1)\pi}{64} \quad (\text{V.19b})$$

So for each value of  $Z$  that  $\Delta K_I$  will be calculated, for a given  $x_o, y_o$ ; 320 Fourier cosine coefficients must be found, ten coefficients for each value of  $\beta_f$ .

The HP-41c is a slow computer and performing this calculation for each  $x_o, y_o, Z$  chosen took about five hours. To determine how fast this type of calculation scheme was converging to a reliable answer,  $\Delta K_I$  was calculated with the  $\beta$  distance divided into 1, 2, 4, 8, 16, 32, 64, and 128 equal width sections with Fourier series found for  $f(\xi, \beta, Z)$  at the mid-point of the section with  $Z=0, x_o=2$  and  $y_o=0$  (Table XII). The difference from the previous answer decreases as the number of sections increased and appears to be converging. Dividing  $\beta$  into thirty-two sections for further calculations was a compromise between speed and accuracy.

$\Delta K_I$  vs.  $Z$  curves were calculated for four spherical inclusion positions:  $x_o/a=-2, y_o/a=2, (2,0), (2,2)$  and  $(2,0)$  Figures V.2-5. At large  $Z$ , for  $(-2,2)$  or any negative  $x_o$ , a ten term Fourier series is insufficient to accurately model the real function, Figure V.2. As the sphere rotates from the front to behind the crack tip, the  $\Delta K_I$  at  $Z=0$  changes from + to -, which is very reasonable. Except for  $(+2,0)$ , as  $Z$  becomes large, the  $\Delta K_I$  changes from - to +. These curves are in qualitative agreement with results from Evans et al. (1981a).

Although informative curves were obtained, this method was quite slow. A better procedure would have been to use Eq. (V.6) and integrate numerically using two-dimensional cubic splines with a large computer (Hildebrand, 1974). Adjustable 2-D subintervals for the splines would

Table XII

Fourier Series Method

$$x_o = 2 \quad y_o = 0 \quad z = 0$$

$\frac{K_I}{c} \times 10$	# sections for $\beta_{finite}$	% difference from $\beta_f=128$	% difference from next $\beta_f$	time for computation
1.2727	1	52	24	10 min
1.6718	2	37	16	20 min
1.9963	4	25	11	40 min
2.2339	8	16	6.9	1.25 hr
2.3982	16	9.3	4.5	2.5 hr
2.51555	32	5.1	3.1	5 hr
2.5902	64	2.1	2.1	10 hr
2.6453	128	-	-	20 hr

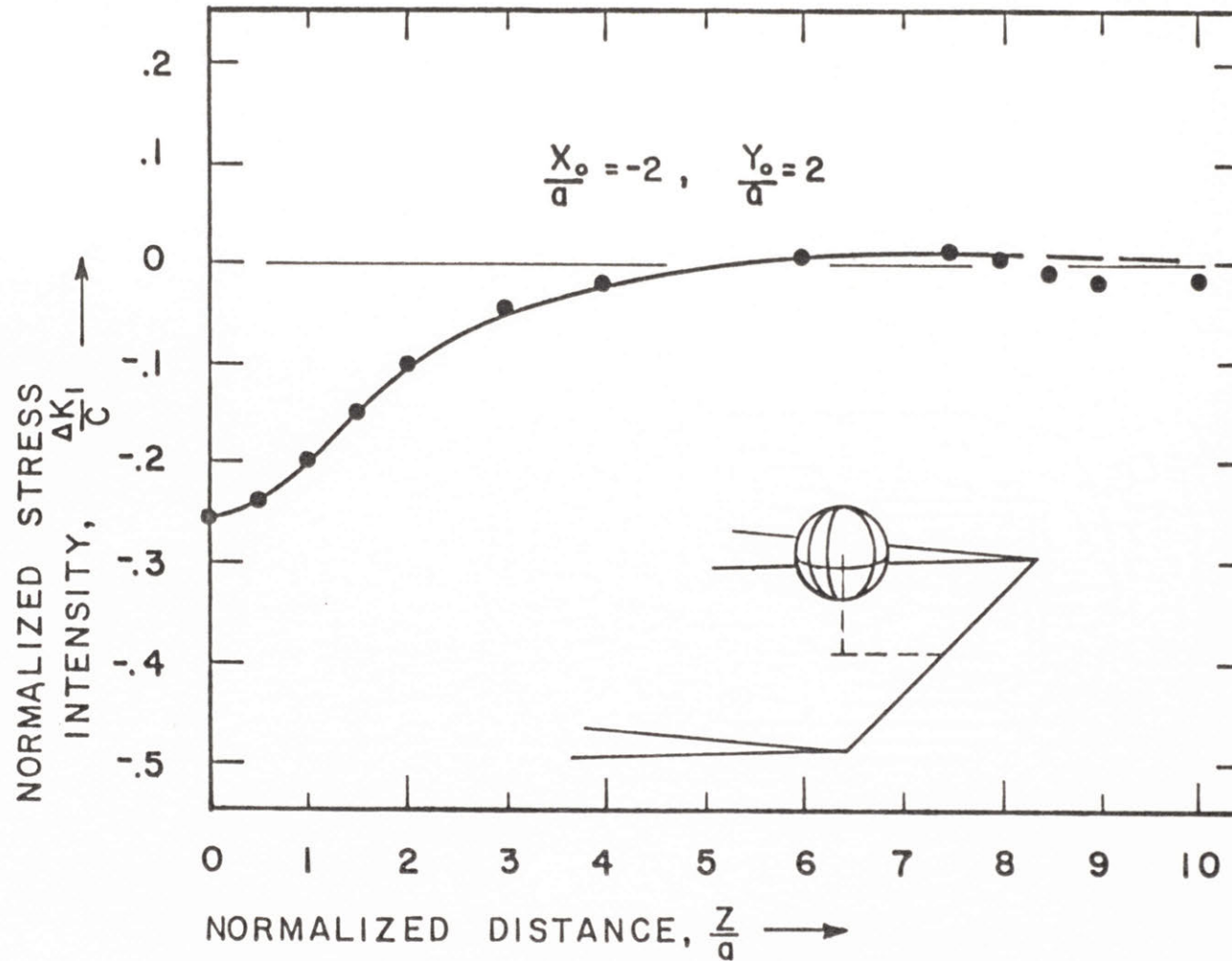


Figure V 2 Normalized stress intensity vs. normalized distance along the crack front calculated by the Fourier series method (Equation V 19) for an inclusion position of  $\frac{X_0}{a} = -2, \frac{Y_0}{a} = 2$ .

$$C = \frac{(2)}{(\pi)}^{3/2} \frac{(\Delta V)}{(V)} \frac{E a^{1/2}}{9(1-\nu)}$$



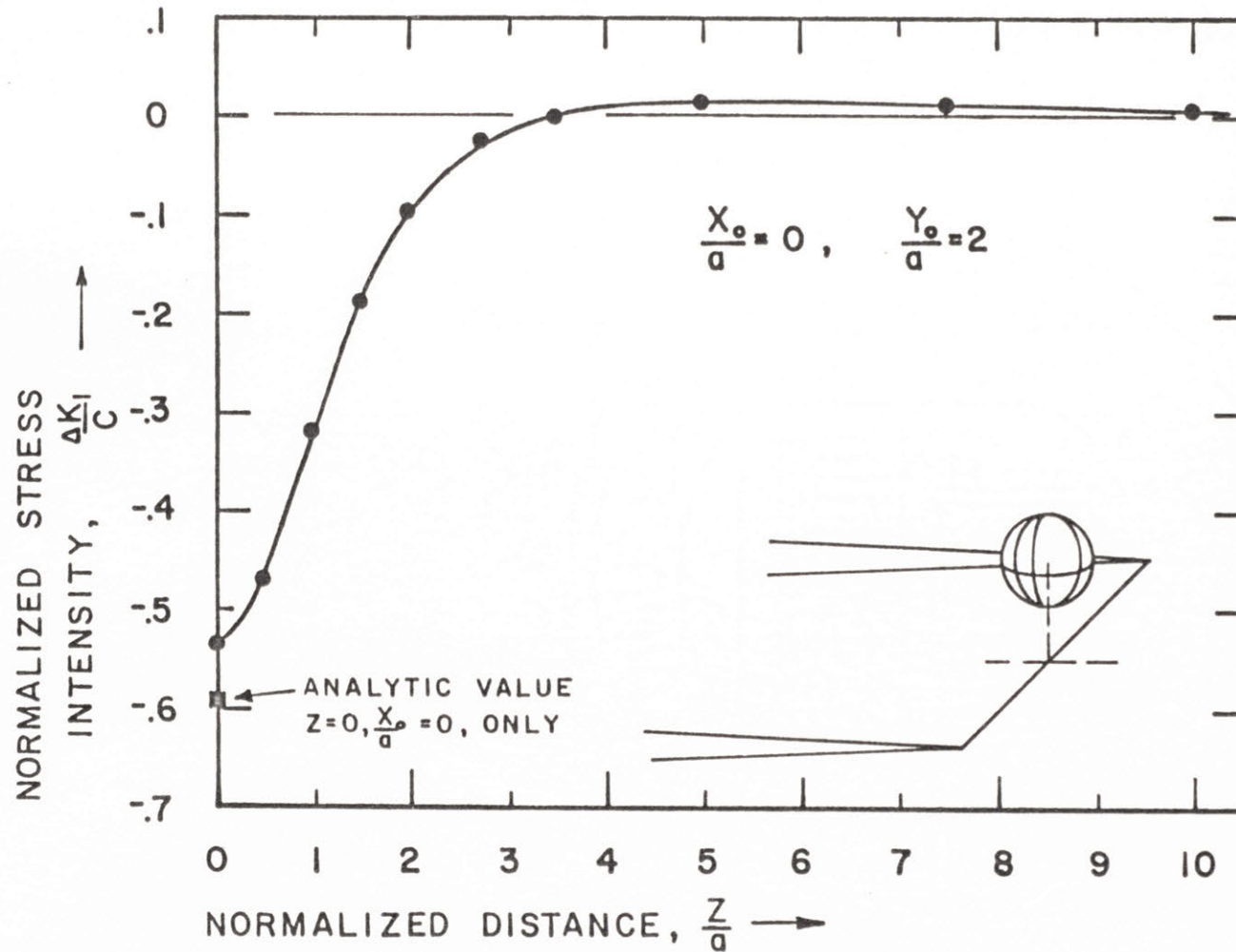


Figure V 3 Normalized stress intensity vs. normalized distance along the crack front calculated by the Fourier series method (equation V 19) for an inclusion position of  $\frac{X_0}{a} = 0, \frac{Y_0}{a} = 2$ .

$$C = \frac{(2)^{3/2}}{(\pi)} \frac{(\Delta V)}{(V)} \frac{E a^{1/2}}{9(1-\nu)}$$

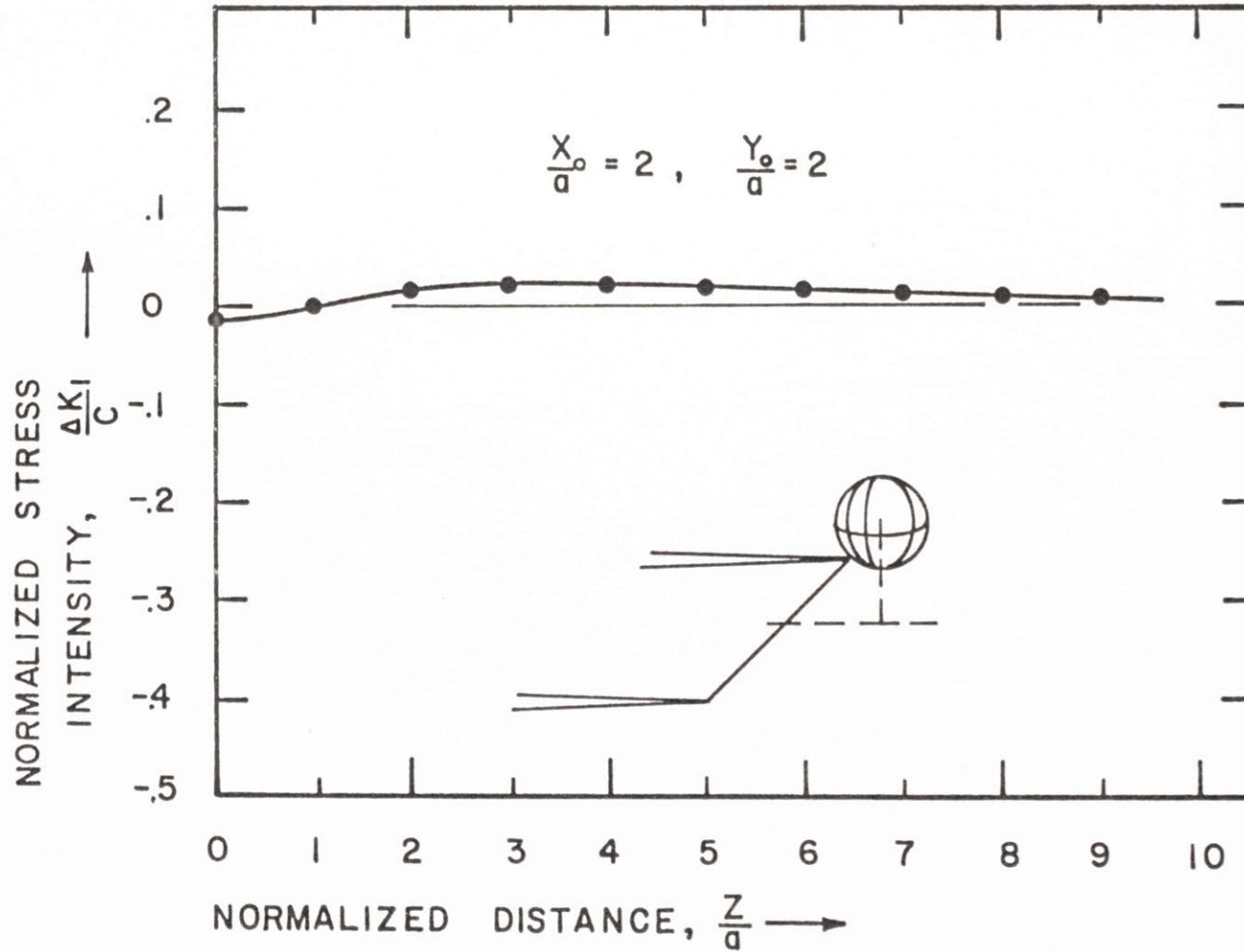


Figure V 4 Normalized stress intensity vs. normalized distance along the crack front calculated by the Fourier series method (equation V 19) for an inclusion position of  $\frac{X_0}{a} = 2, \frac{Y_0}{a} = 2$ .

$$C = \frac{(2)}{(\pi)}^{3/2} \frac{(\Delta V)}{V} \frac{E a^{1/2}}{9(1-\nu)}$$

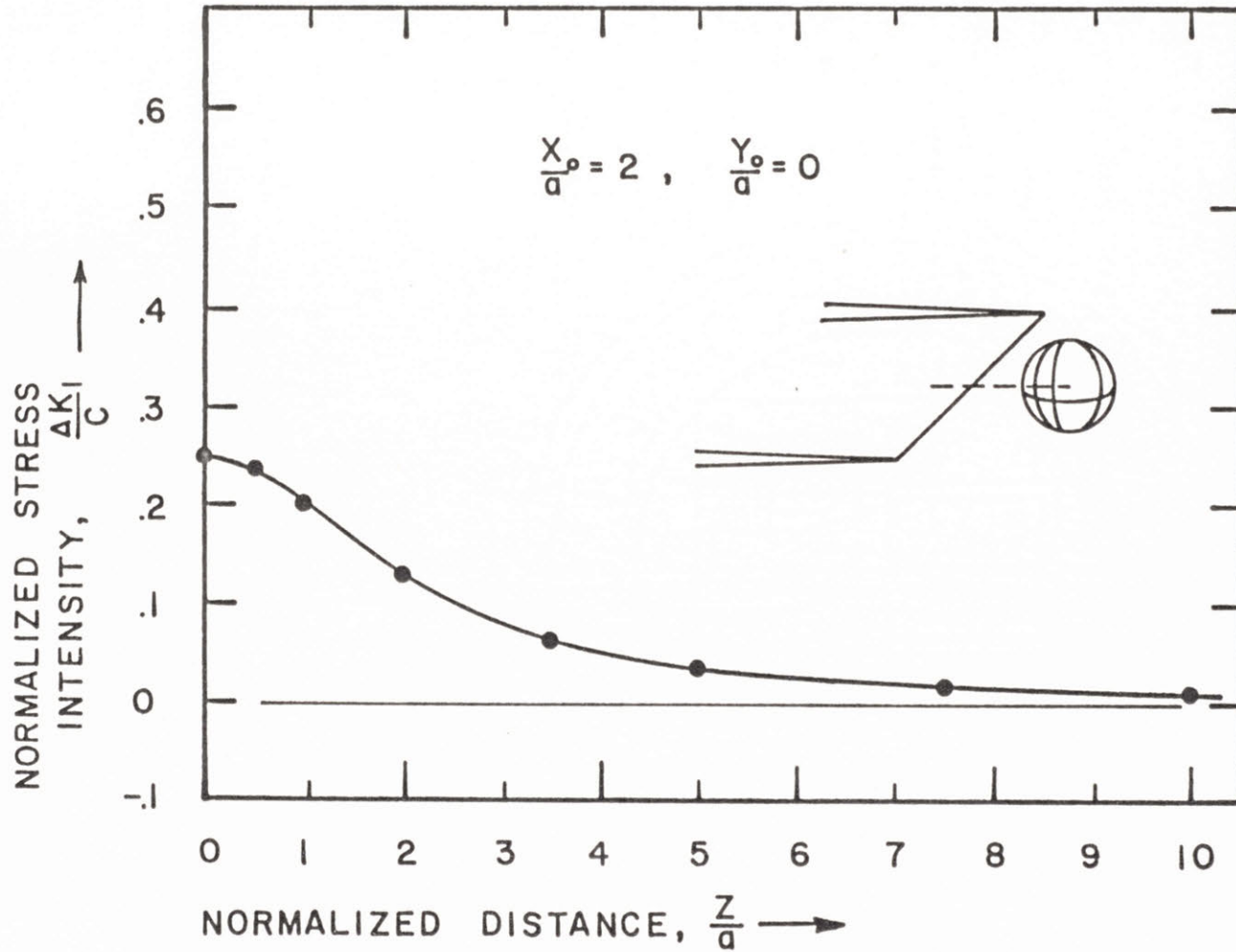


Figure V 5 Normalized stress intensity vs. normalized distance along the crack front calculated by the Fourier series method (equation V 19) for an inclusion position of  $\frac{X_o}{a} = 2, \frac{Y_o}{a} = 0$ .

$$C = \frac{(2)}{(\pi)} \frac{3/2}{(V)} \frac{(\Delta V) E a^{1/2}}{9(1-\nu)}$$



be necessary to model the  $r^{-1/2}$  singularity accurately as  $r$  approaches zero. Attempts to integrate either Eq. (V.5) or (V.12) numerically by Simpson quadrature failed because the singularity was not accurately modelled. The areas of integration near the singularity must become smaller and smaller, but the methods developed only allowed smaller areas of integration over the entire range of integration.

### V.C.2. A Rigorous Method

A rigorous method can be obtained as follows. The inverse distance between two points  $x$  and  $x'$  in three-dimensional space for  $r' < r$  where  $r'$  and  $r$  are distances from the origin can be represented by

$$\frac{1}{|\underline{x}-\underline{x}'|} = \sum_{\ell=0}^{\infty} \frac{r'^{\ell}}{r^{\ell+1}} P_{\ell}(\cos\phi) \quad (V.20)$$

where  $\phi$  is the angle between the vectors  $\underline{x}$  and  $\underline{x}'$ , and  $P_{\ell}(\cos\phi)$  is a Legendre polynomial (Jones). If  $r' > r$ , then reverse the notation.

$$[(\xi+x_0)^2 + (Z-\alpha)^2 + y_0^2]^{1/2} \quad (V.21)$$

is the distance from point  $x_0, y_0, Z$  to point  $\xi, -\alpha$  (the sense of  $\xi$  and  $\alpha$  are opposite that of  $x$  and  $Z$ ). Point  $\xi, -\alpha$  is confined to lie in the half plane representing the crack, thus

$$\begin{aligned} \Delta K_I = & C \int_0^{\pi} (\sin\theta)^{1/2} \int_0^{r'} r^{-1/2} \cdot \left\{ \frac{3}{2} y_0^2 \left[ \sum_{\ell=0}^{\infty} \frac{r^{\ell}}{r^{\ell+1}} P_{\ell}(\cos\phi) \right]^5 \right. \\ & \left. - \frac{1}{2} \left[ \sum_{\ell=0}^{\infty} \frac{r^{\ell}}{r^{\ell+1}} P_{\ell}(\cos\phi) \right]^3 \right\} dr d\theta \\ & + C \int_0^{\pi} (\sin\theta)^{1/2} \int_{r'}^{\infty} r^{-1/2} \cdot \left\{ \frac{3}{2} y_0^2 \left[ \sum_{\ell=0}^{\infty} \frac{r'^{\ell}}{r^{\ell+1}} P_{\ell}(\cos\phi) \right]^5 \right. \\ & \left. - \frac{1}{2} \left[ \sum_{\ell=0}^{\infty} \frac{r'^{\ell}}{r^{\ell+1}} P_{\ell}(\cos\phi) \right]^3 \right\} dr d\theta \quad (V.22a) \end{aligned}$$

where

$$r' = [x_0^2 + y_0^2 + z^2]^{1/2} \quad (V.22b)$$

and

$$\phi = \cos^{-1} \left[ - \frac{x_0 \sin\theta + z \cos\theta}{(x_0^2 + y_0^2 + z^2)^{1/2}} \right] \quad (V.22c)$$

$P_\ell$  is then, a simple polynomial of  $\sin\theta$  and  $\cos\theta$ , then finding  $P_\ell^{3,5}$  is simple algebra and the resulting integrations are elementary if tedious. Computer programs are available to do this simple algebra and calculus (Pavelle, et al.). This may result in a slowly converging series and no numerical calculations were performed.

### V.5.3. Rapid Non-rigorous Solution

A rapid non-rigorous method that seems to be useful has been developed. An analytic expression for

$$\int_0^\infty r^{-1/2} (r^2 + rA + B)^{-3/2, -5/2} dr$$

could not be obtained. This form could not be found in tables (C.R.C. Standard Math. Tables, Gradshteyn and Ryzhik), nor integrated using complex variable methods (Hildebrand, 1976, Marsden, Henrici, Greenleaf) asymptotic analysis (Bender and Orszag), or repeated integration by parts.

The integrals

$$\int_0^\infty r^{-1/2} (r^2 + rA + B)^{-1} = \frac{\pi}{M} \frac{\cos(\frac{\phi}{2})}{(M^2 + N^2)^{1/4}} \quad (V.23a)$$

$$\int_0^\infty r^{-1/2} (r^2 + rA + B)^{-2} = \frac{\pi}{2M^3} \frac{\cos(\frac{\phi}{2})}{(M^2 + N^2)^{1/4}} + \frac{\pi \sin(\frac{3\phi}{2})}{4M^2 (M^2 + N^2)^{3/4}} \quad (V.23b)$$

$$\int_0^{\infty} r^{-1/2} (r^2+rA+B)^{-3} = \frac{3\pi \cos(\frac{\phi}{2})}{8M^5 (M^2+N^2)^{1/4}} + \frac{3\pi \sin(\frac{3\phi}{2})}{16M^4 (M^2+N^2)^{3/4}} + \frac{-3\pi \cos(\frac{5\phi}{2})}{32 M^3 (M^2+N^2)^{5/4}} \quad (V.23c)$$

$$\text{where } N = A/2, M = (B-A^2/4)^{1/2} \quad (V.23d)$$

and

$$\phi = \cos^{-1} \frac{-A}{2(B)^{1/2}} \quad (V.23e)$$

are easily obtained via residue calculus (Appendix C) when

$$r^2 + Ar + B \geq 1 \quad \text{where } r \geq 0$$

From the regular forms of Eqs. (V.23a-c) one would guess that

$$\int_0^{\infty} r^{-1/2} (r^2+rA+B)^{-3/2} dr = C_{11} \frac{3\pi \cos(\frac{\phi}{2})}{4M^2 (M^2+N^2)^{1/4}} + C_{12} \frac{\sin\pi(\frac{3\phi}{2})}{8M (M^2+N^2)^{3/4}} \quad (V.24a)$$

and

$$\int_0^{\infty} r^{-1/2} (r^2+rA+B)^{-5/2} dr = C_{21} \frac{7\pi \cos(\frac{\phi}{2})}{16M^4 (M^2+N^2)^{1/4}} + C_{22} \frac{7\pi \sin(\frac{3\phi}{2})}{32M^3 (M^2+N^2)^{3/4}} + C_{23} \frac{-3\pi \cos(\frac{5\phi}{2})}{64 M^{3/2} (M^2+N^2)^{5/4}} \quad (V.24b)$$

with  $C_{ij}$   $i=1,2$ ;  $j=1,2,3$  numerical constants to be determined.

The left sides of Eqs. (V.24a,b) were numerically integrated for four pairs of A and B in the range of interest, the right sides were



then calculated and the answers compared.\* For the values of A and B of (1, 10), (1, 2), (-5, 25) and (-20, 401), Eq. (V.24a) represented the numerical value within +8%, -6% with  $C_{11} = C_{12} = 1$ . For the same pairs of A and B Eq. (V.24b) represented the numerical value within +11%, -6% with  $C_{21}=C_{22}=C_{23}=1$ . The numerical values for the integrals for these pairs of A and B vary over two orders of magnitude for Eq. (V.24a) and over four orders of magnitude for Eq. (V.24b). Thus,

$$\Delta K_I = C \int_0^\pi (\sin\theta)^{1/2} \cdot \left\{ \frac{3}{2} y_o^2 \cdot \left[ \frac{7\pi \cos(\frac{\phi}{2})}{16R^4(Q)^{1/4}} + \frac{7\pi \sin(\frac{3\phi}{2})}{32R^3(Q)^{3/4}} + \frac{-3\pi \cos(\frac{5\phi}{2})}{64R^{3/2}(Q)^{5/4}} \right] - \frac{1}{2} \left[ \frac{3\pi \cos(\frac{\phi}{2})}{4R^2Q^{1/4}} + \frac{\pi \sin(\frac{3\phi}{2})}{8R(Q)^{3/4}} \right] \right\} d\theta \quad (V.25a)$$

where

$$R = [x_o^2 + y_o^2 + Z^2 - (-Z \cos\theta + x_o \sin\theta)^2]^{1/2} \quad (V.25b)$$

$$Q = (x_o^2 + y_o^2 + Z^2) \quad (V.25c)$$

and

$$\phi = \cos^{-1} \frac{(-Z \cos\theta + x_o \sin\theta)}{(x_o^2 + y_o^2 + Z^2)^{1/2}} \quad (V.25d)$$

---

\*The original intent was to form simultaneous equations for about 8 pairs of A and B and find a least squares fit for  $C_{ij}$ , but the HP-41c simultaneous equations program would only find exact answers. This also ignores the problem of weighing functions, i.e., accuracy at small  $x_o$ ,  $y_o$ ,  $Z$  more important or is accuracy at large or intermediate  $x_o$ ,  $y_o$ ,  $Z$  important?

This equation can be rapidly integrated numerically over  $\theta$  with Simpson quadrature at only ten points. This took only two minutes with the HP-41c.

A comparison of  $\Delta K_I$  curves calculated via Eq. (V.25) vs. Eq. (V.19) is shown in Figures V.6-9. This method represents the  $\Delta K_I$  well (perhaps better than Eq. (V.19) over most of the  $x_o, y_o, Z$  range, but diverges as  $Z$  and  $y_o$  approach zero simultaneously, Figure V.9. This is because as

$$\theta \rightarrow \pi/2, [x_o^2 + y_o^2 + Z^2 - (-Z \cos \theta + x_o \sin \theta)^2]^{-1/2} \rightarrow \infty \quad (V.26)$$

This is a result of two poles combining in the complex plane, Appendix C.

To correct this difficulty, maximum values for the integrals

$$\int_0^{\infty} r^{-1/2} [r^2 + rA + B]^{-3/2, -5/2} dr$$

where  $x_o \geq 0$  can be found and these values substituted in Eq. (V.25a) when Eqs. (V.24a,b) exceed these maximum values, Appendix C. This limited form of Eq. (V.25) is also plotted on Figure V.10.

The same type of difficulty may also occur as  $\theta$  approaches 0 or  $\pi$  when  $Z^2 \gg x_o^2 + y_o^2$  for any value of  $x_o$  or  $y_o$ . Evidently the  $(\sin \theta)^{1/2}$  removes this problem. Difficulties might also be expected when  $x_o < 0$  and  $x_o^2 \gg Z^2 + y_o^2$  as  $\theta$  approaches  $\pi/2$ . For  $x_o < 0, y_o > 1$ , an examination of Figure V.9 near  $Z=1$  would indicate using Eq. (V.25) is not too inaccurate, as long as

$$[x_o^2 + y_o^2 + Z^2 - (-Z \cos \theta + x_o \sin \theta)^2]^{-1/2} > 1$$

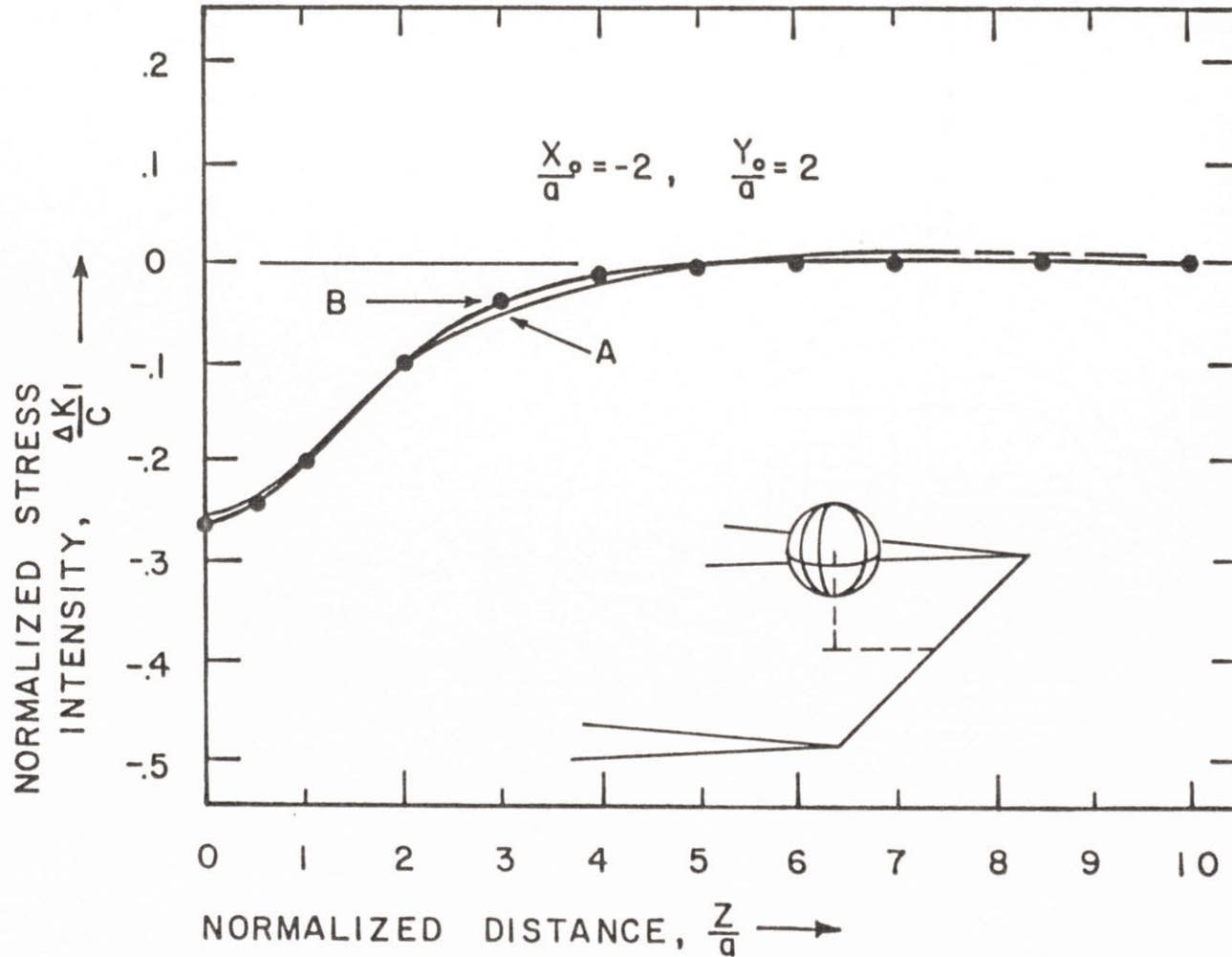


Figure V 6 Comparison of normalized stress intensity vs. normalized distance curves calculated by the rapid non-rigorous method (RNR), equation V 25 curve B, and the Fourier series method, equation V 19 curve A.  $\frac{X_0}{a} = -2, \frac{Y_0}{a} = 2,$

$$C = \frac{(2)}{(\pi)}^{3/2} \frac{(\Delta V)}{(V)} \frac{E a^{1/2}}{9(1-\nu)}$$



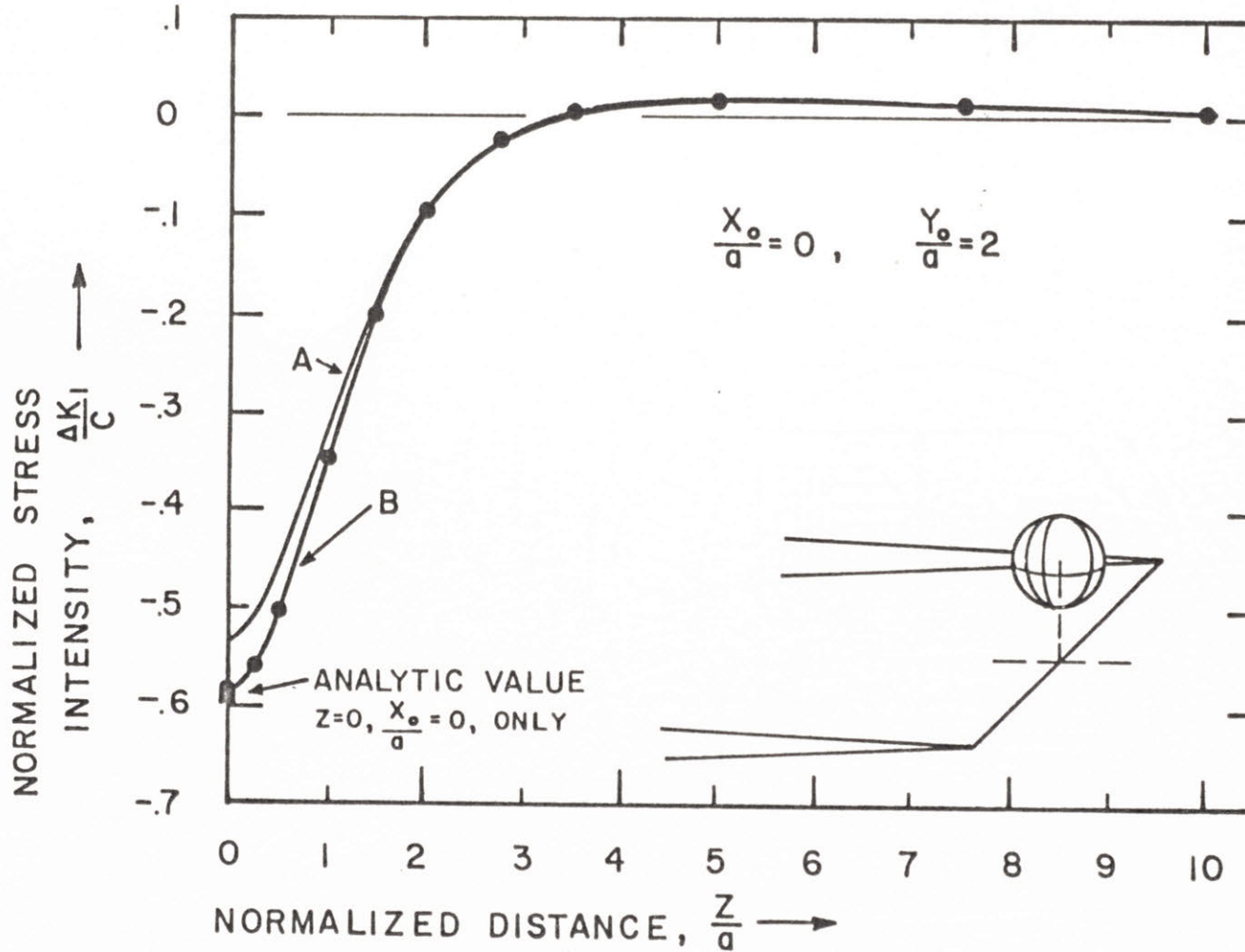


Figure V 7 Comparison of normalized stress intensity vs. normalized distance curves calculated by the rapid non-rigorous method (RNR), equation V 25 curve B, and the Fourier series method, equation V 19 curve A.  $\frac{X_o}{a} = 0, \frac{Y_o}{a} = 2,$

$$C = \frac{(2)}{(\pi)}^{3/2} \frac{(\Delta V)}{(V)} \frac{E a^{1/2}}{9(1-\nu)}$$

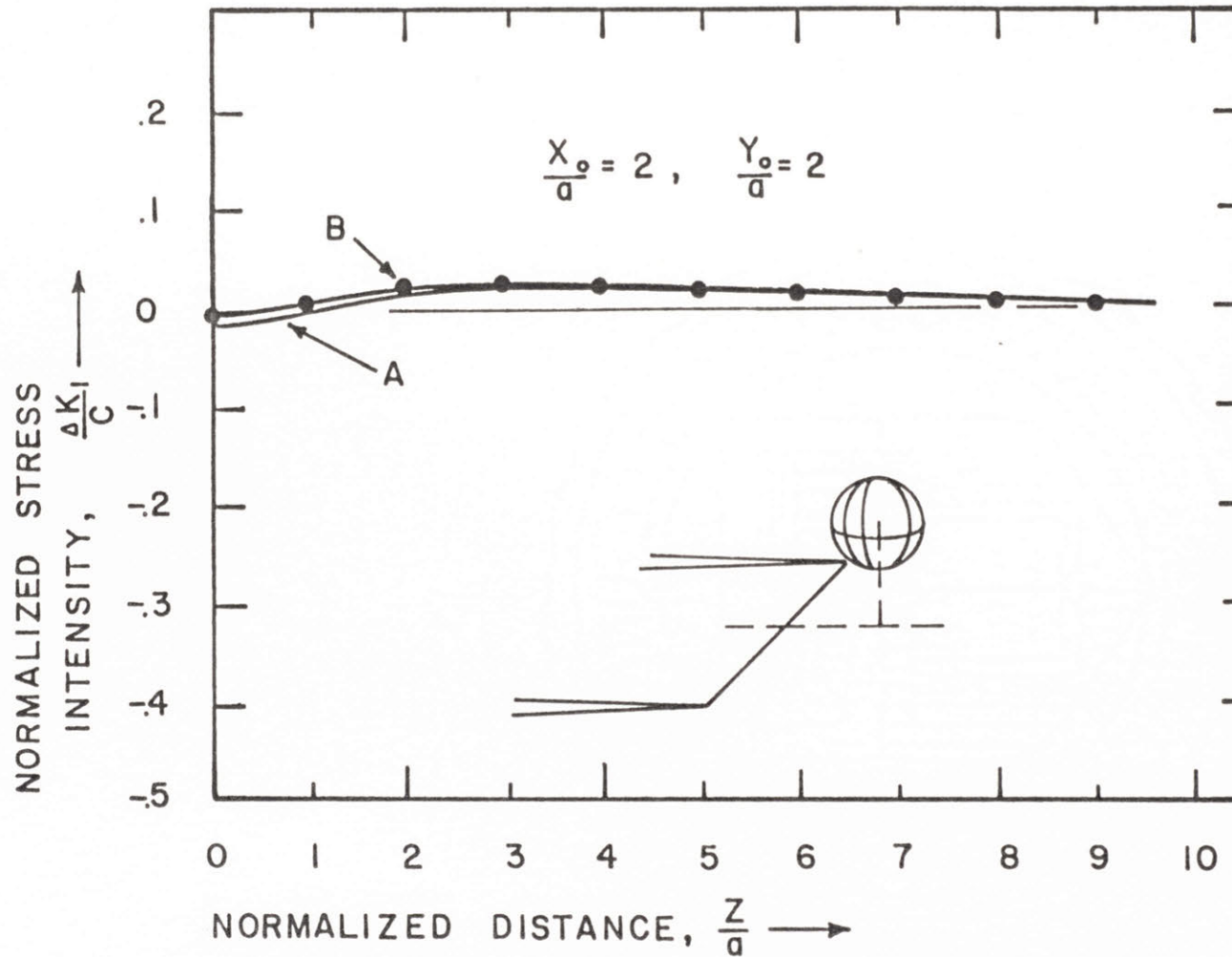


Figure V 8 Comparison of normalized stress intensity vs. normalized distance curves calculated by the rapid non-rigorous method, (RNR), equation V 25 curve B, and the Fourier series method, equation V 19 curve A.  $\frac{X_0}{a} = 2, \frac{Y_0}{a} = 2,$

$$C = \frac{(2)^{3/2}}{(\pi)} \frac{(\Delta V)}{(V)} \frac{E a^{1/2}}{9(1-\nu)}$$

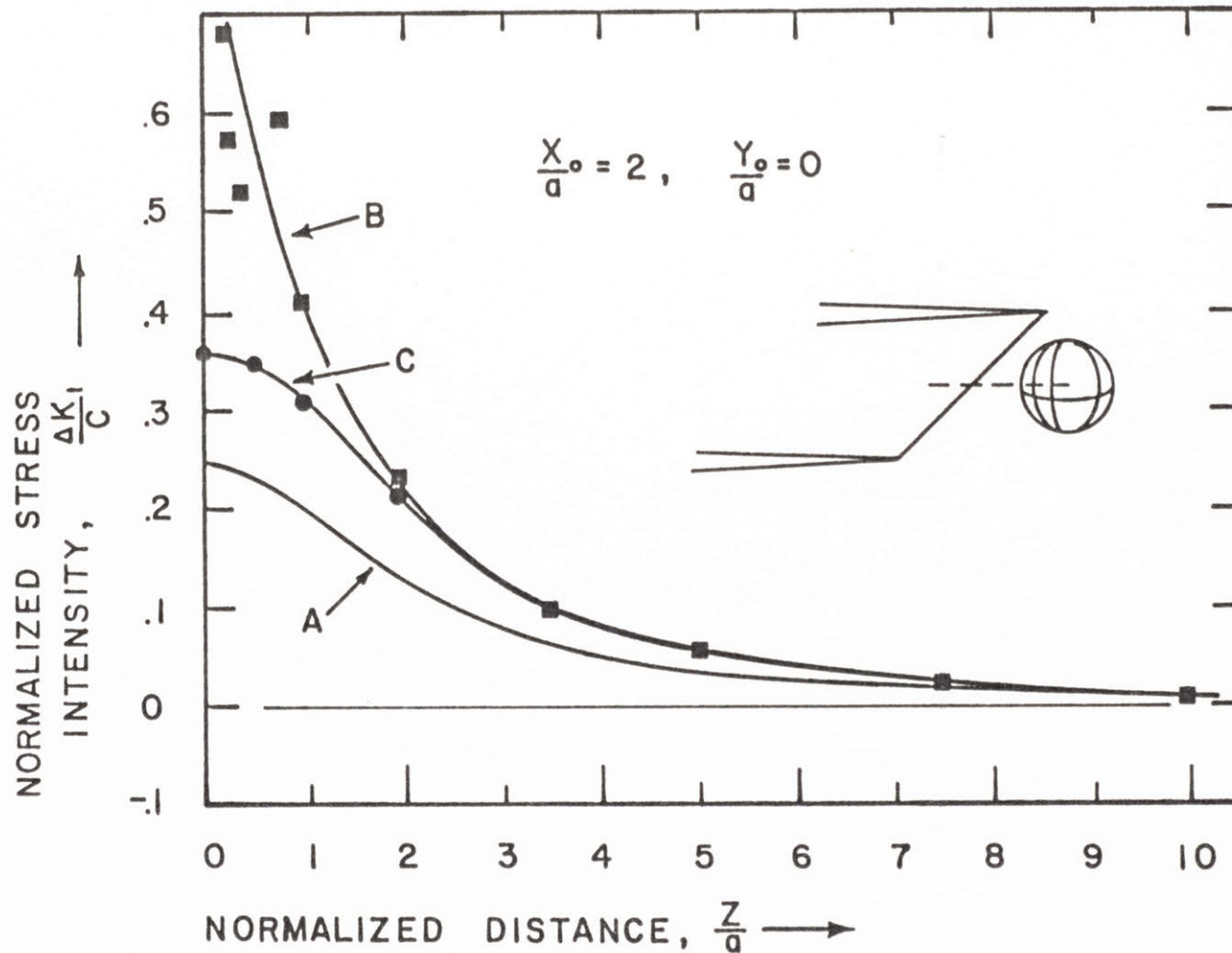


Figure V 9 Comparison of normalized stress intensity vs. normalized distance curves calculated by the rapid non-rigorous method (RNR), equation V 25 curve B, the limited rapid non-rigorous method (LRNR), equations V 25 and A.C. 17 curve C, and the Fourier series method, equation V 19 curve A.  $\frac{X_0}{a} = 2, \frac{Y_0}{a} = 0,$

$$C = \frac{(2)}{(\pi)} \frac{3/2}{(\Delta V)} \frac{E a^{1/2}}{9(1-\nu)}$$



A more accurate method of approximation can be developed using Taylor series when  $\theta$  approaches  $\pi/2$ , Appendix C.

## V.D. DISCUSSION

If  $\psi$  is the polar angle from directly ahead of the crack and  $R$  the distance from the crack tip, the four inclusion positions  $(2,0)$ ,  $(2,2)$ ,  $(0,2)$  and  $(-2,2)$  are  $(0,2)$ ,  $(\pi/4, 2\sqrt{2})$ ,  $(\pi/2, 2)$  and  $(3\pi/4, 2\sqrt{2})$  respectively. From the eight  $\Delta K_I$  vs.  $z/a$  curves, the  $\Delta K_I$  passes from positive  $\Delta K_I$  to negative  $\Delta K_I$  for  $z=0$  at  $\psi \sim \pi/4$  for a positive  $\Delta V$ . The maximum negative amplitude of  $\Delta K_I$  at  $\psi = \pi/2$  is larger than the maximum positive amplitude at  $\psi = 0$ . The maximum negative amplitude of  $\Delta K_I$  is still appreciable at  $\psi = 3\pi/4$ . A reasonable expectation is that for a uniformly distributed array of inclusions with a positive  $\Delta V$ ,  $\Sigma \Delta K_I < 0$  along the entire crack front. When the  $\Delta V$  is negative the sign of  $\Delta K_I$  will be reversed in the above statements, and for a large uniformly distributed array of inclusions  $\Sigma \Delta K_I > 0$  along the entire crack front. This assumes that the stress field caused by an expanding inclusion is that caused by a single misfitting inclusion in an infinite matrix. This is appropriate for small volume fractions of inclusions. At higher volume fractions of inclusions the stress field of an individual inclusion might be more accurately modelled by a combination of the stresses present from a misfitting spherical inclusion imbedded in a larger sphere of matrix material (with the radii adjusted for the given volume fraction of inclusions) and a uniform compression or dilation over the entire zone with transformed inclusions. This uniform hydrostatic stress will tend to adjust  $\Sigma \Delta K_I$  toward zero for both positive and negative  $\Delta V$ .

The results of the computations on an individual inclusion level illustrate why Evans et al. (1981a) obtain R curve behavior with a positive  $\Delta V$  in their transformation toughening model. When transformation

occurs ahead of the crack tip,  $\pi/4 > \psi > -\pi/4$ , the crack must advance past the inclusions to obtain much negative  $\Delta K_I$ . The more transformed inclusions behind the crack tip there are, the larger negative  $\Delta K_I$  is obtained. Thus transformation toughening models should be extremely sensitive to zone shape.

A single inclusion at  $\psi=0$ ,  $R=2$  and  $\psi=\pi/2$ ,  $R=2$  have maximum  $\Delta K_I$ 's of +0.14 and -0.22 MPa m<sup>1/2</sup>, when an average Young's modulus for ThO<sub>2</sub>-ZrO<sub>2</sub> of 240 GPa, an inclusion radius of 0.5 micron and a volume expansion of 3% are used. These numbers seem physically realistic. In addition only modest numbers of inclusions may be necessary to produce an average  $\Delta K_I$  along the crack front approaching the toughening the levels measured in Section IV (for ThO<sub>2</sub>-ZrO<sub>2</sub>,  $\Sigma \Delta K_I \sim 1-1.5$  MPa m<sup>1/2</sup> above the  $K_{IC}$  of ThO<sub>2</sub>).

The numerical solutions to the Fourier series method and limited rapid non-rigorous (LRNR) method both predict crossovers from  $-\Delta K_I$  to  $+\Delta K_I$  for  $\psi > \pi/4$  but no change in sign for  $\psi=0$  as  $z/a \rightarrow \infty$ . This is reasonable as the sign of the  $\Delta K_I$  is a balance between integrals containing tangential and radial stress fields normal to the crack plane. As  $z/a \rightarrow \infty$  the tangential field dominates the integral but near the inclusion for  $\psi > \pi/4$  the radial stress field dominates. For  $\psi=0$  there is never any radial contribution. For  $\psi=0$ , Figure V.9 the LRNR method overestimates the magnitude of the  $\Delta K_I$  as  $z/a \rightarrow 0$ . The Fourier series method probably underestimates the magnitude of the  $\Delta K_I$  because as more sections were subdivided for  $\beta$  (Eq. V.19b) the  $\Delta K_I$  for  $z/a=0$ ,  $x_o/a=2$  and  $y_o/a=0$  was increasing, Table XII. The accuracy of the LRNR method will improve if a Taylor series approximations for the maximum of the integrals are used (Appendix C4) rather than the  $\Gamma$  function approximation, Appendix C3.



The limited rapid non-rigorous (LRNR) solutions seems to be reasonably accurate over most of the range ( $z/a < 10, -2 \leq x_0/a \leq 2, 0 \leq y_0/a \leq 2$ ) covered by the inclusion positions (0,2), (-2,2), (2,2) and (2,0). For simple iterative procedures that can model elastic moduli differences between the matrix and inclusion, reasonable accuracy is probably insufficient as the error can be additive at each iteration. The accuracy of the LRNR solution should be checked by the rigorous Legendre series method for specific  $x_0/a, y_0/a$  and  $z/a$ . It is anticipated that to obtain an accurate solution by the rigorous method more computation time would be expended than for the LRNR method. If not, then the rigorous method should be used. The Taylor series approximation (Appendix C4) should be included in the LRNR method to obtain higher accuracy. Specific ranges of  $z/a, x_0/a,$  and  $y_0/a$  where the LRNR method's accuracy may be poor are:  $(x_0/a)^2 \gg (y_0/a)^2 + (z/a)^2$  and  $(z/a)^2 \gg (y_0/a) + (x_0/a)^2$ ; i.e., where  $R,$  Eq. (V.25b), can approach zero.

The situation of a single misfitting inclusion around which circumferential or radial microcracking has occurred can be qualitatively examined by the model developed in the previous section. If an inclusion in front of the crack plane,  $-\pi/4 < \psi < \pi/4,$  is in tension the model would predict a negative  $\Delta K_I$  near the inclusion along a straight crack front. Thus the inclusion would act to make the crack bow around it, or deflect out of the plane to pass it. If the inclusion cracks circumferentially along the entire inclusion/matrix interface, then a pore is produced. If an external stress is applied, an iterative procedure using the model will produce a position  $\Delta K_I$  near the pore; the ligament between the crack and pore will have a high tensile stress and the crack will bow toward

the pore, assuming a crack will propagate to maintain a constant  $K_I$  along a curved crack front. The crack extension increment can be described by the change in the bowing of the crack from away from the inclusion to towards the inclusion. If an inclusion in front of the crack plane in compression that cracks radially is considered a different situation occurs. Before the microcracking a positive  $\Delta K_I$  exists near the inclusion on a straight crack front, a real macrocrack will bow towards the inclusion. When radial microcracking occurs under an applied stress the microcracks probably propagate towards the main crack while the  $\Delta K_I$  on the main crack is still positive and probably greater than the  $\Delta K_I$  before microcracking. This will probably result in microcrack-macrocrack linkage and a large crack extension increment per radial microcrack event. When the radial microcracking occurs above or behind the crack plane the situation is different. For an inclusion in compression, the  $\Delta K_I$  is negative near the inclusion. When radial microcracking occurs, the  $\Delta K_I$  will still be negative but the magnitude will be reduced. The magnitude will be determined by how much strain is left in the inclusion/matrix, the applied stress and the direction(s) of the microcracking. However, the  $\Delta K_I$  is still negative and crack propagation is impeded. For an inclusion in tension behind the crack that cracks circumferentially the analysis is unclear. Before cracking the  $\Delta K_I$  near the inclusion is positive and the main crack will bulge forward. After microcracking the  $\Delta K_I$  is negative under an applied stress and the main crack would tend to lag behind locally under the inclusion, but to obtain such a crack curvature the entire crack front must advance.

For crack branching and local crack deflection out of the original

crack plane  $\Delta K_{II}$  and  $\Delta K_{III}$  must be included in any model.  $\Delta K_{II}$  and  $\Delta K_{III}$  provide shearing forces that can twist the crack locally out of plane in response to the stresses producing the  $\Delta K_{II\&III}$ . When  $\Delta V$  is positive this can lead to crack deflection toward the inclusion. When  $\Delta V$  is negative the inclusion may deflect the crack out of plane, generally following the tensile tangential stress field. If two inclusions are placed at the same R but at exactly opposite  $\psi$ 's the effects of  $\Delta K_{II}$  and  $\Delta K_{III}$  may cancel.

Calculation of  $\Delta K_I$  for an expanding inclusion involved solving two double integrals of the type given by equation V12. Calculation of  $\Delta K_I$  for a general triplet of point forces will involve solving three double integrals of the type given by equation V12. Calculation of  $\Delta K_{II}$  and  $\Delta K_{III}$  will each involve solving nine double integrals of the type given by equation V12. The three methods of solution given by the preceding section can be used for these double integrals but the LRNR method is probably the most useful. The LRNR method is based on the interpolation of the forms of the integrals over r and was used with equations V23 and V24. This interpolation can be directly and easily applied to the integrals over r that describe  $\Delta K_{I,II,III}$  for generalized point forces. Numerical integration for the integrals over  $\theta$  is rapid and simple. Thus a generalized LRNR method for  $\Delta K_{I,II,III}$  for generalized point forces presents no major mathematical or computational difficulties.

The calculations for  $\Delta K_I$  and a single inclusion show that for a positive  $\Delta V$ , a negative  $\Delta K$  results at  $Z=0$  for inclusion positions where  $\psi \rightarrow \pi$ . The calculations were based on a stress superposition argument and thus any stress normal to the crack plane on the crack was cancelled.



If however the local strain caused by an expanding inclusion is larger than the crack opening displacement (C.O.D.) then normal stress can be transmitted across the crack surface. If enough stress is transmitted across the crack surface, the  $\Delta K_I$  as  $\psi \rightarrow \pi$  may switch from being negative to being positive. Thus if the C.O.D. necessary for crack propagation is small near the crack tip and strains caused by expanding inclusions are large, expanding inclusions near the crack surface and near the crack tip can aid, not hinder, crack propagation. If transformation zones in T-ZrO<sub>2</sub> toughened materials are extremely narrow the M-ZrO<sub>2</sub> may actually assist crack propagation, when in front of and behind the crack.

Toughening from irreversible work due to transformation cracking could be in principle be derived from a local model extended to large arrays of inclusions. All stress fields from inclusions could be summed to get  $\Delta K_{I,II,III}$  and a strain energy release rate could be obtained from irreversible work done during each transformation/microcrack event. Coupled with a local crack extension increment an average strain energy release rate may be obtained. However summation errors due to the approximate nature of the non-rigorous solutions may lead to inaccurate predictions. Additionally much computation time would be involved, especially for modulus difference interactions.

The methods developed in this section are most useful for describing local events. Perhaps a crack bowing through four particles can be modelled successfully using generalized point forces. For transformation/microcrack toughening a zone local to the crack tip using these methods may be imbedded in other zones.

An accurate transformation/microcrack toughening model may contain

the following features:

1. A zone near the crack tip where each microcrack/inclusion is modelled by multiple triples of point forces and near neighbor and next nearest neighbor interactions are allowed.

2. A second zone surrounding the first where each microcrack/inclusion is modelled by a single triplet of point forces, and no interaction is allowed.

3. A third zone surrounding the second, having an average, stress stimulated, volume expansion or elastic moduli difference.

4. The elastic matrix on the outside with the applied stresses. This zone may have an internal stress due to average thermal expansion differences or moduli differences between the matrix and inclusions.

A straight crack front may not adequately model many situations of interest and crack bowing and branching in the first zone may need to be included. Whether a generalized LRNR method of solution can be accurate or fast enough for the two inner zones of this four zone model is open to question.

#### V.E. CONCLUSIONS

1. A model was developed to describe the elastic interaction of a single misfitting spherical inclusion and a straight front crack using three dimensional elasticity and stress superposition. The interaction is obtained in terms of a variation of stress intensity factor ( $\Delta K_I$ ) along the crack front near the inclusion. The basic equations result in double integrals that could not be solved analytically. The results obtained by two different numerical methods for solving the integrals describing the elastic interaction of a single inclusion and a crack are in good

agreement.

2. The results obtained show that a positive  $\Delta K_I$  occurs when a misfitting inclusion with a positive  $\Delta V$  is in front of the crack and a negative  $\Delta K_I$  occurs when the inclusion is above or above and behind the crack. The opposite is true when the inclusion has a negative  $\Delta V$ .

3. When an average elastic modulus for  $\text{ThO}_2\text{-ZrO}_2$  of 240 GPa, an inclusion radius of 0.5 micron and a volume expansion of 3% are used, a single inclusion 1 micron ahead of the crack tip has a maximum positive  $\Delta K_I$  of  $0.14 \text{ MPam}^{1/2}$ . When the inclusion is 1 micron directly above the crack tip a maximum negative  $\Delta K_I$  of  $0.22 \text{ MPam}^{1/2}$  was calculated. These values seem physically realistic.

4. One method developed for solving the double integrals which describe the interaction of a misfitting inclusion and a crack took a minimum of computation time. This method, the limited rapid non-rigorous method (LRNR), was based on interpolating the forms of the desired but analytically unobtainable inner (first) integral from the forms of similar integrals that can be obtained by residue calculus. The outer (second) integrals could then be obtained numerically with a small amount of computation time. The LRNR method can be extended to model multiple inclusion-crack interactions when the moduli of the inclusions are the same as the matrix.

5. The LRNR method can be generalized to at least single microcrack-macrocrack interactions and probably to a much wider class of fracture mechanics problems because of its speed. This wider class might include situations with elastic moduli differences such as: crack bowing between obstacles, crack interaction with limited porosity or inclusions with



different moduli, and perhaps some simple crack branching situations.

6. The effect of the crack opening displacement on the normal and shear stresses that might be transmitted across the crack due to large local strains near misfitting inclusions or other local internal stresses must be included in the modelling of toughening.

## VI. SUMMARY

### VI.A. TOTAL CONCLUSIONS

1. ThO<sub>2</sub>-ZrO<sub>2</sub> ceramic alloys can be prepared over a wide range of compositions 3 m/o ZrO<sub>2</sub> - 46 m/o ZrO<sub>2</sub> at fine ZrO<sub>2</sub> grain sizes, 0.1-0.5 micron.
2. The high temperature tetragonal phase of ZrO<sub>2</sub> can be maintained to room temperature in dense, fine grain sized ThO<sub>2</sub>-ZrO<sub>2</sub> alloys.
3. Fracture toughness of  $K_{IC} > 3 \text{ MPam}^{1/2}$  can be obtained in ThO<sub>2</sub>-ZrO<sub>2</sub> alloys of  $\geq 15$  m/o ZrO<sub>2</sub>, compared to  $K_{IC} \approx 1.6 \text{ MPam}^{1/2}$  for fine grained, dense ThO<sub>2</sub>.
4. Fracture toughness increases in ThO<sub>2</sub>-ZrO<sub>2</sub> with ZrO<sub>2</sub> content (0 m/o - 46 m/o) at a constant ZrO<sub>2</sub> grain size in the range of 0.1-0.3 microns.
5. Fracture toughness can increase then decrease with increasing grain size over the range 0.1 to 0.9 micron, at a constant ZrO<sub>2</sub> content of 15 m/o.
6. At large ZrO<sub>2</sub> grain sizes the toughness of ThO<sub>2</sub>-ZrO<sub>2</sub> is lower than for pure ThO<sub>2</sub>; sometimes spontaneous fracture involving slow crack growth occurs. The ZrO<sub>2</sub> grain sizes at which this occurs decrease from  $>1$  micron for ThO<sub>2</sub>-15 m/o ZrO<sub>2</sub> to  $<0.4$  micron for ThO<sub>2</sub>-46 m/o ZrO<sub>2</sub>.
7. Materials with several percent porosity are less sensitive to spontaneous fracture and to low toughness at large ZrO<sub>2</sub> grain sizes.
8. Evidence was found for toughness increases due to three different mechanisms: near surface compressive stresses due to grinding, compressive stress in a crack tip zone caused by local stress induced transformation, microcracking and multiple cracking or branching.

9.  $\text{ThO}_2$  - 15 m/o  $\text{ZrO}_2$  alloys can be made that have factor of two improvement in fracture toughness over  $\text{ThO}_2$  ( $K_{IC} > 3 \text{ MPam}^{1/2}$ ) and have good optical transmission in the 5-6 micron wavelength range.

10. A 3-dimensional elasticity model has been developed for a crack/misfitting inclusion problem. The methods of solution used have good potential for use in other fracture mechanics problems.

11. The important results for the single expanding inclusion problem are that crack propagation is encouraged when the inclusion is in a zone  $\pm 45^\circ$  ahead of the crack tip and that crack propagation is inhibited by inclusions which are above or behind the crack tip. The results for a contracting sphere are exactly opposite. The effect of the crack opening displacement needs to be added to the model.

12. The tetragonal  $\rightarrow$  monoclinic phase transformation of  $\text{ZrO}_2$  in  $\text{ThO}_2$ - $\text{ZrO}_2$  appears to be nucleation controlled.

13. Under some circumstances there is little if any toughening in  $\text{ThO}_2$  - 15 m/o  $\text{ZrO}_2$  material with fine T- $\text{ZrO}_2$  grains. These materials tend to have narrow size distributions. Some of these materials have  $\text{ZrO}_2$  grain sizes which are large enough to have expected grinding or crack tip stress induced transformation toughening. The lack of toughening may result because a scarcity of nuclei results in very limited transformation or microcracking.

#### VI.B. DISCUSSION

A common theme in materials science research is that properties are the result of structure. Materials structure comes in many size scales and analytical techniques and models must address the correct structure scale controlling the properties of interest to be useful.



Prior to the routine use of SEM and TEM, ZrO<sub>2</sub> bearing alloys of high toughness were not developed, perhaps because the analytical tools available, x-ray diffraction and optical microscopy, were not appropriate for the scale of the structure that could control the properties of the alloys. SEM and quantitative image analysis are probably adequate tools for the task of determining two major structures, ZrO<sub>2</sub> grain size and grain size distribution. Powder processing must advance so that we can vary the ZrO<sub>2</sub> grain size and grain size distribution at will on the 0.05 micron - 10 micron structure scale. Although TEM and in a limited way x-ray diffraction can identify the ZrO<sub>2</sub> phases, normal TEM seems inadequate to the task of finding the nucleation sites for M-ZrO<sub>2</sub>, especially if the sites are in grain boundaries. Improved microscopes, microscopy techniques and data analysis techniques will yield higher resolution in the future, but the average TEM is not suited to the probable scale of the postulated nuclei. A similar problem exists in modelling toughening, the methods used are often unresponsive to the scale necessary for the problem. Two-dimensional elasticity simply cannot model crack bowing between obstacles. Local crack extension events are of paramount importance to the modelling of toughening in ceramics yet models are often developed at too coarse a scale for adequate treatment of the local events.

#### VI.C. SUGGESTIONS FOR FURTHER RESEARCH

Suggestions specific to ThO<sub>2</sub>-ZrO<sub>2</sub> are:

1. Use Raman spectroscopy for ZrO<sub>2</sub> phase identification.
2. Use thermal expansion measurements to detect the average temperatures of transformation.
3. Quantify the ZrO<sub>2</sub> grain size distributions.

4. Use elastic moduli measurements to detect bulk microcracking.
5. Use better precipitation techniques for hydroxide precursors.
6. Quantify the magnitude of the grinding induced surface compressive stresses.

7. Deform  $\text{ThO}_2\text{-ZrO}_2$  alloys at high temperatures to induce lattice dislocations, and non-equilibrium grain boundary structures, perhaps changing the density of nucleation sites, and measure  $K_{IC}$  afterwards.

Suggestions of a general nature for all  $\text{ZrO}_2$  bearing ceramic alloys are:

1. Measure  $K_{IC}$  and strength vs. temperature.
2. Measure the variability in strength.
3. Measure  $\Delta G$  for the M $\rightarrow$ T transformation as a function of composition using the most common "stabilizing" oxides.
4. Control powder processing better.
5. Find the alleged nucleation sites.

Suggestions for the  $\Delta K_I$  calculation include:

1. Develop the generalized  $\Delta K_{I,II,III}$  solution.
2. Develop some specific crack bowing and crack branching problems from the general solution.

## APPENDIX A\*

### I.R. Transmission of ZrO<sub>2</sub> Bearing Alloys

There are three major considerations that can limit the usefulness of two-phase or anisotropic materials for optical purposes; absorption losses, scattering intensity losses and image blurring. The absorption can be extrinsic and can depend on impurities. For a second phase of spherical particles of diameter,  $d$ , the intensity of light transmitted through a thickness  $t$  is:

$$I = I_0 e^{-st} \quad (\text{A.A.1})$$

If  $d \ll \lambda_0$  (Raleigh scattering), the scattering is over a wide angle and the intensity loss is the major consideration. When  $d$ , the absorption coefficients,  $\beta$ , and the difference in refractive indices of the particles,  $n_p$ , and matrix,  $n_m$ , are small the in-line intensity loss can be expressed as (Musikant, 1980):

$$\frac{\Delta I}{I_0} = st = \frac{16\pi^4 x n_m^4}{9} \left(\frac{t}{\lambda_0}\right) \left(\frac{d}{\lambda_0}\right)^3 \left(\frac{\Delta n}{n_m}\right)^2 + \chi \beta_p t + (1-\chi) \beta_m t$$

for  $d/\lambda_0 < 0.2/n_m$  (A.A.2)

where  $\lambda_0$  is the wavelength of light,  $\chi$  the volume fraction of solids. For small non-spherical particles  $\Delta I/I_0 \propto (d/\lambda_0)^m$  where  $m=1,2,3$  for plates, rods and spheres, respectively.

For large particles the scattering is predominant at small angles; image blurring rather than intensity loss is the controlling consideration. Harrison has derived an approximate expression for the mean squared angle of blurring\*\* ; for large particles it is: (Musikant, et al., 1979, 1980):

---

\* Appendix A taken from Cannon, et al. (1982).

\*\*

For small sizes  $\theta_{\text{rms}} \propto (S_c t)^{1/2}$  but the wide angle scattering does not cause blurring.



$$\theta_{\text{rms}} = \left[ \pi \chi \left( \frac{t}{d} \right) \left( \frac{\Delta n}{n_m} \right)^2 \ln (5.15 n_m d / \lambda_o) \right]^{1/2}, \quad d / \lambda_o > 0.3 / n_m \quad (\text{A.A.2})$$

The relative importance of particle size and index difference can be seen in Fig. A.1 in which limiting criteria of  $\Delta I / I_o < 10\%$  for small particles and  $\theta_{\text{rms}} < 0.5^\circ$  for large particles were chosen for illustration. Although many optical systems will require smaller values of  $\theta_{\text{rms}}$  and  $\Delta I / I_o$  than used for Fig. A.1, these values encourage some latitude in searching for new materials, and the plot indicates the required control on particle size. Generally, it will be easier to use fine rather than coarse particles. The advantage to selecting phases having a close match of the refractive indices is apparent.

The intensity loss expression, Eq. (A.A.1), for isotropic, stress-free, spherical particles for which  $d < \lambda_o / 5n_m$ , should be satisfactory guide to initial materials selection and design. There are a few further complications including the effect of stresses which must be considered particularly if  $\Delta n$  is small. For quantitative treatments the effect of the particle size distribution must be considered; the effective particle size describing the scattering will be larger than the modal size. Further, if non-spherical particles are aligned or spheres are regularly spaced, then diffraction effects or non-random scattering may cause false signals in the background. When  $\Delta n$  is sufficiently small, then for particle sizes near the wavelength the scattering is relatively small. For this case a combination of intensity loss and blurring considerations will be important. The criteria relating scattering behavior to optical performance have not been fully worked out yet for this situation, and it may be necessary to consider multiple scattering to do so.

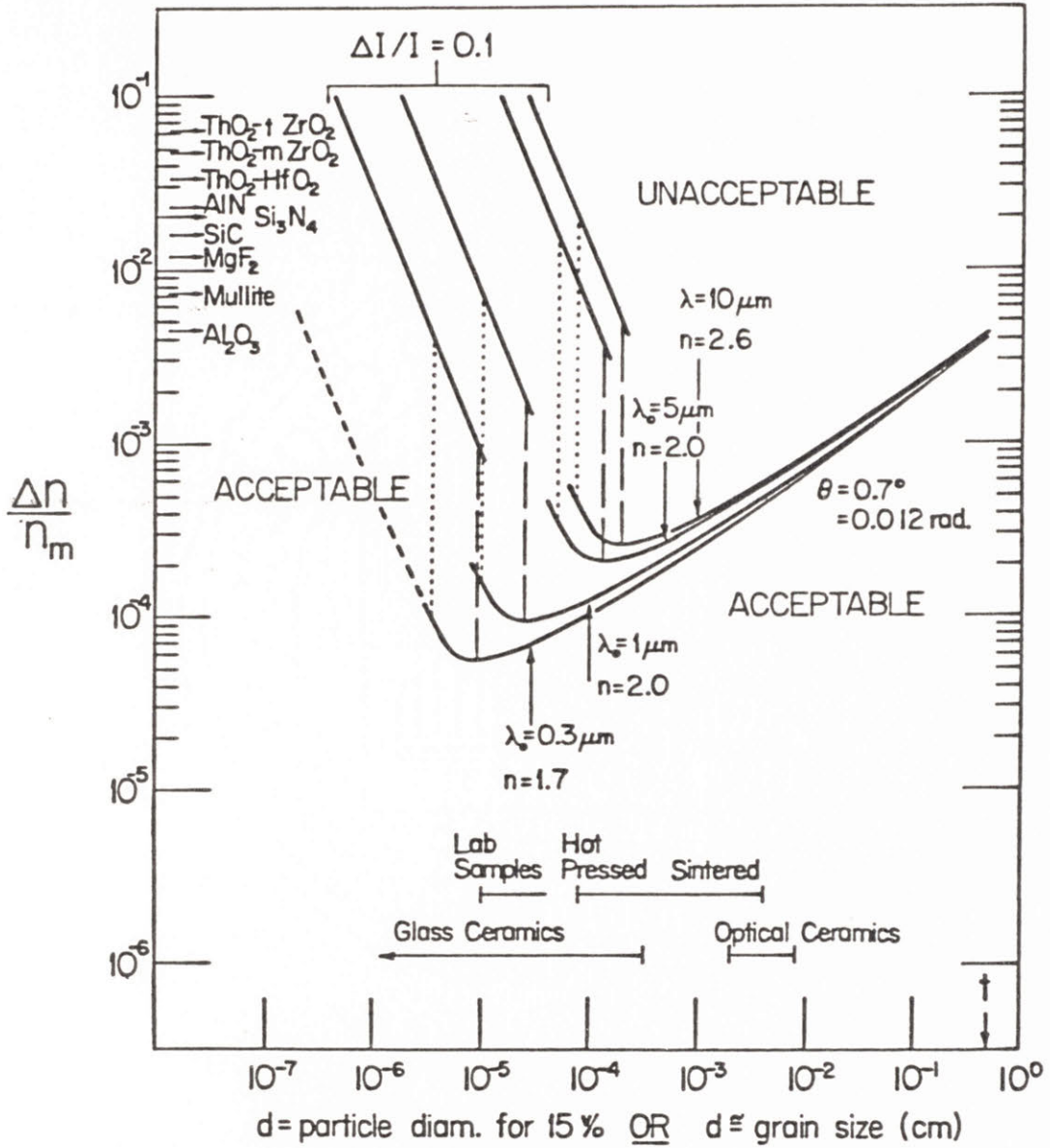


Figure A.A.1 Plot of the required refractive index match as a function of particle size. At small particle sizes, the intensity loss is the controlling feature; whereas at large sizes, reducing blurring is most important. Grain sizes typically obtained by conventional processing techniques are also shown.

Toughening using  $ZrO_2$  is particularly suitable for optical materials; the strengths and toughness are very high; the required particle sizes are small,  $d < 1 \mu m$ ; and several opportunities exist with different matrices to alloy to improve and control the refractive index match and the particle size for peak toughness. Preliminary work using  $ThO_2 + ZrO_2$  indicates toughening and useful optical properties should be achievable for some IR wavelengths, Fig. A.A.2. With  $d < 1 \mu m$ , the toughness and scattering increase with particle size; the transmission losses for the two materials with 15%  $ZrO_2$  and  $d \sim 0.5-1 \mu m$  are approximately described by Eq. (A.A.2) assuming scattering due only to the  $ZrO_2$  particles,  $\Delta n/n \sim 4\%$ . These curves also reveal processing problems with entrapped carbon which result from the need for submicron grains and high density, which can also exist for sintered materials, and which require special attention. The data in Figs. IV. 5 & 9 and A.A.2 and Eq. (A.A.1) suggest higher  $ZrO_2$  contents with finer particle sizes should cause less scattering (the  $\chi d^3$  term is smaller) at comparable toughnesses.

The combined scattering and absorption of the  $ZrO_2$  toughened materials is within a factor of ten of being useful at some wavelengths, and further improvements and extension of the useful range of wavelengths should be possible. Two materials offering the prospect of good index matching are  $ThO_2 + (Zr,Hf)O_2$  and  $(Al,Cr)_2O_3 + ZrO_2$ . The latter presents processing difficulties, is not transparent at optical wavelengths due to Cr absorption, but could have very high toughness, strength, and hardness. Since alloying with  $HfO_2$  should lower  $\Delta n/n$  with  $ThO_2$  and the particle size for peak toughening,  $ThO_2 + (Zr,Hf)O_2$



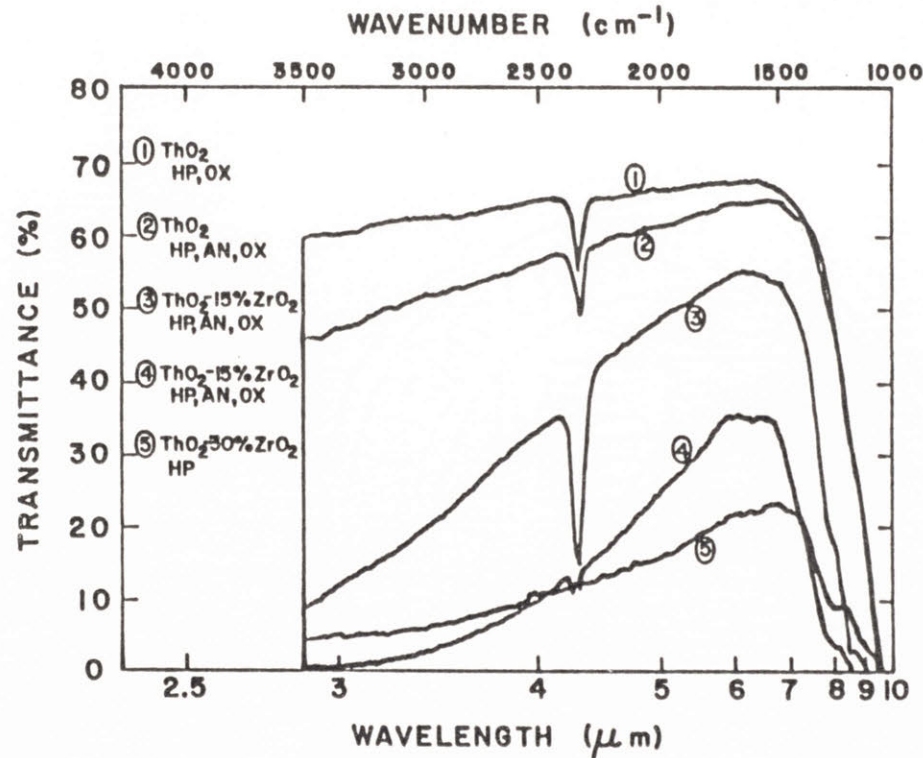


Figure A.A.2 IR transmission of hot pressed  $\text{ThO}_2$  and  $\text{ThO}_2+\text{ZrO}_2$ . Data taken by inline transmission with a Digilab FTS. The 15% materials were annealed to increase the  $\text{ZrO}_2$  size prior to oxidation. Curves 1 and 2 illustrate increased scattering from pore coarsening from such treatment. The  $\text{ZrO}_2$ ,  $d \sim 0.5-1 \mu\text{m}$  causes scattering, particularly at smaller  $\lambda$ . The larger  $\text{ZrO}_2$  size in 4 gives higher  $K_c$  and scattering than in 3. Unoxidized material, 5, has low transmission, primarily due to higher absorption; the finer  $\text{ZrO}_2$   $d < 0.2 \mu\text{m}$  should cause less scattering than in 3 or 4. The  $4.3 \mu\text{m}$  absorption (absent in 5) is from  $\text{CO}_2$  in ultrafine pores caused by oxidation of C entrapped during hot pressing. The C is probably residue from surface reactions of organic solvents used during powder preparation.  $t = 1.57, 1.09, 0.93, 1.69, 0.74 \text{ mm}$  for 1-5, respectively.

Table A.1. Comparison of Scattering/Absorption Coefficient and Mechanical Properties in Toughened and Matrix Materials

Material	Condition	$\lambda$ , $\mu\text{m}$	$S^*$ , $\text{cm}^{-1}$	$K_c$ $\text{MN/m}^{3/2}$	H, GPa
Thoralox <sup>®</sup>	sintered	6	0.44 <sup>Ⓐ</sup>	~1.6	
		3	1.3 <sup>Ⓐ</sup>		
ThO <sub>2</sub>	hot-pressed & oxidized	6	0.79	1.6	10.4
		3	1.6		
ThO <sub>2</sub>	hot-pressed, annealed & oxidized	6	1.7	1.6	
		3	4.5		
ThO <sub>2</sub> +15% ZrO <sub>2</sub>	hot-pressed, aged & oxidized	6	3.6	3.5	9.5
		3	20		
ThO <sub>2</sub> +15% ZrO <sub>2</sub>	hot-pressed, aged & oxidized	6	4.7	3.9	9.4
		3	26		
ThO <sub>2</sub> +30% ZrO <sub>2</sub>	hot-pressed	6	18	~3	10
		3	33		
AlCrO <sub>3</sub> +40% ZrO <sub>2</sub>	hot-pressed	6	92	6.6	14.5
		3	$\infty$ -165		
AlCrO <sub>3</sub> +40% ZrO <sub>2</sub>	hot-pressed & air annealed	6	270	~6.9	12.9
		3	$\infty$ -542		
Mullite+20% ZrO <sub>2</sub>	hot-pressed	-	--	4.5	10.9

\* From single thickness transmission measurements. Corrected for reflection losses,  $I/I_0 (I-R)^2$ ,  $R = (n-1/n+1)^2$  using optical values of n. Calculated by R.M. Cannon.

<sup>Ⓐ</sup> Measurements at GE-RESO.

could be transparent from 7  $\mu\text{m}$  to near IR or smaller  $\lambda$  over a wide temperature range. Mullite +  $\text{ZrO}_2$  should have very good thermal shock resistance; however, the index mismatch is too large for use at IR wavelengths, but it would be useful for radar windows.



## APPENDIX B

### Other ZrO<sub>2</sub> Toughened Alloys

Three other ZrO<sub>2</sub> bearing ceramic alloys were produced; AlCrO<sub>3</sub>-ZrO<sub>2</sub>, ThO<sub>2</sub>-(Zr,Hf)<sub>1</sub>O<sub>2</sub> and 3Al<sub>2</sub>O<sub>3</sub>·2SiO<sub>2</sub>-ZrO<sub>2</sub>. First two contain solid solutions of Al<sub>2</sub>O<sub>3</sub>-Cr<sub>2</sub>O<sub>3</sub> and ZrO<sub>2</sub>-HfO<sub>2</sub> respectively that in principle can match the index of refraction of the other oxides, ZrO<sub>2</sub> or ThO<sub>2</sub>. The AlCrO<sub>3</sub>-ZrO<sub>2</sub> and ThO<sub>2</sub>-(Zr,Hf)<sub>1</sub>O<sub>2</sub> were produced by hydroxide precipitation similar to the method described in Section III. The AlCrO<sub>3</sub>-40 v/o ZrO<sub>2</sub> was hot pressed at 1500°C for 1/2 hr. at 34 MPa. An Al<sub>2</sub>O<sub>3</sub> rich 3Al<sub>2</sub>O<sub>3</sub>·2SiO<sub>2</sub> (mullite) submicron particle size powder was supplied by Svante Prochazka\*, 20 v/o of unstabilized submicron ZrO<sub>2</sub> powder added and vibromilled with stabilized ZrO<sub>2</sub> media for 20 hrs. The 3Al<sub>2</sub>O<sub>3</sub>·2SiO<sub>2</sub>-20 v/o ZrO<sub>2</sub> was hot pressed at 1525°C for 1/2 hr. at 34 MPa. SEM examination did not reveal any porosity in either hot pressed sample. After diamond polishing the microhardness K<sub>IC</sub>'s and H's were 6.6 MPa m<sup>1/2</sup> and 14.5 GPa for AlCrO<sub>3</sub>-40 v/o ZrO<sub>2</sub> and 4.5 MPa m<sup>1/2</sup>, and 11 GPa for 3Al<sub>2</sub>O<sub>3</sub>·2SiO<sub>2</sub>-20 v/o ZrO<sub>2</sub>. The AlCrO<sub>3</sub>-ZrO<sub>2</sub> was extremely difficult to polish due to the high hardness and high K<sub>IC</sub>. The 3Al<sub>2</sub>O<sub>3</sub>·2SiO<sub>2</sub>-ZrO<sub>2</sub> had a very good thermal shock resistance and good bend strength, σ<sub>f</sub> = 314 MPa (Musikant et al., 1980).

The ThO<sub>2</sub>-20 m/o (Zr<sub>.6</sub>Hf<sub>.4</sub>)O<sub>2</sub> was densified by sintering. The isostatically pressed green body was preferred in air at 900°C for 15 min. after a slow heating (> 4 hrs.) from room temperature to eliminate organics. The ThO<sub>2</sub>-20 m/o (Zr<sub>.6</sub>Hf<sub>.4</sub>)O<sub>2</sub> was sintered for 1/2 hr. at 1500°C and 1/2 hr. at 1600°C in high purity dried H<sub>2</sub>. A density of 97%

---

\*General Electric Corp. Research and Development Center, Schenectady, N.Y.

theoretical was achieved.  $(\text{Zr,Hf})\text{O}_2$  grain sizes for the  $\text{ThO}_2-(\text{Zr,Hf})\text{O}_2$  were under 0.5 micron. Several small ( $\sim 1$  mm) dense patches within the sintered material were translucent after oxidation at  $\sim 1200^\circ\text{C}$ . The fine particle size of the  $\text{ThO}_2-(\text{Zr,Hf})\text{O}_2$  powder allowed large amounts of water absorption to occur. Isostatically cold pressed samples expanded by 3x in volume during rapid heating after one week at R.T. and high humidity.

APPENDIX C

Mathematical Details for Section V

App. C.1 Fourier Series Method,  $\eta$  integration (Hildebrand 1976).

i.  $A_0$

Using upper half of complex plane with  $\eta$  complex,

$$\int_{-\infty}^{\infty} \frac{1}{Q^2 + \eta^2} \cdot A_0 d\eta = A_0 \cdot 2\pi i [\text{res. at } iQ] = A_0 \cdot 2\pi i [2iQ]^{-1} = A_0 \cdot \pi/Q \quad (\text{A.C.1})$$

ii.  $A_n, B_n$

$$\int_{-\infty}^{\infty} A_n \frac{\cos 2n(\tan^{-1} \eta)}{Q^2 + \eta^2} d\eta = A_n \text{ Real } I_3 \quad (\text{A.C.2})$$

$$\int_{-\infty}^{\infty} B_n \frac{\sin 2n(\tan^{-1} \eta)}{Q^2 + \eta^2} d\eta = B_n \text{ Imag. } I_3 \quad (\text{A.C.3})$$

$$I_3 = \int_{-\infty}^{\infty} \frac{e^{i2n[1/2i \ln i-n/1+n]}}{Q^2 + \eta^2} d\eta = \int_{-\infty}^{\infty} \frac{1}{Q^2 + \eta^2} \left[ \frac{i-\eta}{i+\eta} \right]^n d\eta \quad (\text{A.C.4})$$

$$I_3 = 2\pi i [\text{Res in upper half plane (i.e., } iQ)] \quad (\text{A.C.5})$$

$$I_3 = \frac{2\pi i}{2Qi} \left[ \frac{i(1-Q)}{i(1+Q)} \right]^n = \frac{\pi}{Q} \left[ \frac{1-Q}{1+Q} \right]^n \quad (\text{A.C.6})$$

and

$$\text{Real } I_3 = \pi/Q \left[ \frac{1-Q}{1+Q} \right]^n \quad (\text{A.C.7})$$

$$\text{Imag. } I_3 = 0 \quad (\text{A.C.8})$$

$$\text{and with } Q = \tan \beta \quad (\text{A.C.9})$$

we have Eq. (V.17).



A.C.2 Integrals of the form  $\int_0^{\infty} r^{-1/2} [r^2 + Ar + B]^{-1, -2, -3} dr$

With  $r$  complex using contour in Figure A.C.1

$$\int_0^{\infty} r^{-1/2} [r^2 + Ar + B]^{-1, -2, -3} dr = \pi i [\text{residue at } r^2 + Ar + B = 0] \quad (\text{A.C.10})$$

$$\begin{aligned} \int_0^{\infty} r^{-1/2} [r^2 + Ar + B]^{-1} dr &= \frac{\pi i}{2} \left\{ \frac{1}{i} \left[ B - \frac{A^2}{4} \right]^{-1/2} \left[ -\frac{A}{2} + i \left( B - \frac{A^2}{4} \right)^{1/2} \right]^{-1/2} \right. \\ &\quad \left. - \frac{1}{i} \left[ B - \frac{A^2}{4} \right]^{-1/2} \left[ -\frac{A}{2} - i \left( B - \frac{A^2}{4} \right)^{1/2} \right]^{-1/2} \right\} \quad (\text{A.C.11}) \end{aligned}$$

Using Figure A.C.2

$$\left[ -\frac{A}{2} + i \left( B - \frac{A^2}{4} \right)^{1/2} \right]^{-1/2} = [B]^{-1/2} e^{-i \phi_1 / 2} \quad (\text{A.C.12a})$$

$$\left[ -\frac{A}{2} - i \left( B - \frac{A^2}{4} \right)^{1/2} \right]^{-1/2} = [B]^{-1/2} e^{-i \phi_2 / 2} \quad (\text{A.C.12b})$$

but

$$\phi_2 = 2\pi - \phi_1 \quad (\text{A.C.12c})$$

thus

$$\int_0^{\infty} r^{-1/2} [r^2 + Ar + B]^{-1} dr = \frac{\pi [e^{i \phi_1 / 2} + e^{-i \phi_1 / 2}]}{[B^2]^{1/4} [B - A^2/4]^{1/2}} \quad (\text{A.C.13a})$$

$$= \frac{\pi \cos(\phi_1 / 2)}{[B^2]^{1/4} [B - A^2/4]^{1/2}} \quad (\text{A.C.13b})$$

$$\phi_1 = \cos^{-1} \left[ -\frac{A}{2[B]^{1/2}} \right] \quad (\text{A.C.13c})$$

The integrals

$$\int_0^{\infty} r^{-1/2} [r^2 + Ar + B]^{-2, -3} dr$$

are solved in a similar manner. The integrals  $\int_0^{\infty} r^{-1/2} [r^2 + Ar + B]^{-1, -2} dr$

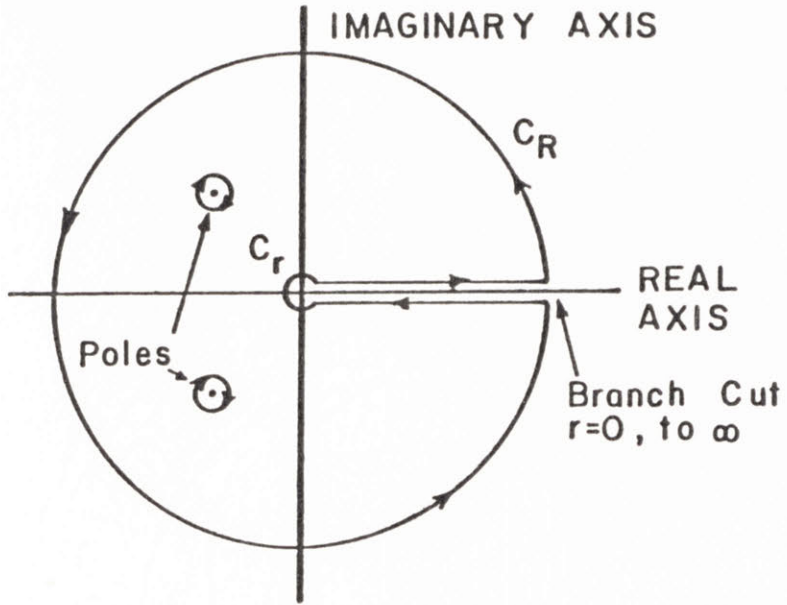


Figure A.C.1 Contour for complex residue integrals A.C.10 a & b.  
 $C_R$  and  $C_r$  do not contribute to the result.

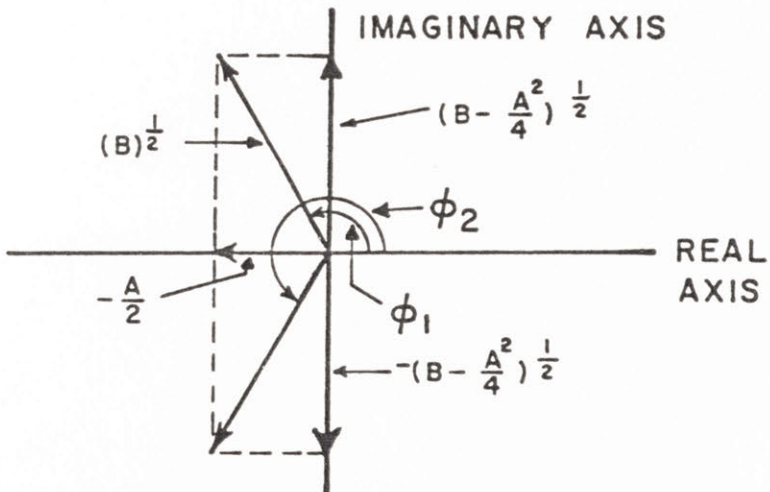


Figure A.C.2 Vector representation of equations A.C.12 a & b.

are also available from tables in slightly different forms, Gradshteyn and Ryzhik.

A.C.3 Maximum possible for Eqs. (V.24a) and (V.24b).

As  $\theta$  approaches  $\pi/2$

$$[r^2 + 2rx_0 \sin\theta + x_0^2]^{1/2} = r+x_0 \tag{A.C.14}$$

and Eqs. (24a) and (24b) useless.

By inspection the integrals

$$\int_{-\infty}^{\infty} \int_0^{\infty} \frac{(\gamma)^{1/2}}{(\gamma)^2 + (z+\alpha)^2} [y_0^2 + \alpha^2 + (\gamma+x_0)^2]^{-3/2, -5/2} d\gamma d\alpha \tag{A.C.15}$$

are maximum when  $z=0$  with  $y_0, x_0$  constant. When  $x_0 \geq 0$

$$\int_0^{\infty} r^{-1/2} [r^2 + 2rx_0 \sin\theta + x_0^2 + y_0^2]^{-3/2, -5/2} dr \leq \int_0^{\infty} r^{-1/2} [r^2 + x_0^2 + y_0^2]^{-3/2, -5/2} dr \tag{A.C.16a}$$

when  $0 < \theta < \pi$

But

$$\int_0^{\infty} r^{-1/2} [r^2 + m]^{-c} dr = \frac{1/4 - c}{2} \left[ \frac{\Gamma(\frac{1}{4}) \Gamma(c - \frac{1}{4})}{\Gamma(c)} \right] \tag{A.C.17}$$

If  $c$  can be extended to non-integers (C.R.C. Math. Tables ). As  $\theta$  approaches  $\pi/2$  Eqs. (24a) and (24b) pass this maximum possible value, then we used Eq. (A.C.17) instead of Eqs. (24a) and (24b) for the particular range of  $\theta$  involved.



A.C.4 Taylor Series estimate near  $\theta = \pi/2$  when  $x_0 \geq 0$

For the integral

$$I_4 = \int_0^\infty \int_{\theta_1}^{\theta_2} r^{-1/2} (\sin\theta)^{1/2} [r^2 + 2r(-z\cos\theta + x_0 \sin\theta) + x_0^2 + y_0^2 + z^2]^{-3/2} d\theta dr \quad (\text{A.C.18})$$

when  $\phi_1 < \pi/2 < \theta_2$  and  $\theta_1, \theta_2$  are near  $\pi/2$ , first develop a Taylor series around  $\theta = \pi/2$

$$I_{\text{Taylor}} = \int_0^\infty \int_{\theta_1}^{\theta_2} \{ (r^{-1/2} [r^2 + 2x_0 r + x_0^2 + y_0^2 + z^2]^{-3/2}) \cdot$$

$$\{ 1 + -\frac{1}{2} (\theta - \pi/2)^2 \} + r^{-1/2} [r^2 + 2x_0 r + x_0^2 + y_0^2 + z^2]^{-5/2} \cdot$$

$$\{ -\frac{3}{2} z(\theta - \pi/2) + -\frac{3}{2} x_0 (\theta - \pi/2)^2 \} +$$

$$\frac{15}{4} z^2 r^{-1/2} [r^2 + 2x_0 r + x_0^2 + y_0^2 + z^2]^{-7/2} \} d\theta dr$$

+ higher order terms

(A.C.19)

Now the  $\theta$  integration is trivial. If  $(x_0/a)^2 \gg (y_0/a)^2 + (z/a)^2$

then

$$[r^2 + 2rx_0 + x_0^2 + y_0^2 + z^2]^{-1/2} \sim (r + \sqrt{B})^{-1}$$

where  $B = x_0^2$  or  $x_0^2 + y_0^2 + z^2$ .

Now the  $r$  integration is also easy. The value for  $B$  is determined by the sign of the constants after the  $\theta$  integration, since we wish to find a maximum possible for  $I_{\text{Taylor}}$ .  $\theta_1$  and  $\theta_2$  can be determined initially as

in Section A.C.3 or directly from the value of  $I_{\text{Taylor}}$  after the  $r$  integration but before  $\theta$  integration.

The integral

$$\int_0^\infty \int_{\theta_1'}^{\theta_2'} r^{-1/2} [\sin\theta]^{1/2} \cdot [r^2 + 2r(-z\cos\theta + x_0\sin\theta) + x_0^2 + y_0^2 + z^2]^{-5/2} dr d\theta$$

can be approximated for the same conditions on  $\theta$ ,  $x_0$ ,  $y_0$ , and  $z$  in a similar manner. Taylor series often need many terms to be accurate however.

#### A.C.5 Branch points and moving poles

Analytical expressions for the integrals

$$\int_0^\infty r^{-1/2} (r^2 + Ar + B)^{-3/2, -5/2} dr$$

could not be obtained. In the complex plane the integrals contain 3 branch points, one at  $r=0$ , and two at the solutions to  $r^2 + Ar + B = 0$ . Any change of variables that eliminated two branch points at  $r^2 + Ar + B = 0$  also lead to cancellations of the integrals along any reasonable contour. As  $r^2 + Ar + B$  approaches  $[r \pm \sqrt{B}]^2$  the two branch points combine to form a single pole, and the integral is easily done. This was utilized in Section A.C.4. When integrating Eqs. (V.23), however, two poles combine to form a single higher order pole. This causes difficulties not only in Eqs. (V.23a - c), but also in Eqs. (V.24a) and (V.24b) because the form of Eqs. (V.24a) and (V.24b) are derived from the form of Eqs. (V.23a-c).

$r^2 + Ar + B$  approaches  $[r \pm \sqrt{B}]^2$  in several situations.  $\theta \rightarrow \pi/2$  when  $(x_0/a)^2 \gg (y_0/a)^2 + (z/a)^2$ ;  $\theta \rightarrow 0$  or  $\theta \rightarrow \pi$  when  $(z/a)^2 \gg (x_0/a)^2 + (y_0/a)^2$ . However, when  $x_0/a < 0$  then  $(y_0/a)^2 \geq 1$  and  $(x_0/a)^2 + (y_0/a)^2 \geq 1$

no matter what  $z/a$  is. Hence, except for  $\theta \rightarrow \pi/2$ ,  $x_0/a \geq 0$  and  $(x_0/a)^2 + (y_0/a)^2 + (z/a)^2$  the poles are separated by at least  $2i$  across the real axis. Thus Eqs. (V.24a) and (V.24b) may only be wrong by perhaps a factor of 2 or 3 in most cases. As  $\theta$  approaches 0 or  $\pi$  the factor of  $(\sin\theta)^{1/2}$  eliminates any problems when  $(z/a)^2 \gg (x_0/a)^2 + (y_0/a)^2$ . This leaves only  $x_0/a < 0$ ,  $(x_0/a)^2 \gg (y_0/a)^2 + (z/a)^2$  to be analyzed, as  $x_0/a \geq 0$  has been dealt with in Sections A.C.3 and A.C.4.



## BIBLIOGRAPHY

- Anderson, C.A. and T.K. Gupta (1981), "Phase Stability and Transformation Toughening in Zirconia", in Advances in Ceramics, vol. 3, Amer. Ceram. Soc., Inc., 1981, pp. 184-201.
- Anstis, G.R., P. Chantikul, B.R. Lawn and D.B. Marshall (1981) "Critical Evaluation of Indentation Techniques for Measuring Fracture Toughness: I. Direct Crack Measurements," J. Amer. Ceram. Soc., vol. 64, No. 9, pp. 533-538.
- Bannister, M.J. (1968), "Equivalence of X-ray and Electron Microscopy Crystalite Sizes in Thoria Gel," *ibid.*, vol. 51, No. 4, pp. 228-229.
- Bannister, M.J. (1975), "Sintering Mechanisms in Thoria Gel," *ibid.*, vol. 58, No. 1-2, pp. 10-14.
- Bansal, G.K. and A.H. Heuer (1972), "On a Martensitic Phase Transformation in Zirconia ( $ZrO_2$ ), I. Metallographic Evidence," *Acta Metl*, vol. 20 No. 11, pp. 1281-89.
- Bansal, G.K. and A.H. Heuer (1974), "On a Martensitic Phase Transformation in Zirconia ( $ZrO_2$ ). II. Crystallographic Aspects," *ibid.*, vol. 22 No. 4, pp. 409-417.
- Becher, P.F. (1981), "Transient Thermal Stress Behavior in  $ZrO_2$ -Toughened  $Al_2O_3$ ," J. Amer. Ceram. Soc., vol. 1, 64, No. 1, pp. 37-39.
- Bender, B.A. and R.P. Ingel (1981), "Microscopy of PSZ Single Crystals," J. Amer. Ceram. Soc., vol. 64, No. 6, Back cover.
- Bender, C.M. and S.A. Orszag (1978), "Advanced Mathematical Methods for Scientists and Engineers," Chapter 6, McGraw-Hill, N.Y., 1978.
- Bhat, D.G. (1981), "Comment on Elastic/Plastic Indentation Damage in Ceramics: The Median/Radial Crack System," *Commun. Amer. Ceram. Soc.*, Nov. 1981, pp. C-165, in J. Amer. Ceram. Soc., vol. 64, No. 11.
- Bratton, R.J. and S.K. Lau (1981), "Zirconia Thermal Barrier Coatings," in Advances in Ceramics, Vol. 3, Amer. Ceram. Soc., Inc., 1981, pp. 226-240.
- Brook, R.J. (1981), "Preparation and Electrical Behavior of Zirconia Ceramics," in *ibid.*, pp. 272-285.
- Cannon, Jr., R.M., T.D. Ketcham and T.W. Coyle, "Toughened Optical Materials," to be published, SPIE Proceedings on Emerging Optical Materials.

- Cannon, Jr., R.M. (1981), personal communication.
- Carniglia, S.C., S.D. Brown and Schroeder, T.F. (1971), "Phase Equilibria and Physical Properties of Oxygen-Deficient Zirconia and Thoria," J. Amer. Ceram. Soc., vol. 54, No. 1, pp.13-17.
- Claussen, N. and M. Ruhle (1981), "Design of Transformation Toughened Ceramics," in Advances in Ceramics, vol. 3, Amer. Ceram. Soc., Inc. 1981, pp. 137-163.
- Claussen, N. (1978), "Stress-Induced Transformation of Tetragonal  $ZrO_2$  Particles in Ceramic Matrices," J. Amer. Ceram. Soc., vol. 61, Nos. 1-2, pp. 85-86.
- Claussen, N., J. Steeb and R.F. Pabst (1977), "Effect of Induced Microcracking on the Fracture Toughness Ceramics," Bull. Amer. Ceram. Soc., vol. 56, No. 6, pp. 559-562.
- Claussen, N. (1976), "Fracture Toughness of  $Al_2O_3$  with an Unstabilized  $ZrO_2$  Dispersed Phase," J. Amer. Ceram. Soc., vol. 59, Nos.1-2, pp. 49-51.
- Coble, R.L. (1970), "Diffusion Models for Hot Pressing with Surface Energy and Pressure Effects as Driving Forces," J. Appl. Phys., vol. 41, No.12, pp. 4798-4807.
- Cohen, M. and C.M. Wayman (1981), "Fundamentals of Martensitic Reactions," to be published in Treatises in Metallurgy, Tein and Elliott, Eds.
- Coughlin, J.P., and E.G. King (1950), "High Temperature Heat Contents of some Zirconium Containing Substances," J. Amer. Chem. Soc., vol. 72, No. 5, pp. 2262-2265.
- C.R.C. Standard Mathematical Tables, 22 ed., S.M. Selby Ed., The Chemical Rubber Co., 1974.
- Cullity, B.D. (1956), "Elements of X-ray Diffraction," Addison-Wesley 1956, pp. 468.
- Cutler, I.B. (1976), personal communication.
- Dole, S.L., R.S. Scheidenker, L.E. Shiers, M.F. Berard and O. Hunter, Jr. (1978a), "Technique for Preparing Highly-Sinterable Oxide Powders," Mat. Sc. and Eng., vol. 32, No. 3, pp. 277-281.
- Dole, S.L., O. Hunter, Jr., F.W. Calderwood and D.J. Bray (1978b), "Microcracking in Monoclinic  $HfO_2$ ," J. Amer. Ceram. Soc., vol. 61, Nos.11-12, pp. 486-490.
- Duwez, P. and E. Loh (1957), "Phase Relationships in the System Zirconia-Thoria," Ibid., vol. 40, No.9, pp. 321-324.



- Evans, A.G., and R. McMeeking (1982), to be published.
- Evans, A.G., Marshall, D.B. and N.H. Burlingame (1981a), "Transformation Toughening in Ceramics," in Advances in Ceramics, vol. 3, The Amer. Ceram. Soc., Inc., 1981, pp. 202-214.
- Evans, A.G., N. Burlingame, M. Drory and W.M. Kriven (1981b), "Martensitic Transformations in Zirconia: Particle Size Effects and Toughening," *Acta Met.*, vol. 29, No. 2, pp. 447-456.
- Evans, A.G., and K.T. Farber (1981), "Toughening of Ceramics by Circumferential Microcracking," *J. Amer. Ceram. Soc.*, vol. 64, No. 7, pp. 394-398.
- Evans, A.G. and A. H. Heuer (1980), "Preview-Transformation Toughening in Ceramics; Martensitic Transformations in Crack-tip Stress Fields," *ibid.*, vo. 63, No. 5-6, pp. 241-248.
- Evans, A.G., A.H. Heuer and D.L. Porter, "The Fracture Toughness of Ceramics," in Fracture, 1977, vol. 1, ICF4, pp. 529-556.
- Evans, A.G. and T.G. Langdon (1976), "Structural Ceramics," *Progress in Materials Science*, vol. 21, No.3-4, pp. 171-441.
- Evans, A.G. and E.A. Charles (1976), "Fracture Toughness Determinations by Indentation," *J. Amer. Ceram. Soc.*, vol. 59, No.7-8, pp.371-372.
- Evans, A.G. (1972), "The Strength of Brittle Materials Containing Second Phase Dispersions," *Phil. Mag.*, vol. 183, No. 26, pp. 1327-1344.
- Fehrenbacher, L.L. and L.A. Jacobson (1965), "Metallographic Observation of the Monoclinic-Tetragonal Phase Transformation in  $ZrO_2$ ," *ibid.*, vol. 48, No. 3, pp.157-161.
- Furgeson, D.E., O.C. Dean and D.H. Douglas (1964), "Sol-Gel Process for the Remote Preparation and Fabrication of Recycle Fuels," in *Proceedings of the 3rd International Conference of Peaceful Uses of Atomic Energy*, vol. 10, 1965; published in 1965, pp. 307-313.
- Garvie, R.C. (1965), "The Occurrence of Metastable Tetragonal Zirconia as a Crystalline Size Effect," *J. Phys. Chem.*, vol. 69, No.4, pp. 1338-1243.
- Garvie, R.C., R.H. Hannink and R.T. Pascoe (1975), "Ceramic Steel?," *Nature (London)*, vol. 258, pp. 703-704.
- Garvie, R.C., R.R. Hughan, and R.T. Pascoe (1978), "Strengthening of Lime-Stabilized Zirconia by Post Sintering Heat Treatment," in *Processing of Crystalline Ceramics*, ed., H. Palour III, R.F. Davis and T.M. Hare, Plenum Press, 1978, pp. 263-273.



- Garvie, R.C., R.H.J. Hannink and C. Urbani (1980), "Fracture Mechanics Study of a Transformation Toughened Zirconia Alloy in the CaO-ZrO<sub>2</sub> System," *Ceramurgia Intern.*, vol. 6, No.1, pp. 19-24.
- Gradshteyn, I.S. and I.M. Ryzhik (1965), "Table of Integrals, Series and Products," 4th ed., Academic Press, N.Y., 1965.
- Grain, C.F. (1967), "Phase Relations in the ZrO<sub>2</sub>-MgO System," *J. Amer. Ceram. Soc.*, vol. 50, No.6, pp. 288-290.
- Green, D.J., and P.S. Nicholson, "Fracture of Brittle Particular Composites," in Fracture Mechanics of Ceramics, vol. 4, Plenum Press, N.Y., pp. 945-960.
- Green, D.J., P.S. Nicholson and J.D. Embury (1973), "Fracture Toughness of a Partially Stabilized ZrO<sub>2</sub> in the System CaO-ZrO<sub>2</sub>," *ibid.*, vol. 56, No. 12, pp. 619-623.
- Greenleaf, F.P. (1972), "Introduction to Complex Variables," W.B. Saunders Co., Philadelphia, 1972.
- Griffith, A.A. (1920), "The Phenomena of Rupture and Flow in Solids," *Phil. Trans. Roy. Soc.*, London, vol. A.221, pp. 163-198.
- Gupta, T.K. (1980), "Strengthening by Surface Damage in Metastable Tetragonal Zirconia," *J. Amer. Ceram. Soc.*, vol. 63, No.1-2, pp. 117.
- Gupta, T.K., J.H. Bechtold, R.C. Kuzunick, L.H. Cadoff and B.R. Rossing (1977), "Stabilization of Tetragonal Phase in Polycrystalline Zirconia," *J. Matls. Sc.*, vol. 12, pp. 2421-2426.
- Haberko, K. (1979), "Characteristics and Sintering Behavior of Zirconia Ultrafine Powders," *Ceramurgia Int.*, vol. 5, No. 4, pp. 148-154.
- Hannink, R.H.J. (1978), "Growth Morphology of the Tetragonal Phase in Partially Stabilized Zirconia," *J. Matls. Sc.*, vol. 13, pp. 2487-2496.
- Henrici, P. (1974), "Applied and Computational Complex Analysis," vol. 1, J. Wiley and Sons Inc. 1974.
- Heuer, A.H., N. Claussen, W. Kriven, and M. Ruhle (1982), "The Stability of Tetragonal ZrO<sub>2</sub> particles in Ceramic Matrices," to be published.
- Heuer, A.H. and L.W. Hobbs (1981), editors of "Science and Technology of Zirconia," The American Ceramic Society, Inc., Columbus, Ohio, 1981, vol. 3 of Advances in Ceramics.
- Hildebrand, F.B. (1976) "Advanced Calculus for Applications," 2nd ed., Prentice Hall Inc., 1976, chapters 10 & 11.
- Hildebrand, F.B. (1974), "Introduction to Numerical Analysis," 2nd ed., McGraw-Hill, N.Y., 1974, pp. 478.

- Hoagland, R.G. and J.D. Embury (1980), "A Treatment of Inelastic Deformation Around a Crack Tip due to Microcracking," J. Amer. Ceram. Soc., vol. 63 No.7-8, pp. 404-410.
- Hong, B. and R.L. Coble (1981), personal communications.
- Hull, D. (1969), "Introduction to Dislocations," Pergamon Press, Oxford, 1969, pp. 99.
- Hulse, C.O. (1978), "Mechanical Properties of  $\text{Al}_2\text{O}_3\text{-HfO}_2$  Eutectic Microstructures," in Fracture Mechanics of Ceramics, vol. 4, ed., by R.C. Bradt, D.P.H. Hasselman and F.F. Lange, Plenum Press, N.Y., 1978, pp. 903-912.
- Hutchinson, J. (1982), to be published.
- Inoue, T. and H. Matzke (1981), "Temperature Dependence of Hertzian Fracture Surface Energy of  $\text{ThO}_2$ ," J. Amer. Ceram. Soc., vol. 64, No. 6, pp. 355-360.
- Irwin, G.R. (1957), "Analysis of Stresses and Strains Near the End of a Crack Traversing a Plate," J. Appl. Mech., vol. 24, No.3, pp. 361-364.
- J.A.N.F. Thermodynamical Tables 2nd ed., D.R. Stull and H. Prophet, ed. Dow Chemical Co., Thermal Research Laboratory, U.S. Government Printing Office, Washington, D.C., 1970.
- Jones, L.M. (1979), "An Introduction to Mathematical Methods of Physics," Benjamin/Cummings Publishing Co., 1979, pp. 247.
- Kanazawa, T., H. Oba and S. Machida (1961), "The Effect of Welding Residual Stress on Brittle Fracture Propagation," J. Soc., Nav. Archit., Japan, vol. 109, pp. 359-369.
- Kassir, M.K. and G.C. Sih (1975), "Three-dimensional Crack Problems, Mechanics of Fracture, 2", Noordhoff Int. Pub., Leyden, 1975, pp. 168.
- Kennard, F.L., B.C. Bradt and V.S. Stubican (1974), "Directional Solidification of the  $\text{ZrO}_2\text{-MgO}$  Eutectic", J. Amer. Ceram. Soc., vol. 57, No. 10, pp. 428-43.
- Kingery, W.D., H. K. Bowen and D.R. Uhlmann (1976), "Introduction to Ceramics," 2nd ed. J. Wiley and Sons, N.Y., 1976.
- Kriven, W.M. (1981), "Martensite Theory and Twinning in Composite Zirconia Ceramics," in Advances in Ceramics, vol. 3, The Amer. Ceram. Soc., Inc., 1981, pp.168-17.
- Kriven, W.M., W.L. Fraser and S.W. Kennedy (1981), "The Martensite Crystallography of Tetragonal Zirconia," in Advances in Ceramics vol. 3, pp. 82-97.



- Lang, S.M. (1964), "Axial Thermal Expansion of Tetragonal  $ZrO_2$  Between 1150°C and 1700°C, J. Amer. Ceram. Soc., vol. 47, No. 12, pp.641-644.
- Lang, S.M. and E.P. Knudson (1956), "Some Physical Properties of High Density Thorium Oxide," *ibid.*, vol. 39, No. 12, pp. 415-424.
- Lange, F.F., and D.J. Green(1981), "Effect of Inclusion Size on the Retention of T- $ZrO_2$ : Theory and Experiments," in Advances in Ceramics, vol. 3, pp. 217-225.
- Lange, F.F. (1980), personal communication.
- Lange, F.F. and G.R. Terwillinger (1973), "The Powder Vehicle Hot-Pressing Technique," Bull. Amer. Ceram. Soc., vo.1. 52, No. 7, pp. 563-565.
- Lange, F.F. (1970), "Interaction of Crack Front with Second Phase Dispersions," Phil. Mag., vol. 179, No. 22, pp. 983-992.
- Lawn, B.R., A.G. Evans and D.B. Marshall (1980), "Elastic/Plastic Indentation Damage in Ceramics: The Median/Radial Crack System," J. Amer. Ceram. Soc., vol. 63, No. 9-10, pp. 574-581.
- Lawn, B.R. and T.R. Wilshaw (1975), "Fracture of Brittle Solids," Cambridge Univ. Press, Cambridge, 1975.
- Leipold, M.H. (1976), "Hot Pressing," in Ceramic Fabrication Processes vol. 9, of Treatise on Materials Science and Technology, ed. by F.F. Wang, Academic press, N.Y. 1976, pp. 95-134.
- Marsden, J.E. (1973), "Basic Complex Analysis, W.H. Freeman and Co., 1973.
- Marshall, D.B. and B.R. Lawn (1977), "An Indentation Technique for Measuring Stresses in Tempered Glass Surfaces," J. Amer. Ceram. Soc., vol. 60, No.1-2, pp. 86-87.
- Matzke, HJ. (1980), "Hertzian Indentation of Thorium Dioxide,  $ThO_2$ ," J. Matls. Sc. Vol. 15, Ho. 3, pp. 739-746.
- Mazdiasni, K.S., C.T. Lynch and J.S. Smith (1967), "Cubic Phase Stabilization of Translucent Yttria-zirconia at Very Low Temperatures," J. Amer. Ceram. Soc., vol. 50, No.10, pp. 532-537.
- McClintock, F.A. and A.S. Argon (1966), "Mechanical Behavior of Materials," Addison-Wesley Publishing Co., Reading, Mass., 1966, pp. 80.
- McClintock, F.A., and F. Zaverl, Jr. (1979), "An Analysis of the Mechanics and Statistics of Brittle Crack Initiation," Inter. J. Fracture Mechanics, vol. 15, No.2, pp. 107-118.



- Miller, R.A., J.L. Smialek and R.G. Garlick (1981), "Phase Stability in Plasma-Sprayed Partially Stabilized Zirconia-Yttria," Advances in Ceramics, vol. 3, the Amer. Ceram. Soc., Inc. 1981, pp. 241-253.
- Mitsubashi, T., M. Ichihara and U. Tatsuke (1974), "Characterization and Stabilization of Metastable Tetragonal  $ZrO_2$ ," J. Amer. Ceram. Soc., vol. 57, No. 2, pp. 97-101.
- Mumpton, F.A. and R. Roy, (1980), "Low-Temperature Equilibria Among  $ZrO_2$ ,  $ThO_2$ , and  $UO_2$ ," Amer. Ceram. Soc., vol. 43, No. 5, pp. 237-240.
- Musikant, S. et al. (1978), "Advanced Optical Ceramics Phase '0'," Final Technical Report Contract No. N00014-77-C-0 649 (15 May, 1978).
- Musikant, S. et al. (1979), "Advanced Optical Ceramics Phase '1'," Annual report, contract No. N-0014-78-C-0466 (31 Aug. 1979).
- Musikant, S. et al. (1980), "Advanced Optical Ceramics Phase 'II'" Annual Report, contract No. N00014-78-C-0466 (31 August, 1980).
- Neilsen, T.H. and M.H. Leipold (1964), "Thermal Expansion of Yttria-Stabilized Zirconia," J. Amer. Ceram. Soc., vol. 47, No. 3, pp. 155.
- Ohnysty, B. and F.K. Rose (1964), "Thermal Expansion Measurements on Thoria and Hafnia to 4500°F," *ibid.*, vol. 47, No. 8, pp. 398-400.
- Olson, G.B. and C. Cohen (1976), "A General Mechanism of Martensitic Nucleation: Part I. General Concepts and The FCC-HCP Transformation; Part II. FCC-BCC and other Martensitic Transformations; Part III; Kinetics of Martensite Nucleation," Met. Trans. A. vol. 7A, No. 12, pp. 1897-1923.
- Pavalle, R., M. Rothstein and J. Fitch (1981), "Computer Algebra," Scientific American, vol. 245, No. 6, pp. 136-152.
- Panasyuk, V.V., A.E. Andrejkiv and M.M. Standnik (1981), "Three-Dimensional Static Crack Problems Solution (A review)," Engneer. Fract. Mechanics, vol. 14, No. 11, pp. 245-260.
- Porter, D.L., and A.H. Heuer (1977), "Mechanisms of Toughening Partially Stabilized Zirconia (PSZ)," J. Amer. Ceram. Soc., vol. 60, No. 3-4, pp. 183-184.
- Porter, D.L. and A.H. Heuer (1979a), "Microstructural Development in MgO-Partially Stabilized Zirconia (Mg-PSZ)," *ibid.*, vol. 62, No. 5-6, pp. 298-305.
- Porter, D.L., A.G. Evans and A.H. Heuer (1979b), "Transformation Toughening in Partially Stabilized  $ZrO_2$  (PSZ)," Acta Met. vol. 27, No. 12, pp. 1649-1654.
- Reith, P.H., J.S. Reed and A.W. Nauman (1976), "Fabrication and Flexural Ultrafine Grained Yttria-Stabilized Zirconia," Bul. Amer. Ceram. Soc. vol. 55, No. 8, pp. 717-721, 727.

- Rhodes, W.H. (1981), "Agglomerate and Particle Size Effects on Sintering Yttria-Stabilized Zirconia," J. Amer. Ceram. Soc., vol. 64, No. 1, pp. 19-22.
- Rhodes, W.H. and R.M. Haag (1970), "High Purity Fine Particulate Stabilized Zirconia (Zyttrite R)", Technical Report AFML-TR-70-209
- Rothman, E. (1981), personal communication.
- Ruhle, M. and R. Kraog (1981), "Experimental Determination of the Transformation Zone in  $Al_2O_3/ZrO_2$  Ceramics by HVEM, Am. Ceram. Soc. Bull., vol. 60, No. 3, 383.
- Scott, C.E. and J.S. Reed (1979), "Effect of Laundering and Milling on the Sintering Behavior of Stabilized  $ZrO_2$  Powders," Bull. Amer. Ceram. Soc., vol. 58, No. 6, pp. 587-590.
- Selsing, J. (1961), "Internal Stresses in Ceramics," J. Amer. Ceram. Soc., vol. 44, No. 8, pp. 419.
- Smith, D.K. and C.F. Cline (1962), "Verification of Existence of Cubic Zirconia at High Temperature," J. Amer. Ceram. Soc., vol. 45, No. 5, pp. 249-250.
- Sokolnikoff, I.S. (1956), "Mathematical Theory of Elasticity" 2nd ed. McGraw-Hill, 1956, pp. 337.
- Stubican, V.S. and J.R. Hellmann (1981), "Phase Equilibria in Some Zirconia Systems," in Advances in Ceramics, vol. 3, The Amer. Ceram. Soc. Inc., 1981, pp. 25-36.
- Virkar, A.V. (1981), personal communication.
- Wachtman, Jr. J.B., T.G. Scuderi and G.W. Cleek (1962), "Linear Thermal Expansion of Aluminum Oxide and Thorium Oxide from 100°K to 1100°K," J. Amer. Ceram. Soc., vol. 45, No. 7, pp. 319-323.
- Wolten, G.M. (1963), "Diffusionless Phase Transformations in Zirconia and Hafnia," *ibid.*, vol. 46, No. 9, pp. 418-422.
- Wang, F.F. (1976), editor of "Ceramic Fabrication Processes," Academic Press, N.Y., 1976, vol. 9, of Treatise on Materials Science and Technology.

### Biographical Note

Tom Ketcham was born October 1st, 1953 in Concord, California. He was raised primarily in Bountiful Utah and graduated from Viewmont High School in 1971. He received a B.S. in Materials Science from the University of Utah in 1975. He is a member of the American Ceramic Society. He has given several papers at the American Ceramic Society's annual conventions. He is presently the co-author of two publications:

"Hot Pressing of Lithia-Stabilized  $\beta$ "-Alumina"

A. V. Virkar, T. D. Ketcham and R. S. Gordon,  
Ceramurgia International, Vol. 5, No. 2, 1979, pp. 66-69.

"Toughened Optical Materials"

R. M. Cannon, Jr., T. D. Ketcham and T. W. Coyle  
to be published, SPIE Proceeding on Emerging Optical Materials.